UNIVERSITY OF SOUTHAMPTON

Environmental Controls on the State of HV Cables under the Seafloor

by

Timothy James Hughes

A thesis submitted in partial fulfillment for the degree of Doctor of Philosophy

in the

Faculty of Natural and Environmental Sciences

Ocean and Earth Science, National Oceanography Centre Southampton

2016-11-09

UNIVERSITY OF SOUTHAMPTON

ABSTRACT

FACULTY OF NATURAL AND ENVIRONMENTAL SCIENCES
OCEAN AND EARTH SCIENCE, NATIONAL OCEANOGRAPHY CENTRE SOUTHAMPTON

Doctor of Philosophy

Environmental Controls on the State of HV Cables under the Seafloor

by Timothy James Hughes

Submarine high voltage (HV) cables are becoming increasingly important to modern power transmission strategies. There has been a large amount of recent investment in projects such as offshore wind farms and international "megagrid" initiatives, of which submarine HV cables are essential components. A lot of research has been carried out into the thermal behaviour of HV cables buried on land. However, the performance of submarine HV cables has not been investigated extensively, despite several key differences between the two respective environments.

The amount of power that can be transmitted along an HV cable is often limited thermally by the maximum operational temperature of the cable components. It is therefore crucial to understand how heat is dissipated from HV cables as comprehensively as possible to ensure reliable, economical, and efficient deployment of these assets.

2D finite element method (FEM) simulations have been developed to examine the impact that certain environmental parameters have on the dissipation of heat generated within submarine HV cables into the surrounding burial sediment. Both conductive and convective heat transfer mechanisms are considered by solving coupled heat and fluid flow equations in a representative geometrical framework. The implications of some realistic inhomogeneous burial scenarios are considered, as is the impact of environmental conditions on cable temperature response times.

The FEM model suggests that the most influential environmental factor in determining the nature of the heat flow around submarine HV cables is a quantity called the intrinsic permeability. For sediments with a high permeability, convection can make a significant contribution to the overall transfer of heat from submarine HV cables into the surrounding environment, despite being neglected by traditional techniques for assessing heat flow around cables buried on land. Under these circumstances, cable temperatures are typically lower than for low permeability sediments.

Consideration of the additional cooling effect provided by convective heat transfer in these situations may result an increased cable current carrying capacity, or the potential to reduce the amount of conductor material required for manufacture.

Contents

List of Figures ix

List of Tables xi

Declaration xiii

Acknowledgements xv

List of Symbols xvi

Explanation of Notation xviii

1 Introduction 1

1.1 Submarine HV Cables in the Wider Context of Electricity Transmission Networks . . . 2

1.1.1 Common Applications of Submarine HV Cables . . . 2

1.1.2 The Increasing Prevalence of Submarine HV Cables . . . 3

1.1.3 Differences Between Marine and Terrestrial Environments . . . 5

1.2 Motivation for Research . . . 7

1.3 Contribution of this Thesis . . . 8

1.4 Thesis Structure . . . 9

2 HV Cables and Cable Ratings 11

2.1 Why is Heat Generated within HV Cables? . . . 12

2.1.1 Ohm's Law . . . 12

2.1.2 The Advantage of Transmission at High Voltages . . . 14

2.2 HV Cable Design . . . 15

2.2.1 Cable Conductor . . . 17

2.2.2 Insulation . . . 18

2.2.3 Metallic Sheath . . . 19

2.2.4 Armouring . . . 19

2.3 Installation Procedure . . . 20

2.4 Calculation of Cable Losses . . . 21

2.4.1 Skin Effect . . . 23

2.4.2 Proximity Effect . . . 23

2.4.3 Dielectric Losses . . . 24

2.5 Current Ratings . . . 26

2.5.1 The IEC 60287 Standard . . . 27
2.5.2 Numerical Methods . . . 30
2.6 The Finite Element Method . . . 31

3 Modelling Heat and Fluid Flow in Porous Media 35
3.1 Heat Transfer by Conduction and Convection . . . 36
3.2 Estimating the Thermal Conductivity of a Porous Medium . . . 40
3.2.1 Upper and Lower Bounds for the Effective Bulk Thermal Conductivity . . . 41
3.3 Darcy's Law . . . 43
3.4 Sensitivity Analysis . . . 47
3.4.1 Prioritising Parameters for Investigation . . . 49
3.5 Permeability . . . 50
3.5.1 Estimating Permeability . . . 51
3.5.1.1 Theoretical Justification for $\kappa \propto d^2$ . . . 52
3.5.1.2 Hazen's Method . . . 55
3.5.1.3 The Kozeny-Carman Equation . . . 56
3.5.1.4 Other Methods for Estimating κ . . . 58
3.5.1.5 Note for Results . . . 60
3.5.2 Permeability of Marine Sediments . . . 61
3.6 Modelling Heat Transfer from Submarine HV Cables . . . 64
3.6.1 Constructing the Model . . . 65
3.6.1.1 Equations . . . 65
3.6.1.2 Values of Auxiliary Parameters . . . 67
3.6.1.3 Generating the FEM Mesh . . . 68
3.6.1.4 Generation of Heat within the Cable . . . 69

4 Effect of Sediment Properties on the Thermal Performance of Submarine HV Cables 71
4.1 Introduction . . . 73
4.2 Model Overview . . . 75
4.2.1 Governing Equations . . . 75
4.2.2 Internal Heat Transfer within the Cable . . . 77
4.2.3 Geometry and Mesh . . . 78
4.2.4 Boundary Conditions . . . 79
4.2.5 Sensitivity Analysis . . . 80
4.3 Permeability and its Relation to Properties of the Sediment . . . 81
4.3.1 Permeabilities of Real Sediments . . . 81
4.3.2 The Kozeny-Carman Equation . . . 82
4.4 Results . . . 83
4.4.1 Qualitative Overview . . . 83
4.4.2 Varying Permeability and Thermal Conductivity . . . 86
4.4.3 Varying Burial Depth . . . 89
4.4.4 Comparison to the IEC 60287 Standard . . . 90
4.5 Impact on Cable Design . . . 91

4.6 Conclusion . . . 93

5 Submarine HV Cables in Different Environmental Scenarios 95
5.1 Introduction . . . 96
5.2 Homogeneous Sediment . . . 98
5.3 Trench Inhomogeneity . . . 99
5.3.1 Results . . . 102
5.4 Capping Silt Deposit Layer . . . 107
5.4.1 Results . . . 109
5.5 Refilled Scour Pit . . . 110
5.5.1 Results . . . 113
5.6 Discussion . . . 115
5.7 Conclusion . . . 118

6 Time Dependent FEM Simulations 119
6.1 Developing a 2D Time Dependent FEM Model . . . 120
6.2 Heat Up Time . . . 121
6.2.1 Results . . . 122
6.3 Cool Down Time . . . 124
6.3.1 Results . . . 124
6.4 Comparing Heat up and Cool Down Times . . . 125
6.5 Discussion . . . 127

7 Discussion and Conclusions 131
7.1 Contribution of Work . . . 133
7.2 Future Work . . . 137
7.2.1 3D Simulations and Experiments . . . 137
7.2.2 Online DTS Measurements . . . 138

A Current Density Perturbation due to the Skin Effect 141

B Verification of FEM Model Predictions 147
B.1 Experimental Setup . . . 148
B.2 Results . . . 151

C List of Attended Conferences and Published Papers 155
C.1 Journal Papers . . . 156
C.2 Conferences . . . 157

References 158

List of Figures

1.1 Interconnectors and wind farms around the UK 4

2.1 Example three phase SL-type HV cable 16
2.2 Example cable cross-section schematic 17
2.3 Example Milliken conductor schematic 18
2.4 The proximity effect 24
2.5 Loss tangent in the complex plane 26
2.6 An example FEM mesh for a cable schematic 32

3.1 Cartesian volume element with conductive and convective fluxes . . 37
3.2 Heuristic representation of different models for estimating λ_b 41
3.3 Physical characteristics of sediments 52
3.4 Permeabilities predicted by the Kozeny-Carman equation for different porosities and grain sizes 57
3.5 Comparison of permeability estimation methods 60

4.1 Cable routes and sediment grain sizes around the UK 74
4.2 Schematic of the simulation geometry 77
4.3 Permeabilities predicted by the Kozeny-Carman equation for different porosities and grain sizes 83
4.4 Example temperature profiles for cables buried in porous sediments 85
4.5 Dependence of the cable conductor temperature on permeability . . 87
4.6 Vertical convective flux above the cable 88
4.7 Dependence of the cable conductor temperature on thermal conductivity 89
4.8 Dependence of the cable conductor temperature on burial depth . . 90
4.9 Dependence of the cable conductor temperature on cable current load 92

5.1 Environmental scenarios to be considered 97
5.2 Temperature distributions for cables in homogeneous sediments . . 100
5.3 Temperature distributions for cables with a trench inhomogeneity . 100
5.4 Temperature distributions for cables buried under a low permeability layer deposit 101
5.5 Temperature distributions for cables buried under a refilled scour pit 101
5.6 Effect of trenching for different native sediment permeabilities . . . 104
5.7 Effect of trench width on cable temperature 105

5.8 Hjulström curve illustrating the flow velocities for which sediment grains will be eroded, transported, and deposited. 107
5.9 Effect of low permeability layer deposits for different native sediment permeabilities 109
5.10 Effect of varying porosity and grain size on cable temperature . . . 112
5.11 Effect of refilled scour pit material for different native sediment peremabilities 114
5.12 Effect of cable burial depth on temperatures for different native sediment permeabilities 115
5.13 Effect of inhomogeneities on temperatures in the top 20 cm of sediment below the seabed surface 117

6.1 Time dependent FEM model results showing cable heat up times . 123
6.2 Time dependent FEM model results showing cable cool down times 125
6.3 Departure from initial temperature with time for heat up and cool down phases 126
6.4 Effect of sediment thermal conductivity on cable heat up times . . . 129

7.1 Temperature of two cables buried in sediments different permeabilities 134

A.1 The skin effect 145

B.1 The empty experimental tank 149
B.2 Positions of the heat source and thermocouples 150
B.3 Temperature plots of the experimental tank 152

List of Tables

3.1 Example estimated bulk thermal conductivities 43
3.2 Natural variation in relevant environmental parameters 48
3.3 List of permeability estimation methods 59
3.4 List of estimated permeabilities from grain size 61
3.5 Measured permeabilities of marine sediments 63
3.6 Comparing FEM models that use different methods for estimating λ_b 66
3.7 List of parameters used in the FEM model 68
3.8 Comparison of heat transfer rates in different materials 70

4.1 Geometry of the cable used in the FEM model 78
4.2 Range of possible environmental parameter values 80
4.3 Comparison of FEM model results with IEC 60287 91

6.1 Time taken to heat up a cable to equilibrium 122

Declaration

I hereby declare that this thesis has been composed solely by myself, and that it has not been submitted, in whole or in part, in any previous application for a degree. The work presented is entirely my own, except where indicated explicitly by reference or acknowledgement. Furthermore, I confirm that I have exercised reasonable care to ensure that the work is original and does not, to the best of my knowledge, breach any law of copyright. Part of this thesis has previously been published as:

Hughes, T.J., Henstock, T.J., Pilgrim, J.A., Dix, J.K., Gernon, T.M., Thompson, C.E.L., "Effect of Sediment Properties on the Thermal Performance of Submarine HV Cables", *IEEE Transactions on Power Delivery* **30**(6) p.2443-2450 (2015)

Timothy James Hughes
2016-11-27

Acknowledgements

I would like to express my sincere thanks to all my supervisors: Tim Henstock, Justin Dix, James Pilgrim, Tom Gernon, and Charlie Thompson for all the tremendous help and support that they have provided me with during the course of my PhD, and during the writing of this thesis. The knowledge and experience you have shared with me in such a broad range of subjects has been invaluable. Thank you for always finding time to talk about the difficulties and opportunities that I have faced, and for your enthusiasm for the project.

A special thanks goes to my primary supervisor, Tim Henstock. Throughout all the challenges I have encountered over the last four years, you have been a dependable and friendly source of perceptive and astute advice.

I am extremely grateful for the financial support I have received from the Research Councils UK through the HubNet Consortium (grant number: EP/I013636/1), which made this research possible.

I am also indebted to John Emeana for his related experimental work, for being someone to share ideas and chat with, and for the insights and context gained by considering both of our parallel investigations together.

Thanks also goes to National Grid for their support of the work, and the encouragement that they have provided more broadly to the group as a whole.

Finally, thanks for all the personal support I have received from my parents, Bev and Chris, and my girlfriend Holly. Thanks to my housemates for being such great company over the past few years, and thanks to my office mates for so many interesting discussions and sharing my enthusiasm for tea.

List of Symbols

A	$[\mathrm{m}^2]$	Cross-sectional area
b	[m]	Burial depth
$\mathbf{B}$	[T]	Magnetic field
β	$[\mathrm{K}^{-1}]$	Volumetric coefficient of thermal expansion
c_p	$[\mathrm{Jkg}^{-1}\mathrm{K}^{-1}]$	Heat capacity at constant pressure
C	$[\mathrm{Fm}^{-1}]$	Capacitance per unit length
d	[m]	Grain size
δ^{ij}	–	Kronecker delta
$-e$	[C]	Electric charge of a electron
ε	$[\mathrm{C}^2\mathrm{s}^2\mathrm{kg}^{-1}\mathrm{m}^{-3}]$	Electric permittivity
ε_0	$8.85 \cdot 10^{-12}\ \mathrm{C}^2\mathrm{s}^2\mathrm{kg}^{-1}\mathrm{m}^{-3}$	Electric permittivity of free space
$\mathbf{E}$	$[\mathrm{JC}^{-1}\mathrm{m}^{-1}]$	Electric Field
f	[Hz]	Frequency
$\mathbf{F}$	[N]	Force
$\boldsymbol{\phi}$	$[\mathrm{ms}^{-1}]$	Fluid discharge per unit area
Φ	$[\mathrm{m}^3\mathrm{s}^{-1}]$	Fluid flux
Φ_E	$[\mathrm{JC}^{-1}]$	Electric potential
g	$[\mathrm{ms}^{-2}]$	Gravitational (scalar) acceleration
h	$[\mathrm{Wkm}^{-2}]$	Convective heat transfer coefficient
h_h	[m]	Hydraulic head
I	[A]	Current
$\mathbf{J}$	$[\mathrm{Am}^{-2}]$	Current density
κ	$[\mathrm{m}^2]$	Permeability

L	[m]	Length
λ	[$\mathrm{Wm^{-1}K^{-1}}$]	Thermal conductivity
λ_1	-	Ratio of sheath to total conductor losses
λ_2	-	Ratio of armour to total conductor losses
m	[kg]	Mass
μ	[$\mathrm{kgm^{-1}s^{-1}}$]	Dynamic viscosity
μ_B	[$\mathrm{kgmC^{-2}}$]	Magnetic permeability
n	-	Porosity
$\mathcal{N}_u$	–	Nusselt number
p	[$\mathrm{kgm^{-1}s^{-2}}$]	Pressure
P_E	[W]	Power
q_e	[C]	Electric charge
$\mathbf{q}$	[$\mathrm{Wm^{-2}}$]	Heat flux
Q	[$\mathrm{Wm^{-3}}$]	Heat source per unit volume
r	[m]	Radius
R	[Ω]	Electrical Resistance
$\mathcal{R}_a$	-	Rayleigh number
$\mathcal{R}_e$	-	Reynolds number
ρ	[$\mathrm{kgm^{-3}}$]	Density
ρ_c	[$\mathrm{Cm^{-3}}$]	Charge density
ρ_e	[Ωm]	Electrical resistivity
σ	[$\mathrm{\Omega^{-1}m^{-1}}$]	Electrical conductivity
t	[s]	Time
$\tan(\delta)$	-	Loss tangent
T	[K]	Temperature
T_0	[K]	Ambient temperature of overlying seawater
τ	$\mathrm{mKW^{-1}}$	Thermal resistance per unit length
$\mathbf{u}$	[$\mathrm{ms^{-1}}$]	Velocity
U	–	Coefficient of grain uniformity
V	[V]	Potential difference (voltage)

V_f	[m^3]	Fluid volume
W_d	[Wm^{-1}]	Dielectric loss per unit length
ω	[Hz]	Angular frequency
χ	–	Electric susceptibility
y_p	–	Proximity effect coefficient
y_s	–	Skin effect coefficient

Explanation of Notation

Scalars, Vectors, Matrices, and Tensors

- Scalar quantities are denoted by normal script; roman alphabet variable labels are italicised, *e.g.*:

$$a \quad \text{or} \quad \alpha$$

- The imaginary unit will be denoted by i.

- Vector, matrix, and tensor quantities are denoted by bold symbols, *e.g.*:

$$\mathbf{a} \quad \text{or} \quad \boldsymbol{\alpha}$$

  The scalar components of vectors and matrices are labelled with subscripts.

- The common labels (x, y, z) and (r, θ, z) are used to denote points in Cartesian and cylindrical coordinates systems respectively.

- Unit vectors are written as bold symbols with a hat, *e.g.*:

$$\hat{\mathbf{a}} \quad \text{or} \quad \hat{\boldsymbol{\alpha}}$$

- The scalar product between two vectors, $\mathbf{a}, \mathbf{b}$ in three dimensional Euclidean space ($\mathbb{E}^3$) is denoted:

$$\mathbf{a} \cdot \mathbf{b} = \sum_{i=1}^{3} a_i b_i$$

  This "dot" notation is also occasionally used to express multiplication of scalar quantities.

- The vector product (also called the cross product) between two vectors, $\mathbf{a}$ and $\mathbf{b}$, in three dimensional Euclidean space ($\mathbb{E}^3$) is denoted:

$$\begin{aligned}\mathbf{a} \times \mathbf{b} &= (a_1\hat{\mathbf{x}} + a_2\hat{\mathbf{y}} + a_3\hat{\mathbf{z}}) \times (b_1\hat{\mathbf{x}} + b_2\hat{\mathbf{y}} + b_3\hat{\mathbf{z}}) \\ &= (a_2b_3 - a_3b_2)\hat{\mathbf{x}} + (a_3b_1 - a_1b_3)\hat{\mathbf{y}} + (a_1b_2 - a_2b_1)\hat{\mathbf{z}}\end{aligned}$$

Calculus

- When used in standalone equations, the differential or partial differential of a quantity, b with respect to another quantity, a will be expressed respectively as:

$$\frac{db}{da} \quad \text{and} \quad \frac{\partial b}{\partial a}$$

  However, when one of these operators appears in the text, the following convenient shorthand may be used:

$$\partial_a b = \frac{\partial b}{\partial a}$$

- The operator ∇ is also used extensively to denote the gradient of a scalar:

$$\nabla a$$

  the divergence of a vector:

$$\nabla \cdot \mathbf{a}$$

  or, the curl of a vector:

$$\nabla \times \mathbf{a}$$

  Unless otherwise stated, ∇ refers to the Cartesian operator defined by:

$$\nabla = \hat{\mathbf{x}}\frac{\partial}{\partial x} + \hat{\mathbf{y}}\frac{\partial}{\partial y} + \hat{\mathbf{z}}\frac{\partial}{\partial z}$$

CHAPTER 1

Introduction

1.1 Submarine HV Cables in the Wider Context of Electricity Transmission Networks

One of the defining aspects of life in the modern world is the convenience of access to a dependable and plentiful supply of electricity. This essential utility is delivered to consumers from power generating stations via an extensive and intricate network of cables. It is often advantageous for these networks to include links that traverse large bodies of water.

1.1.1 Common Applications of Submarine HV Cables

The first power cable to be installed underwater was completed in 1811, and ran across the river Isar in Germany.[1,2] Like most early underwater cables, it had a relatively basic design intended to accommodate low voltages. Since then, a lot of progress has been made in both the design of the cables themselves, as well as the construction procedures and constituent materials used in the manufacturing process.

Today, modern submarine HV cables have numerous applications. Perhaps the most intuitively recognizable application of these types of cable is to supply offshore installations and island communities with electricity. For example, the Isle of Man to England interconnector provides an electrical connection between the eponymous island and the UK mainland with a maximum capacity of 50 MW.[3] The cable allows the islanders to both import energy from, and export what energy they generate domestically to the network on the UK mainland.

The trading or sharing of electricity between different nations (or regions of countries) can also provide motivation for the construction of these submarine cable links in and of itself. Each grid network requires a set amount so called "spinning reserve": power generation capacity that can be switched on at short notice to meet spikes in demand for electricity. This reserve capacity is traditionally met by idling generators, however it is more efficient to augment the spinning reserve with interconnection.[4] The demand peaks are likely to occur at different times in different countries;[4] sharing electricity between networks via HV interconnector cables can help to reduce the strain placed on the domestic power stations of the consumer region during these times. It also simultaneously reduces the amount

of surplus energy in the supplying region (energy that would otherwise require storage, which may be complicated and/or inefficient). Furthermore, access to a wider power generation market through interconnection may lead to a reduction in the unit price for electricity through increased competition.[5,6]

Submarine HV cables are also necessary for transmitting electricity generated offshore from renewable sources (*e.g.* wind, wave, *etc.*) back to the grid network on land ready for distribution to consumers.

1.1.2 The Increasing Prevalence of Submarine HV Cables

Submarine HV cables play a key role in contemporary power transmission strategies. The cross-channel link between the UK and France alone has a maximum transmission capacity of 2 GW[7] (to put this figure in context, the aggregate power consumption for the UK during the year of 2014 was 303 TWh[8] - equivalent to a year averaged constant power load of just under 34.6 GW). The net amount of power imported by the UK has seen a sharp increase in recent years, from 11.9 TWh in 2012[9] to 20.9 TWh in 2015.[8] The total supply of electricity available to the UK through existing interconnector links is 4 GW,[6,8] with more projects planned for the near future.[10,11] Illustrated in Figure 1.1 are the interconnector cables and offshore wind farms in and around the UK that are currently operational, as well as those that have been (at the time of writing) approved for construction, or are currently under construction. In addition to those indicated, there are also a number of projects that are either in the early stages of discussion or planning. Many of these proposals are for cables connecting the UK to countries that it is currently not directly linked with, including: Belgium, Denmark, Norway, and Iceland.[11]

The desire to increase the amount of HV interconnection is by no means limited to the UK. There are numerous plans to develop interconnectors between other European nations. Extensive, intertwined, large scale transmission networks like the one currently being slowly cultivated in northern Europe are commonly and colloquially termed "supergrids". The European supergrid connections concentrated around the North Sea are part of a wider strategy to minimise electricity consumption in Europe. This is achieved by interconnecting major demand and generation centres, and integrating renewable generation and storage into the large scale electricity network.[13] The motivation behind creating such a complicated and

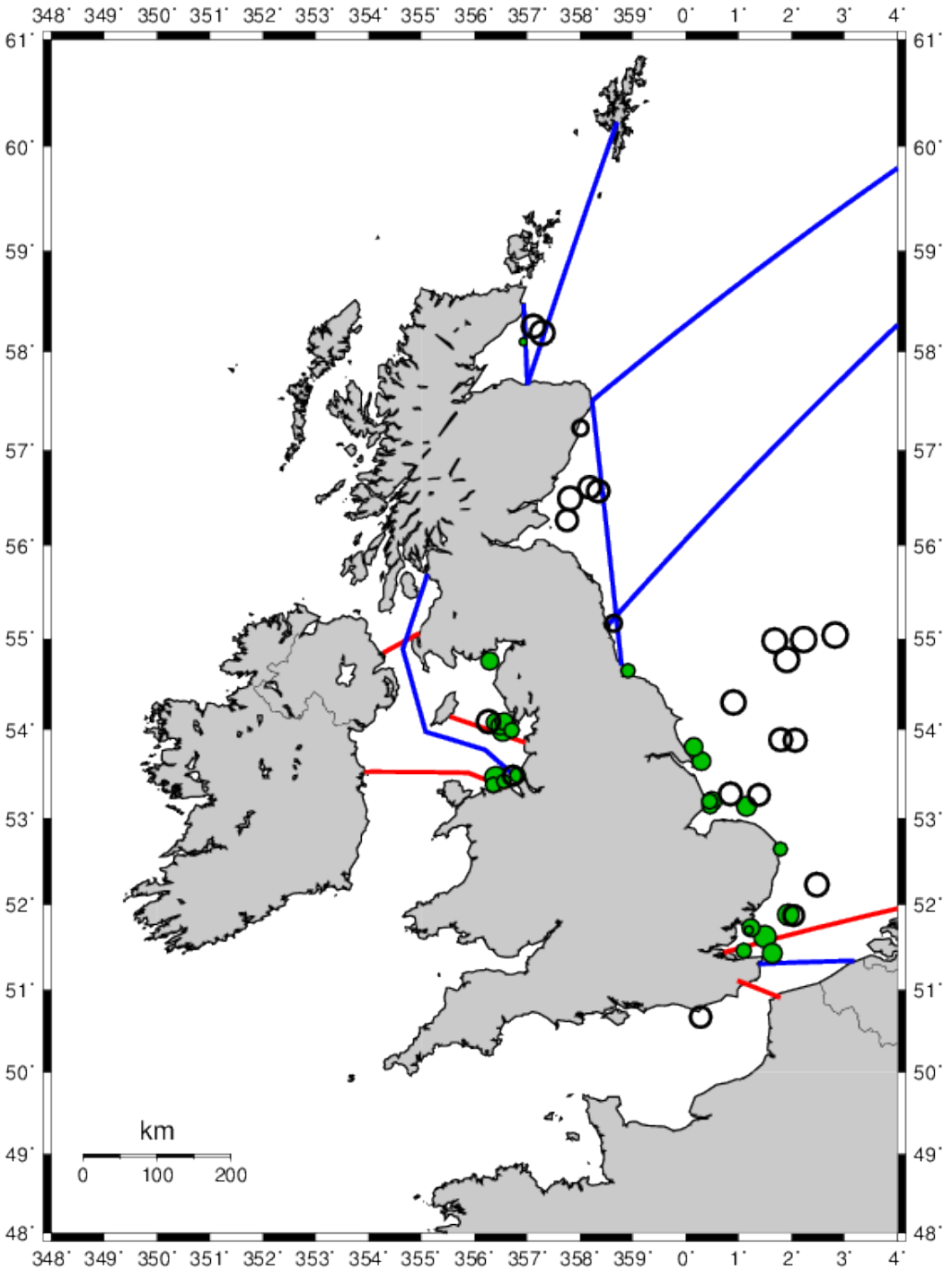

Fig. 1.1: Map illustrating the existing (red lines) and approved/under construction (blue lines) interconnector cables[11] and operational (green circles) and approved/under construction (black circles) offshore wind farms[9,12] in and around the UK.

costly network comes in part from the desire to meet political commitments in reducing carbon emissions in an attempt to mitigate climate change. However, it is not just offshore wind farm export cables that are relevant for reducing carbon emissions. Large amounts of interconnection give inland countries access to the offshore wind generation potential available in the North Sea. Interconnection also allows generated electricity to be stored in pump storage hydroelectric plants, which are located predominantly in Norway[14] (which would perhaps be geographically inconvenient without the capability to construct submarine HV cables). Interconnector links are therefore very relevant during strategic discussions endeavouring to reduce the total power generation required (and hence fossil fuel usage) on very large scales.[15]

Being an island nation, the UK is ideally situated to take advantage of offshore power generation. Presently, the most prevalent source of power generated offshore for UK markets is derived from wind turbines.[8] At the time of writing, the aggregate power generation capacity of offshore wind projects in the UK stood at just over 5.1 GW.[8] There continues to be a large amount of investment into schemes of this kind, with some draft strategic plans indicating that as much as 18 GW of offshore generation potential could be available to the UK market by the year 2020.[8] By comparison, wave and tidal technologies are currently relatively immature and costly to implement. It is worth noting, however, that the potential future contribution of wave and tidal energy resources is huge. It is estimated that in the waters around the UK, wave and tidal generation could contribute a total of up to 70 TWh[16] of electricity every year ($\sim$ 20% of current annual electricity generation[8]), and is the largest resource of marine energy of this kind in Europe.[17]

Submarine HV cables are becoming much more prevalent in the world today, with large levels of investment into both interconnector and offshore power generation schemes in the UK, in Europe, and around the world.

1.1.3 Differences Between Marine and Terrestrial Environments

The most intuitively heuristic difference between the submarine and terrestrial environments is that the substance that overlies the burial medium will be different. For the well studied case of HV cables buried on land, the overlying material is air. For submarine HV cables, the material is seawater. This overlying seawater provides a convenient reservoir of fluid that may (under certain circumstances) help

to mitigate any temperature driven moisture migration (because the opposing hydraulic gradient created in the submarine scenario is greater than in the terrestrial one). This vast reservoir will likely maintain the saturation of the burial sediment at very high levels (at least in the absence of any aforementioned temperature induced moisture migration).

Heat transfer within a porous medium is sensitive to the topology and relative proportions of all of the constituent material phases. For cables buried on land in porous media with relatively low water saturations, the transfer of heat by both liquid water and water vapour must be considered.[18] The nature of the heat transfer will be dependent on the degree of continuity and connectedness of the liquid and vapour phases within the porous matrix. Numerous investigations into the dissipation of heat from HV cables buried on land consider the aforementioned phenomenon.[19–22] For porous media that are highly saturated with a liquid phase, the contribution to the overall heat transfer from the vapour phase is negligible;[18] the dissipation of heat generated in cables buried under the seafloor must be modelled in a different manner.

The convective heat transfer coefficient, h, for water is much larger than it is for air;[23] heat can be transferred much more efficiently from the burial medium to overlying water than to overlying air. This means that seawater acts as a more effective heat sink for submarine burial scenarios than wind does for terrestrial burials. However, water is a good absorber of radiation in the wavelength range (infrared) expected to be emitted at typical cable surface temperatures*.[24,25] For submarine HV cables, radiative heat transfer is therefore unlikely to transfer a significant amount of heat either within the burial medium pore space (which is likely to be saturated), or from the surface of the medium into the overlying material. This is not the case for cables buried on land.[26–28]

The sediment exposed at the surface of the seabed can exhibit considerable spatial heterogeneity in type, and physical properties. This is illustrated at very large scales by the distribution of sediment types around the UK displayed in Figure 4.1. However, it is not uncommon to see substantial variation in the type of sediment on the seabed over much smaller length scales than this, right down to hundreds of metres or even metres.[29,30] Submarine HV cables are therefore likely to be exposed to wide range of different sediment types and burial conditions along their route.

*For temperatures in the range 10 - 90 °C (see Section 2.5), the peak wavelength of a blackbody spectrum will be between 7 and 10 μm.

The seabed environment can be a lot more dynamic in nature than on land; sediment can be excavated and deposited on very short timescales (something that does not often occur on land except in catastrophic circumstances). Features called bedforms can migrate across the seabed at a rate of 10s of metres per year, and cause variation in the local bed level heights of several metres over the same time period.[31] This variation in burial depth may also have implications for the thermal situation of submarine HV cables, as it amounts to an alteration of the distance between the cable, and the heat sink of the overlying seawater.

1.2 Motivation for Research

On land, cables are often buried under the ground surface. There are a number of reasons why underground cables may be preferred to overhead lines. Burial provides mechanical protection and obfuscates the cable location, which may help to avoid arousing the curiosity of any local inhabitants or wildlife that may (intentionally or otherwise) damage the cable. Overhead lines alter the landscape, and are often considered to be detrimental to the aesthetic of the local area (particularly rural areas). This can lead to delays in obtaining legal approval for the cable.[32]

When a current is passed along an HV cable, some of the transferred energy is inevitably lost as heat. This causes an interesting problem for the design of HV cables, as the degradation of the cable insulation material is a function of temperature,[4,22,33] and degrades at a much faster rate when exposed to high temperatures. One commonly quoted rule of thumb states that an increase in the cable operating temperature of 8 - 10 °C will result in a 50% reduction in its lifetime.[4] For this reason, a maximum normal operating temperature is imposed (commonly set at 90 °C for XLPE-insulated cables[4,22,33,34] - see Section 2.2.2).

A lot of research has been carried out with the aim of better understanding and predicting how heat generated within a buried cable is dissipated into the surrounding medium.[19–22,27,35–41] However, the vast majority of these investigations are based on scenarios that are representative of cables that are buried in a terrestrial environment. Outlined above in Section 1.1.3 are a variety of differences between the terrestrial and submarine environments. Determining how these differences affect the dissipation of heat from HV cables, and developing procedures for predicting their thermal behaviour in a submarine burial environment will help to inform the design of future assets. For example, the amount of heat generated

within the cable is inversely proportional to the cross-sectional area of its conductor(s). If this heat can be dissipated more effectively in a particular marine sediment than previously acknowledged, the conductor cross-section required to transmit a given amount of power along an HV cable can be reduced (saving costs on the raw materials for the conductor during manufacturing). Conversely, if the heat dissipation is less efficient than current understanding suggests, temperatures within the cable would be higher than expected. In this case, either the transmission capacity of the cable would have to be reduced below its intended level, or the safe operational temperature of the cable will be exceeded (compromising its expected lifetime and increasing thermal losses).

Gaining an insight into the nature of the thermal environment that these cables might be exposed to (and how that environment might differ from a more familiar setting) will be very useful for maximising the performance, efficiency, and lifetime of these assets. This knowledge and understanding is likely to become more valuable as investment into submarine HV cables continues to increase (see Section 1.1.2).

1.3 Contribution of this Thesis

Presented herein is an examination of how heat generated within HV cables buried in the submarine environment is dissipated into the surrounding seabed. Among the key questions and considerations that have been investigated are:

- To what extent do the differences between the submarine and terrestrial environments discussed in Section 1.1.3 alter how heat is dissipated from buried HV cables?
- What geological and thermodynamic parameters are likely to have the greatest influence on the effectiveness of the heat dissipation from submarine HV cables?
- Will other mechanisms for transferring heat (*i.e.* convection and radiation) play more of a role in its dissipation from submarine HV cables than they do for terrestrially buried cables?
- What are the implications of any differences in thermal behaviour for the design and operation of submarine HV cables?

The first step in attempting to address these questions was to identify the geological and thermodynamic parameters that are most likely to have the greatest impact on the thermal behaviour of submarine HV cables. A finite element method (FEM) model has been developed to explore how variations in these parameters affect the thermophysical mechanisms involved in determining the nature of the heat flow through the burial medium surrounding the cable (and the circumstances under which the thermal behaviour differs most from that of terrestrial cables). This is accomplished by considering both the flow of heat and the flow of fluid through the sediment simultaneously. There is also a brief discussion on the possible implications of the results of this modelling (from both an electrical engineering, and geological perspective). The veracity of the predictions made by the FEM model are assessed by making a comparison to a laboratory experiment designed to provide a physical analogue for the simulations (see Appendix B).

The FEM model initially designed to investigate this problem has also been modified to determine how much influence certain sources of inhomogeneities in the burial environment can have on the temperature of the cable conductors. For example, to what extent will the mechanisms of heat transfer be affected by the deposition of additional material on the seabed surface above the cable.

While the most natural application of the work detailed herein is to the electrical engineering and HV cable community (in exploring the semantics of how these assets behave thermally in a submarine environment), a lot of the content may also be relevant for the geological community in terms of analysing how heat is transferred through marine sediments of different types, and under different environmental circumstances.

1.4 Thesis Structure

Chapter 2 briefly explains the physics of why heat is generated within HV cables when a current is passed along them. A description of the structure of submarine HV cables, and existing methods for determining current ratings (originally developed for application to terrestrially buried HV cables) is also given here.

Chapter 3 gives an contextual overview of the theory of heat transfer; of particular interest is the application to heat transfer through porous media. Specific attention will be given to how the theory can be applied to scenarios that resemble the kinds of environment that a submarine HV cable might be expected to encounter

along its route (*i.e.* a porous medium composed of a solid phase that is simply connected, and a permeating liquid phase that may be slightly more intermittent). A discussion of the theory behind fluid flow through porous media is also given here, as convection is integral to the treatment of heat transfer described and applied herein. An heuristic analysis of the likely ranges for each relevant parameter is given, based on observations of naturally occurring sediments, or experimental investigations into the temperature dependence of certain quantities. From the initial stages of the investigation, it became clear that one quantity that may have substantial implications for the dissipation of heat from submarine HV cables is the sediment permeability, κ. Chapter 3 introduces this parameter, attempts to contextualise it in terms of other characteristics of the sediment, and illustrates a number of approaches that can be taken to try and evaluate it (which will be invaluable during interpretation of the FEM model results).

The contents of Chapter 4 is comprised of a paper published in *IEEE Transactions on Power Delivery*. Detailed within is a brief outline of an FEM model developed to simulate the dissipation of heat from an example submarine HV cable buried under the seafloor. Simple results from these simulations are also presented, along with an examination of the relative influence certain environmental parameters have on determining the nature of the heat dissipation away from the cable and into the surrounding marine sediment.

Chapter 5 expands on the FEM model constructed in Chapter 3, and discussed in Chapter 4. Several potential sources of inhomogeneities in the burial sediment are selected for further investigation on a heuristic basis, by considering cable installation procedures, and the physical processes that occur in a seabed environment. These classes of inhomogeneity are individually incorporated into a series of augmented FEM models. Based on the simulation results, an assessment can be made in each case as to whether the class of inhomogeneity in question is capable of significantly altering the thermal behaviour of submarine HV cables.

Chapter 6 introduces time dependence to the FEM model. The time response for temperatures in and around the cable are explored, and the effect of varying certain relevant environmental parameters is assessed.

CHAPTER 2

HV Cables and Cable Ratings

2.1 Why is Heat Generated within HV Cables?

The generation of heat within a cable or wire carrying a current is a familiar phenomenon. Some household appliances get hot after an extended period of use, while others make a direct use of this heating effect (*e.g.* electric kettles, toasters). The reason this happens is that one inevitable consequence of the movement of electrons within a conductor is that occasionally there will be a collision between an electron, and one of the constituent ions of the conductor. During one of these collisions, the electron loses a portion of its kinetic energy to the conductor ion. The resulting increase in the kinetic energy of the conductor ion is manifest as an increase in the temperature of the cable conductor;[42] this effect is commonly called Joule, or Ohmic heating.

2.1.1 Ohm's Law

In the context of electrical cables the scalar current, I [A], is defined as the movement of electrons (each with an electric charge of $-e^*$) along the cable conductor.[43] In terms of the total charge, q_e [C]:

$$I = \frac{dq_e}{dt} \tag{2.1}$$

The current density, $\mathbf{J}$ [Am^{-2}] is simply defined as the current per unit area perpendicular to the flow:[44]

$$\mathbf{J} = \frac{I}{A} \tag{2.2}$$

where the parameter A [m^2] is the cross-sectional area of the cable. Ohm's law states that the current density, $\mathbf{J}$ is directly proportional to the applied electric field, $\mathbf{E}$ [$\mathrm{JC}^{-1}\mathrm{m}^{-1}$][42,44,45] (the constant of proportionality, σ is called the conductivity of the material):

$$\mathbf{J} = \sigma\mathbf{E} \tag{2.3}$$

Although the original discovery of Ohm's law was through empirical observation, a theoretical basis for it can nevertheless be insinuated by considering the Drude model of electrical conductivity.[44] In this model, electrons within a conductor are treated as an ideal gas composed of particles being accelerated antiparallel to an applied electric field. Collisions between electrons and ions of the conductor lattice randomises the momentum of the electrons. The force applied on the electrons

N.B.: By convention, current flows in the opposite direction to the movement of electrons.

from the electric field (called the Lorentz force, $\mathbf{F} = -e\mathbf{E}$[42]) provides a small (*cf.* the thermal velocities of the electrons) statistical drift velocity, which is the classical current.[42,44] *N.B.* The Drude model is not considered to be an accurate representation of electron transport (it is a classical picture that does not take account of quantum effects), but it does provide a useful qualitative supporting justification for Ohm's law.

The electric field is essentially a measure of the amount of electromagnetic force that is applied to a particle of unit charge at a given point in the field. The work done by this field in bringing a test charge, q_e from point a to point b is given by the line integral:[44]

$$V = \Phi_{\mathrm{E}}(a) - \Phi_{\mathrm{E}}(b) = -\int_b^a \mathbf{E} \cdot d\mathbf{l} \tag{2.4}$$

where V [JC^{-1}]* is the difference in electric potential (Φ_{E}), or voltage, between the two points, a and b. If a and b are the endpoints of a cable of length L [m] and the electric field is parallel to the length of the cable, then equation (2.4) implies that the potential difference is related to the electric field via:

$$V = |\mathbf{E}| \cdot L \tag{2.5}$$

Using the definition of the current density given in equation (2.2) combined with equation (2.5), the form of Ohm's law quoted in equation (2.3) can now be expressed in the more familiar way:

$$\begin{aligned} \mathbf{J} &= \sigma\mathbf{E} \\ \frac{I}{A} &= \sigma\frac{V}{L} \\ V &= \frac{\rho_e L}{A} I \\ V &= IR \end{aligned} \tag{2.6}$$

Here, the resistance of a cable, R [Ω] is a function of the geometry of the cable conductor, as well as the material from which it is constructed according to the formula:[46]

$$R = \frac{\rho_e L}{A} \tag{2.7}$$

*or [V].

The electrical resistivity, ρ_e [Ωm] is defined as the inverse of the conductivity, σ. It is an intrinsic property of the conductor material that quantifies the degree to which it opposes the flow of electrons through it. To build an efficient cable, it is therefore preferable to manufacture a conductor with a very large cross-section from a material with a low resistivity. This is not practical or cost effective under all circumstances (in terms of the amount of required raw materials); a balance must be struck between the upfront cost of manufacturing the cable, and the ongoing costs incurred from thermal losses. In recognition of this, electricity networks are composed of a variety of different types of cables that are suited for transmitting different amounts of power at differing voltages over various distances. Larger HV cables are used for the bulk transmission of electricity over long distances, medium voltage (MV) cables are used for transmission of moderate amounts of power over (usually) smaller distances, and small, low voltage cables (LV) are used for the distribution of electrical energy from local substations to consumers.

2.1.2 The Advantage of Transmission at High Voltages

The electric potential, Φ_{E} is essentially a measure of energy per unit charge;[42] this can be inferred by dimensional analysis of equation (2.4). Hence, the total amount of power that is lost as heat along the entire length of a cable through the aforementioned Joule heating effect can be expressed in terms of the difference in potential between the two endpoints of the cable, a and b. If electrical energy is being transmitted from point a to point b, the power loss can be expressed as*:

$$\begin{aligned} P_{\mathrm{E}_{\mathrm{loss}}} &= \Big(\Phi_{\mathrm{E}}(a) - \Phi_{\mathrm{E}}(b)\Big) \cdot \frac{dq_e}{dt} \\ &= VI \end{aligned} \tag{2.8}$$

Hence, by combining equations (2.6) and (2.8), the total amount of power lost as heat when transmitting a current along the cable can be expressed as:

$$P_{\mathrm{E}_{\mathrm{loss}}} = I^2 R \tag{2.9}$$

Note that this quantity is not explicitly dependent on the absolute magnitude of the electric potential, Φ_{E} (it depends only on the potential difference between cable endpoints). However, the total amount of usable power transmitted along

**N.B.*: Here, V is the potential difference between the points a and b, not the voltage to earth.

the cable is:

$$P_{\mathrm{E}} = \Phi_{\mathrm{E}}(b)I \tag{2.10}$$

From equations (2.9) and (2.10), it follows that it is much more efficient to transmit power over large distances at the lowest currents and highest voltages possible (provided the product of the voltage and the current remains identical).

2.2 HV Cable Design

High voltage power cable design structure is very much dependent on the desired transmitted power, the type of current to be transmitted (AC or DC*), and the technical considerations of individual cable routes. For example, while high voltage direct current (HVDC) cables have a single core, high voltage alternating current (HVAC) cables commonly include multiple cores (often three, in a trefoil arrangement) as seen in Figure 2.1. Each core transmits current at a different phase to mitigate the inherent losses associated with alternating current (see sections 2.2.1 and 2.4).

The cable design used during the development of the FEM model was based on that of a generic three phase SL-type ("separate lead", as each core has its own lead sheath) 132 kV cable (this is one of the voltages used for the transmission of electricity within the UK grid network[22,47]) similar to those available commercially, with the component dimensions altered slightly† from the original. A schematic of this cable is displayed in Figure 2.2. The exact dimensions and thermal properties used for each component in the model are displayed in Table 4.1.

The comparatively extreme conditions (thermal, electromagnetic, and mechanical) that these types of cable will be exposed to, and must endure necessitates the inclusion of several additional components to ensure their reliable and safe operation. The following subsections give an overview of some of the components more relevant to the thermal situation of the cable.

*Alternating current or direct current.

†The alterations were necessary, as the precise design of the original cable used as the inspiration for the FEM models herein is protected intellectual property.

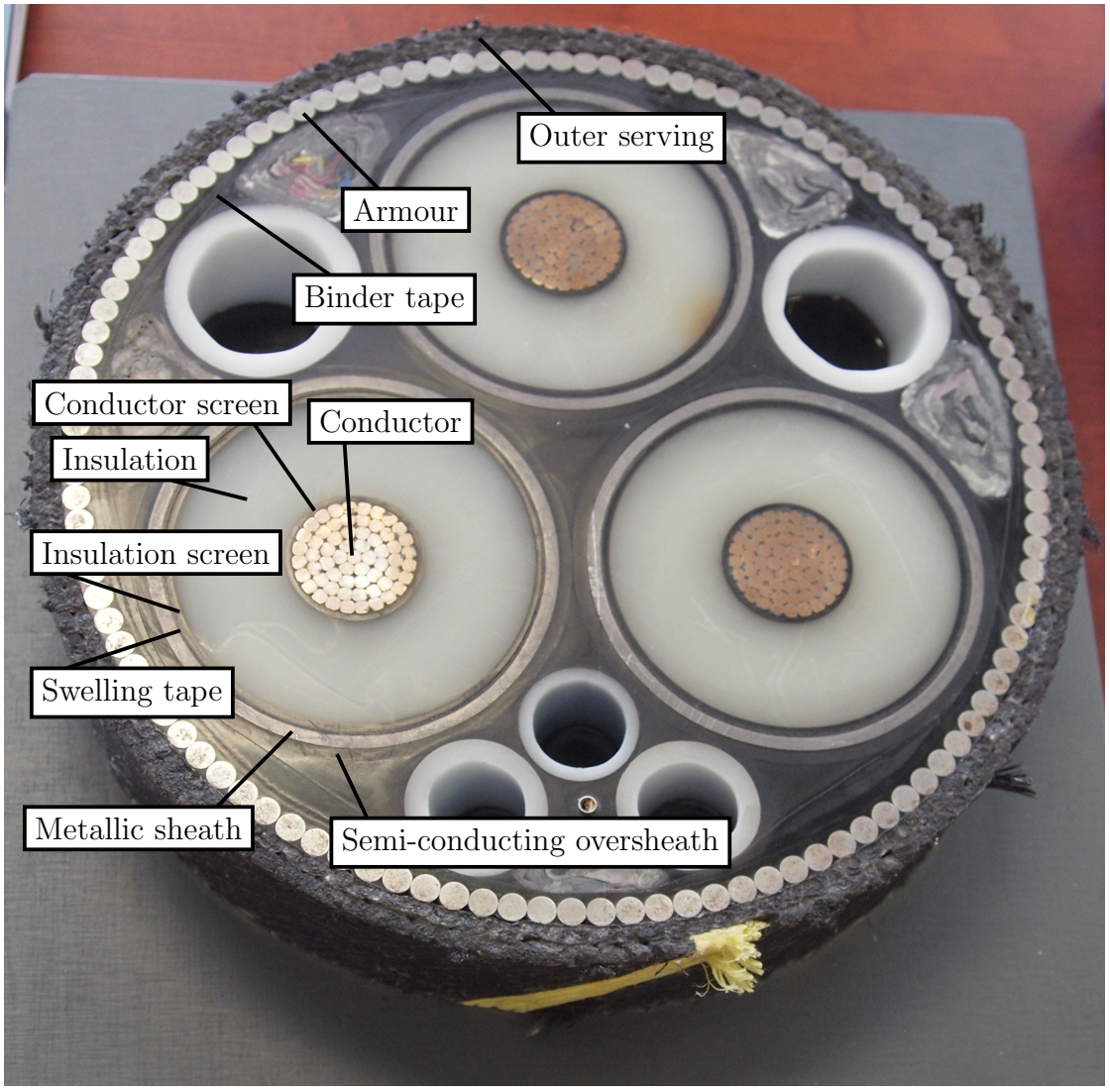

Fig. 2.1: A three phase SL-type HV cable. This particular example is a 245 kV cable used in the Wolfe Island Wind Project, Canada. Labelled are the main cable components. This image is licensed under CC BY-SA 3.0, and has been modified from the original (accessed: 2016-01-26 ∼11:40 UTC) provided by wikipedia user Z22, under the same licence.

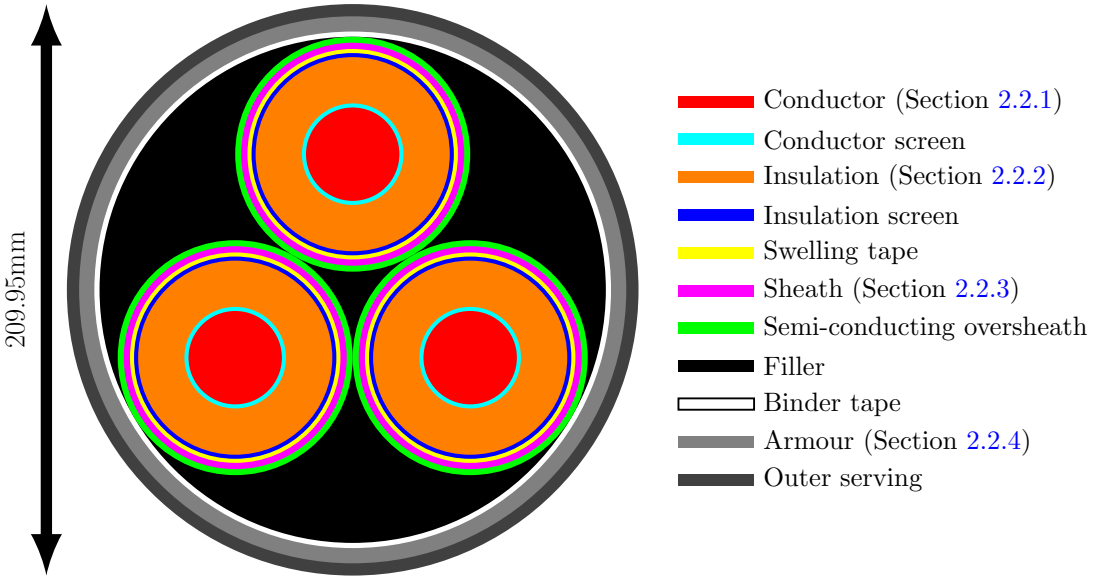

Fig. 2.2: Example cross-section schematic of a three phase SL-type 132 kV cable. The design and component geometry is identical to that used in the FEM simulations in Chapters 4 - 6.

2.2.1 Cable Conductor

At the centre of the cable lies the conductor, which is the component responsible for the transmission of power along the cable. When selecting a material for the cable conductors, a careful balance must be struck between the cost of the raw materials used in construction, and the cost of a higher proportion of losses during transmission. For example, silver has a very low resistivity ($\sim 1.59 \cdot 10^{-8}$ Ωm[44]), but its cost is prohibitively expensive to consider for use when required in large quantities (*i.e.* for HV cables).[46]

The only materials currently used for large scale cable applications are copper (with a resistivity of $1.72 \cdot 10^{-8}$ Ωm[46,48]), and aluminium (with a resistivity of $2.80 \cdot 10^{-8}$ Ωm[46,48]). It is worth noting that, while copper has a slightly lower resistance than aluminium, it is also a lot more dense and costly. Despite a cable with an aluminium conductor requiring a larger cross-section than one with a copper conductor, the mass of material required for manufacture will be lower for an aluminium conductor (by a factor as much as a half[48]). Additionally, the logistical cost associated with cable installation may be larger for cables with copper conductors than those with aluminium conductors.[48]

In addition to Joule heating, HVAC cables incur additional losses (dependent on the topology and geometry of the conductor) compared with HVDC cables (see

Section 2.4). Altering the design of the conductor topology can aid in mitigating the physical processes responsible for causing these additional losses. Commonly used in many modern HV cables,[49–51] Milliken conductors (see Figure 2.3) are one example of a conductor topology arrangement designed specifically to do this.

The design involves partitioning the conductor into numerous stranded wires, which are arranged into identical axisymmetric segments (also called sectors) around the cable axis that are electrically insulated from each other. Each segment contains a number of layers, which are also insulated from each other. Within each layer, all strands are insulated from adjacent strands of the same layer. The strands comprising the layer are arranged in a helical configuration so that as they propagate along the cable axis, each strand precesses around the layer. This distributes the current as evenly as possible throughout all of the strands in the layer.[4,52]

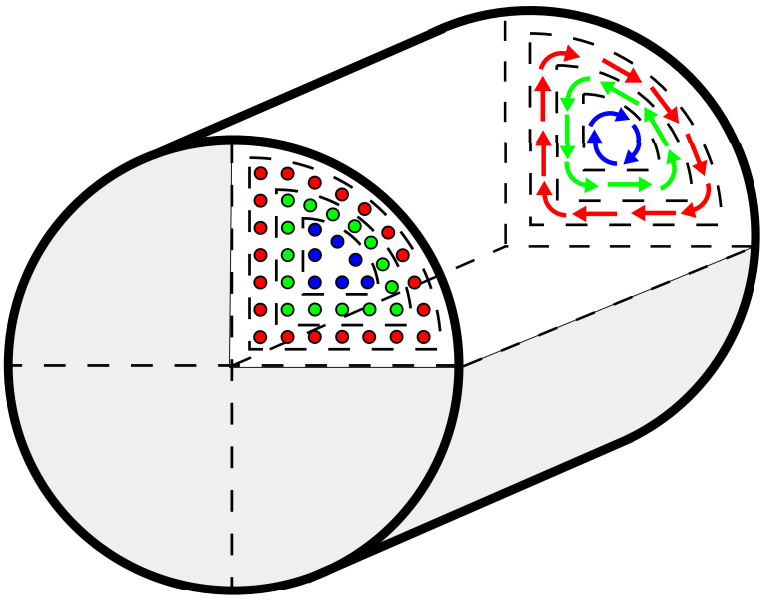

Fig. 2.3: Example schematic of a Milliken conductor segment. The dots on the near face represent wire strands, with different colours for the different layers. The far face illustrates the polarisation of each layer's helix configuration arrangement. The dashed lines indicate where insulation is located.

2.2.2 Insulation

The primary function of the insulation is to prevent current flow in directions other than along the cable axis. It provides a barrier between the conductor, and external surfaces with considerably lower electric potentials. It is vital that the

cable insulation is kept completely homogeneous, and that the material selected for the insulation is both mechanically durable, and resistant to thermal ageing. To encourage homogeneity, a conductor screen is included to smooth the interface between the conductor and insulation. This is usually composed of a similar material to the insulation itself.

Cross-linked polyethylene (XLPE) is currently the preferred insulation material for submarine HV power cables.[4,46] XLPE is manufactured by cross-linking its constituent polymer chains to form an intricate molecular network. This cross-linking allows the material to withstand higher temperatures than normal polyethylene (which melts when heated to 80 - 110 °C depending on density) before becoming unstable.[4] XLPE insulated cables consequently have a higher operating temperature (90 °C[4]) than cables that use previous incarnations of insulation materials.

2.2.3 Metallic Sheath

Outside of the insulation, a metallic sheath is included. This internally constrains the electric field and simultaneously ensures that the field across the dielectric is uniform. The metallic sheath also prevents leakage current from reaching the external environment by providing a path to earth. In fact, the thickness of the sheath is determined by considering the potential rise in temperature (and resulting damage to thermally connected components) from Joule losses in the sheath in the event of a fault current being transmitted along it.[53] Another important function of the sheath is that it acts as a radial water barrier,[4] preventing water from reaching the XLPE insulation and initiating water treeing (defects in the insulation resembling trees that gradually propagate in the presence of water) which can damage the insulation.[54] A secondary function of the metallic sheath is to provide a limited amount of mechanical protection for the encased components.[4] These sheaths are often made from lead, aluminium, or copper, although other metals can also be used.

2.2.4 Armouring

Most of the internal mechanical protection is provided by the cable armouring. For cables with multiple cores, the armouring usually encases all of the cores, rather than having separate armouring for each core. The armouring is provided by metal strands wound around the cable core(s) in a helical configuration.[4] The

material most commonly used for the metal armour strands is galvanised steel,[46] however other metals can be used, including: aluminium, copper, brass, bronze, and stainless steel.[4,46]

Additional losses are induced in the armouring of HVAC submarine cables if they are constructed from magnetic materials (*e.g.* steel). The cause of these losses originates from the time varying magnetic field (originating from the current direction reversals in AC transmission), which induces currents in the armour. These currents are subject to the losses arising from the same physical mechanisms as the main flow of current in the conductors. The effect is explained in more detail in Section 2.4.

2.3 Installation Procedure

Historically, cables were placed on the seabed, often with no external protection at all. However, as potentially hazardous fishing equipment has got heavier over time[4] and the frequency of cable failures due to external damage has risen, external mechanical protection in addition to the cable armouring has become increasingly necessary and prevalent. It is extremely rare for a contemporary cable to be installed without including some form of external mechanical protection,[4] either through burial into the sediment or by covering the cable with boulders in locations where the nature of the seabed makes direct burial impractical.

Damages to submarine telecommunications cables can be attributed to a range of different causes. The two most commonly reported are: fishing activity such as trawling, and anchor impacts.[55–59] It is not known whether the causes of submarine HV cable failures will follow the same trends. However, there are anecdotes of damage to submarine power cables being attributed to these causes,[4,55,57,58] and others including: ship hulls severing cables (when running aground and sinking), damage during installation, landslides (from direct impacts and induced turbidity currents), and volcanic activity.[4] In early unarmoured cables, there are even reports of failures caused by shark bites, although contemporary cables are not considered to be at risk.

The most widespread preventative measure against damage caused by one of the occurrences detailed above is to bury the cable beneath the seabed surface. This can be done either during, or after the cable has been laid. A variety of tools and techniques exist to facilitate the burial of these cables. Sediment can be cleared

using ploughs, or high pressure water jets. Often, remotely operated underwater vehicals (ROVs) are used to to help with the logistics of burial.

Submarine HV cables are usually initially buried at a depth between 0.5 and 1.5 m.[4,55] However, it is important to note that the seabed environment can be highly volatile, with the potential for rapid movement of the overlying sediment. In Section 1.1.3 it was noted that local bed level heights can be altered by many metres in a single year.[31] Cables buried in such an environment may consequently find themselves exposed directly to the seawater on timescales as short as years, months, or even shorter.[60] In extreme circumstances, cables may even become free spanning over a void in the seabed surface, resulting in additional mechanical stresses being placed on the cable components.

2.4 Calculation of Cable Losses

At the beginning of this chapter in Section 2.1, it was explained that when energy is transmitted along electrical cables, inevitably some of the transmitted energy is lost to the environment as heat arising from Joule heating in the conductor. The Joule losses are given by equation (2.9), $P_{\text{loss}} = I^2R$, where the resistance, R is a function of temperature. This is because the resistance of a conductor is proportional to the resistivity of the constituent material, which is itself a function of temperature.[42] The reason that the resistivity is dependent on temperature can be derived by considering the quantum mechanical description of electron-phonon interactions, and the dependence of the effective scattering cross-section on temperature.[61,62] The resistivity of a metallic conductor at a given temperature, can be expressed as a polynomial:[42]

$$\rho_e(T) = \rho_e(T_0)\left(1 + \sum_{i=1}^{\infty} \alpha_i (T - T_0)^i\right) \tag{2.11}$$

where $\rho_e(T_0)$ is the resistivity at some given reference temperature, T_0 and α_i are polynomial coefficients. Taking a first order approximation of this equation yields:

$$\rho_e(T) = \rho_e(T_0)\Big(1 + \alpha(T - T_0)\Big) \tag{2.12}$$

where the subscript from the α_1 coefficient has been dropped. Therefore, the DC resistance as given in equation (2.7) can be expressed as a temperature dependent

function:

$$\begin{aligned} R_{\mathrm{DC}}(T) &= \frac{\rho_e(T_0)\Big(1+\alpha(T-T_0)\Big)\cdot L}{A} \\ &= \frac{\rho_e(T_0)L}{A} + \frac{\rho_e(T_0)L}{A}\cdot\alpha(T-T_0) \\ &= R_{\mathrm{DC}}(T_0) + R_{\mathrm{DC}}(T_0)\alpha(T-T_0) \\ &= R_{\mathrm{DC}}(T_0)\Big(1+\alpha(T-T_0)\Big) \end{aligned} \tag{2.13}$$

which results in the above commonly used equation for the temperature dependence of the resistance of a cable.[27,42,63]

HVDC cables only suffer Joule losses in the conductor as described by combining equations (2.9) and (2.13). By contrast, HVAC cables experience additional losses. The reason behind these extra loss terms can be attributed to the time varying nature of the electric and magnetic fields when using alternating current. When these fields vary in time, eddy currents are produced in the current carrying conductor. Currents are also induced in the other metallic components of the cable, which themselves then experience Joule heating.

Ampère's law (with Maxwell's correction) in the integral form is:[42,44]

$$\oint_C \mathbf{B}\cdot d\mathbf{l} = \iint_S \mu_{\mathrm{B}}\left(\mathbf{J}+\varepsilon\frac{\partial\mathbf{E}}{\partial t}\right)\cdot d\mathbf{A} \tag{2.14}$$

where $\mathbf{B}$ [T], μ_{B} [kgmC^{-2}], $\mathbf{J}$, and ε [C^{2}s^{2}kg^{-1}m^{-3}] are the magnetic field, the magnetic permeability, the current density, and the electric permittivity respectively. Therefore, any change in the electric field with time (*e.g.* from reversing the direction of current flow in the cable, as with alternating current) will result in an induced magnetic field within the conductor.[44] This induced magnetic field will also vary in time*. However, in an analogous way to Ampère's law above, the integral form of Faraday's law states that a magnetic field that varies in time will induce an electric field.[42,44]

$$\oint_C \mathbf{E}\cdot d\mathbf{l} = -\iint_S \frac{\partial\mathbf{B}}{\partial t}\cdot d\mathbf{A} \tag{2.15}$$

Note the difference in sign between equation (2.14) and equation (2.15). This is crucial, as it implies that the induced electric field will oppose the change in the

*Unless the form of the electric field is such that: $\frac{\partial}{\partial t}\left(\frac{\partial\mathbf{E}}{\partial t}\right)=0$.

magnetic field (and hence any change in the current).[42,44] The resulting eddy currents are still subject to Ohm's law, and lose energy through Joule heating. This effect is the physical origin of the various additional losses associated with transmitting electricity with an alternating current.

2.4.1 Skin Effect

For direct current electricity transmission, the current density is approximately uniform across the conductor.[64] However, when an alternating current is passed along a cable, eddy currents are induced in the conductor itself by the processes described above. The induced magnetic field established by the alternating current is such that the distribution of the resultant induced eddy currents are concentrated more towards the centre of the conductor, and reduce with increasing radial distance.[42] Calculating the exact morphology of the electric field is quite mathematically involved (the solution using cylindrical polar coordinates to describe the cable conductor requires Bessel functions[64,65]). It will suffice to say here that the current decreases significantly from the value at the surface of the conductor as you move towards the cable axis[42,64] (as demonstrated by the calculations in Appendix A). When investigating problems focused on heat generation within cables, the skin effect is often modelled as an increase in the effective resistance of the cable.[27,46]

2.4.2 Proximity Effect

If there are multiple cables carrying an alternating current placed close together, changes in the magnetic field in one wire (caused by the reversal of the direction of current flow) can induce eddy currents in its neighbour, resulting in an anisotropic current density across the surface of the conductor. The magnetic field outside of a cylindrical conductor of radius r' can be calculated from equation (2.14):

$$\begin{aligned} \mathbf{B}(t) \cdot 2\pi r &= \mu_B \left(\mathbf{J}(t) + \varepsilon \frac{\partial \mathbf{E}}{\partial t} \right) \cdot \pi r'^2 \\ \mathbf{B}(t) &= \mu_B \left(\mathbf{J}(t) + \varepsilon \frac{\partial \mathbf{E}}{\partial t} \right) \frac{r'^2}{2r} \end{aligned} \tag{2.16}$$

This demonstrates that the magnetic field strength is inversely proportional to the distance from the cable axis. Hence, the current induced in a neighbouring cylindrical conductor (by variations in the magnetic field resulting from the current

reversals in AC transmission) will be strongest in the region closest to, and weakest in the region furthest from the first conductor. For two parallel cables carrying alternating current in phase, this effect is manifest as a shift of the distribution of the current to the region of the cable most distant from the other cable.[66] The current that the first cable induces in the second opposes its native (in phase) current flow (see Figure 2.4). The strength of the proximity effect between two conductors also increases with transmission frequency.[27,67] In an analogous way to the skin effect, the proximity effect can be treated mathematically as an increase in the cable resistance.[27,68]

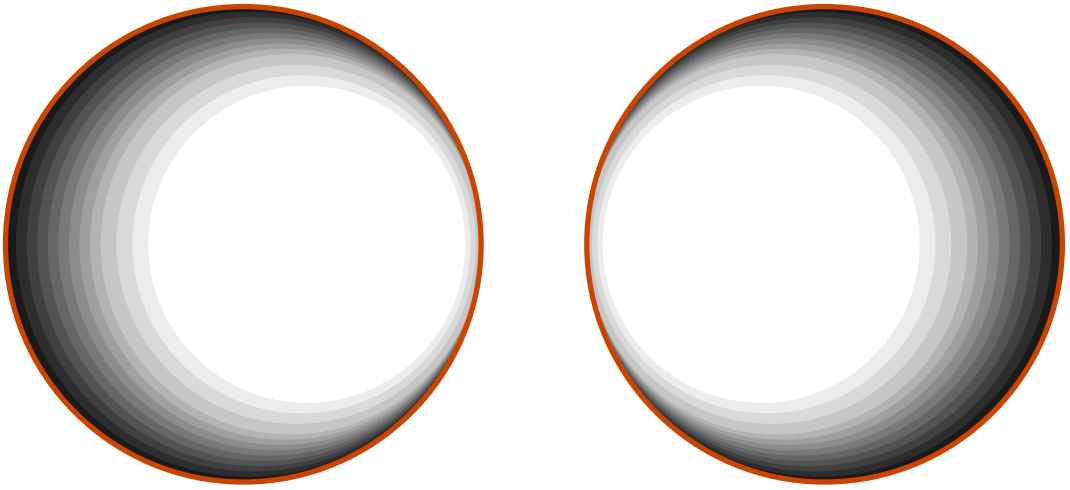

Fig. 2.4: A qualitative example of what happens to the distribution of current in two cables (carrying current of equal magnitude and phase) due to the skin and proximity effects.[68] The darker regions have the highest current density.

The induced magnetic field from current direction reversals can also induce currents in metallic components of the cable other than the conductors (commonly in the core sheaths and cable armour described in sections 2.2.3 and 2.2.4 respectively). When these eddy currents (which also obey Ohm's law) circulate in the aforementioned components, additional heat is generated in these regions of the cable through the skin and proximity effects described above.[22,27]

2.4.3 Dielectric Losses

No dielectric material is a perfect electrical insulator; for HV cables, a small but non-negligible amount of power will also be lost in the cable insulation. When an electric field is applied across a dielectric, molecular electric dipoles (a separation

of positive and negative charges) in the constituent molecules of the dielectric become orientated anti-parallel to the applied field. These dipoles can either be a natural consequence of an inhomogeneous charge distribution within the molecules, or induced by the applied field itself on normally non-polar molecules.[42] The polarisation perturbs the net electric field by an amount proportional to the electric susceptibility, χ such that:

$$\begin{aligned} \varepsilon\mathbf{E} &= \varepsilon_0\mathbf{E} + \varepsilon_0\chi\mathbf{E} \\ &= \varepsilon_0(1+\chi)\mathbf{E} \end{aligned} \tag{2.17}$$

where ε_0 is the permittivity of free space. The electric susceptibility is a complex quantity, reflecting the time lag between the electric field reversals and the polarity alignment of the dielectric molecule electric dipoles. Consequently, the permittivity, ε is also complex, and can be written as:

$$\varepsilon = \varepsilon_{\text{re}} + i\varepsilon_{\text{im}} \tag{2.18}$$

The $\varepsilon\partial_t\mathbf{E}$ term in equation (2.14) can be thought of as a separate "displacement current", $\mathbf{J_D}$ (it has the same dimensionality). Hence by considering Ohm's law - equation (2.3), and writing $\partial_t\mathbf{E} = -i\omega\mathbf{E}$, the total current density (including the displacement current) in the integrand from equation (2.14) becomes:

$$\begin{aligned} &\mathbf{J} + (\varepsilon_{\text{re}} + i\varepsilon_{\text{im}}) \cdot \frac{\partial\mathbf{E}}{\partial t} \\ &= \sigma\mathbf{E} + (\varepsilon_{\text{re}} + i\varepsilon_{\text{im}}) \cdot (-i\omega\mathbf{E}) \\ &= \sigma\mathbf{E} + \varepsilon_{\text{im}}\omega\mathbf{E} - i\varepsilon_{\text{re}}\omega\mathbf{E} \end{aligned} \tag{2.19}$$

The $\sigma\mathbf{E}$ term is the Ohmic dissipation within the dielectric (which is small, but non-zero for an imperfect dielectric[66,69]); the $\varepsilon_{\text{im}}\omega\mathbf{E}$ term accounts for the extra losses associated with the dielectric (*e.g.* those originating from the phase lag between electric field and polarisation response).[66,69] The third term describes the lossless displacement current.[69]

Dielectrics are often described in terms of the ratio between the first two, and the third term in equation (2.19),[66,69] which is called the loss tangent (*N.B.* The terms in the numerator of the loss tangent are often combined into an effective conductivity term, $\sigma_{\text{eff}} = \sigma + \omega\varepsilon_{\text{im}}$):

$$\tan(\delta) = \frac{\sigma + \omega\varepsilon_{\text{im}}}{\omega\varepsilon_{\text{re}}} \tag{2.20}$$

This loss tangent describes an angle in the complex plane that represents the actual phase difference between the applied field (and the current density vector, **J**) and the displacement current (see Figure 2.5). The total losses in the dielectric are proportional to the loss tangent (see Section 2.5.1).

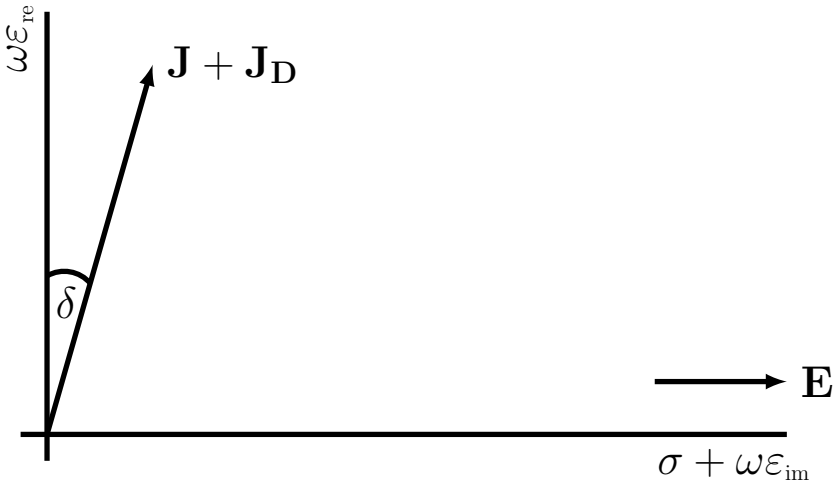

Fig. 2.5: The loss tangent represented geometrically in the complex plane.

2.5 Current Ratings

The amount of power that can be transmitted along an HV cable is usually limited by its maximum operating temperature.[22,70] If a cable insulated with XLPE is exposed to temperatures in excess of the 90 °C limit mentioned in Section 2.2.2, the rate of thermal ageing processes increases dramatically.[4] This thermal ageing can result in a significant reduction in the lifetime of a cable. To prevent this from happening, each cable is given a thermal "current rating", which sets the maximum amount of current that can be safely transmitted along the cable (either under continuous operation, or with a varying current load for a dynamic rating) while remaining below this temperature threshold.

The current ratings of buried HV cables are dependent on a variety of different quantities, including: the thermal properties of both the cable components and the surrounding material, the resistivity and cross-sectional area of the cable conductor(s), the number of conductors/cores in the cable (and their geometric configuration), the geometrical structure of the cable, and the cable burial depth to name a few.

A number of different approaches and procedures have been developed to aid in determining the current rating for cables buried in a variety of different scenarios. By making several assumptions about the problem, the relevant heat transfer equations can be solved analytically. This allows calculation of the current rating by empirically ascertaining the values for the various parameters involved, and subsequently substituting them into an algebraic expression for the current rating.

An alternative method for arriving at a value for the current rating involves solving the differential equations responsible for describing the transfer of heat numerically. This is often done using one of several techniques (*e.g.* finite difference, finite element), using computers to make the calculations. The advantage of this approach to the problem is that it is possible to determine the current rating without having to make as many assumptions as are necessary in the analytical approach.

2.5.1 The IEC 60287 Standard

One of the most commonly used analytical methods for calculating cable current ratings for land-based cables is outlined in the IEC 60287 standard.[27] According to this procedure, the maximum current, I that can be transmitted along an AC cable buried in a soil that will not dry out is given by the following formula:[27]

$$I = \left(\frac{\Delta T - W_d(0.5\tau_1 + N\tau_2 + \tau_3 + \tau_4)}{R_{\mathrm{AC}}\tau_1 + NR_{\mathrm{AC}}(1+\lambda_1)\tau_2 + NR_{\mathrm{AC}}(1+\lambda_1+\lambda_2)(\tau_3+\tau_4)} \right)^{0.5} \tag{2.21}$$

where ΔT is the difference between the rated and ambient temperatures, and W_d is the dielectric loss per unit length per phase for the insulation material around the conductor. τ_i is the thermal resistance per unit length of the corresponding ith material*. The description of the conductive heat flow is split up into four parts in the calculation: from the conductors to sheath (τ_1), from the sheath to the armour (τ_2), through the cable outer serving (τ_3), and through the surrounding burial medium (τ_4). N is the number of conductors in the cable; λ_1 and λ_2 are the ratio of losses from currents induced in one sheath, and in the armour (by a single cable conductor) to the losses in one conductor respectively. R_{AC} is the cable AC

**N.B.*: Some of the notation has been altered from that used in the IEC 60287 standard to avoid duplication of symbol definitions used later in this thesis. In the source document, the symbols: T_i, n, and $\Delta\theta$ are respectively used in place of τ_i, N, and ΔT in equation (2.21)

resistance per unit length, which is given by the following equation:[27]

$$R_{\mathrm{AC}} = R_{\mathrm{DC}}(T_{\max}) \cdot (1 + y_s + y_p) \tag{2.22}$$

where y_s and y_p (which are both strictly greater than zero) are the contributions to the effective resistance from the skin and proximity effects respectively. $R_{\mathrm{DC}}(T_{\max})$ is the DC resistance of the cable at the maximum operating temperature, which, following from equation (2.12) is given by:[27]

$$R_{\mathrm{DC}}(T_{\max}) = R_{\mathrm{DC}}(T_0)\Big(1 + \alpha(T_{\max} - T_0)\Big) \tag{2.23}$$

where 20 °C is used as the reference temperature, T_0 in the IEC 60287 standard, and $T_{\max}$ is commonly set to 90 °C. For an SL-type cable with three cores arranged in a trefoil formation (similar to the design used in the FEM models developed herein, depicted in Figure 2.2), the skin effect factor, y_s as given in section 2.1.2 of the IEC 60287 standard is:

$$y_s = \frac{x_s^4}{192 + 0.8x_s^4} \tag{2.24}$$

where

$$x_s = \sqrt{\frac{8\pi f}{R_{\mathrm{DC}}(T_{\max})} \cdot 10^{-7} \cdot k_s} \tag{2.25}$$

f is the frequency in Hz, and the coefficient, k_s is dependent on the topological construction of the conductor ($k_s = 1$ in this case). The proximity effect factor, y_p for the same cable design is quoted in section 2.1.4.1 of the IEC 60287 standard:

$$y_p = \frac{x_p^4}{192 + 0.8x_p^4} \cdot \left(\frac{2r_c}{s}\right)^2 \cdot \left(0.312\left(\frac{2r_c}{s}\right)^2 + 1.18 \Bigg/ \left(\frac{x_p^4}{192 + 0.8x_p^4} + 0.27\right)\right) \tag{2.26}$$

where

$$x_p = \sqrt{\frac{8\pi f}{R_{\mathrm{DC}}(T_{\max})} \cdot 10^{-7} \cdot k_p} \tag{2.27}$$

r_c is the radius of the conductor in mm, s is the separation between adjacent conductor axes in mm, and the coefficient k_p is dependent on the topological construction of the conductor ($k_p = 1$ in this case).

The total amount of electrical energy lost as heat per unit length within the insulation W_d, is expressed as the following function proportional to the loss tangent

(see section 2.2 of the IEC 60287 standard[27]):

$$W_d = \omega C U_0^2 \tan(\delta) \tag{2.28}$$

where $\omega = 2\pi f$ is the angular frequency of the system (f is the supply frequency), U_0 is the root mean squared (RMS) AC voltage to earth and C is the capacitance per unit length given by[27]

$$C = \frac{\varepsilon_r}{18 \ln(\frac{d_c}{d_i})} \cdot 10^{-9} \tag{2.29}$$

where ε_r is the relative electric permittivity of the insulation, and d_c and d_i are the diameters of the cable conductor (including the conductor screen, if one is present) and insulation in mm.

The AC cables depicted in Figures 2.1 and 2.2 experience additional losses in the sheath and armour due to the proximity effect described in Section 2.4.2. The sheath loss term in equation (2.21), λ_1 is given by the equation in section 2.3.10 of the IEC 60287 standard:[27]

$$\lambda_1 = \frac{R_s}{R_{\text{AC}}} \cdot \frac{1.5}{1 + (R_s/x)^2} \qquad \text{with } x = 2\omega \ln(2s/d) \cdot 10^{-7} \tag{2.30}$$

where s and d_s are the separation distance between cable axes (in mm) and the sheath diameter (in mm) respectively, and R_s can be calculated iteratively from the following two equations (IEC 60287 section 2.3):

$$R_s = R_s(T_0)\Big(1 + \alpha(T_s - T_0)\Big) \tag{2.31}$$

$$T_s = T_{\text{max}} - (I R_{\text{AC}} + 0.5 W_d)\tau_1 \tag{2.32}$$

The losses in the armour surrounding the three cores can be calculated using the equations in sections 2.4.2.3.1 and 2.4.2.5 of the IEC 60287 standard:[27]

$$\lambda_2 = 1.23 \frac{R_a}{R_{\text{AC}}} \left(\frac{2c}{d_a}\right)^2 \frac{1}{(2.77 R_a 10^6/\omega)^2 + 1} \cdot \left(1 - \frac{R_{\text{AC}}}{R_s}\lambda_1\right) \tag{2.33}$$

where c and d_a are the separation between the conductor axis and the cable axis and the diameter of the armour (both in mm) respectively. R_a can be calculated

iteratively from the following pair of equations (IEC 60287 section 2.4):

$$R_a = R_a(T_0)\Big(1 + \alpha(T_a - T_0)\Big) \tag{2.34}$$

$$T_a = T_{\max}\left((I^2 R_{\mathrm{AC}} + 0.5W_d)\tau_1 + \Big(I^2 R_{\mathrm{AC}}(1+\lambda_1) + 0.5W_d\Big)N\tau_2\right) \tag{2.35}$$

It is interesting to note that the only term in equation (2.21) that is directly related to the properties of the surrounding medium is τ_4. It is, however a very important factor in determining the actual value of the current rating.[39] By investigating the heat flow in the region around the cable numerically, a more accurate current rating can be calculated by addressing some of the uncertainties associated with assuming that the heat flow is totally described by the parameter τ_4 in this domain.

2.5.2 Numerical Methods

One shortfalling of the analytical approach outlined above is that several simplifying assumptions have to be made in order to solve the guiding partial differential equations (PDEs) and arrive at equation (2.21). For example, the ground surface must be assumed to be isothermal, which may not be reasonable in all circumstances (especially for cables buried at shallow depths).[22,40] Of particular relevance to submarine applications is the assumption that the heat transfer is dominated by conductive processes. IEC 60287 does account for moisture migration and cable drying, however the treatment is limited to situations where either:[22,27]

- The soil is completely dry (the thermal resistivity of the soil can be altered accordingly).
- All material contained within a critical isotherm is assumed to be completely dry, while the thermal resistivity of the external soil remains unaffected.

As an alternative to analytical approaches of this nature, numerical techniques are often used to solve the PDEs that describe the dissipation of heat generated within HV cables. This involves using a computer to determine an approximate solution to the equations by iteratively improving on an initial guess. Among the distinct numerical techniques that exist for solving PDEs, some of the most commonly used are: the finite difference method, the finite volume method, and the finite element method.[71] All of the aforementioned techniques have been used to a greater or lesser extent to investigate and refine HV cable ratings procedures.[26,38,39]

In particular, FEM models have been used extensively as an alternative method for obtaining ratings for terrestrial cables.[20,22,37–40]

One convenient advantage of using the finite element method is that it is a lot easier to accurately represent complex geometries compared with both analytical approaches, or other numerical techniques (*e.g.* finite difference method). This feature of FEM modelling makes it ideal for constructing simulations that require (or benefit from) the inclusion of detailed geometrical configurations. This is pertinent to the application of simulating submarine HV cables, as it enables the internal design of the cable components (and their relevant thermal properties) to be rendered in the model directly (despite their diminutive scale in comparison to the size of the simulation domain in its entirety).

By applying finite element techniques to cables in a submarine environment, it is hoped that more accurate and representative current ratings for submarine cables can be calculated, and a better understanding of the thermal environment can be obtained.

2.6 The Finite Element Method

The finite element method is a relatively recent invention. The initial development of the technique began in the 1940s to provide insights into problems in structural mechanics.[72] However, it took until 1960 for the term "finite element method" to be coined.[73] Since then, the technique has benefited (and proliferated) greatly from increases in the accessibility of computing power (and its reduction in costs). It has been applied to an extensive and diverse range of problems including: civil, mechanical, and aerospace engineering, heat transfer, fluid mechanics, electromagnetism, biomechanics, geomagnetics, acoustics, and many more.[71,74] Outlined below is a brief description of the general concepts underlying the finite element method.

The central premise behind the finite element method is that the general solution for a PDE that is defined over a certain continuous domain can be approximated by decomposing the original geometry into a finite number of small, connected subregions called "elements".[75] A number of "nodes" are defined for each element usually at the vertices, or along the edges of the element (although it is possible to include interior nodes). These are the points at which the unknown field variable(s) are to be evaluated.[76] For each element, it is also necessary to

define an "interpolation function", which defines the values of the field variable(s) everywhere between the nodes.[77] Adjacent elements will share nodes located at their vertices or on their edges. This allows continuity of the field variable(s) to be enforced between neighbouring elements (and hence across the entire mesh that represents the geometry of the problem in question). The equations describing the field variable(s) in each element are combined to form a matrix of algebraic simultaneous equations.[71] By explicitly stipulating appropriate boundary conditions for the problem, the collection of equations can be solved to obtain the values of the field variable(s) at the nodal points. Intermediate values can be calculated from the interpolation functions and, if required, secondary quantities can then be calculated from the nodal values of the field variable(s).

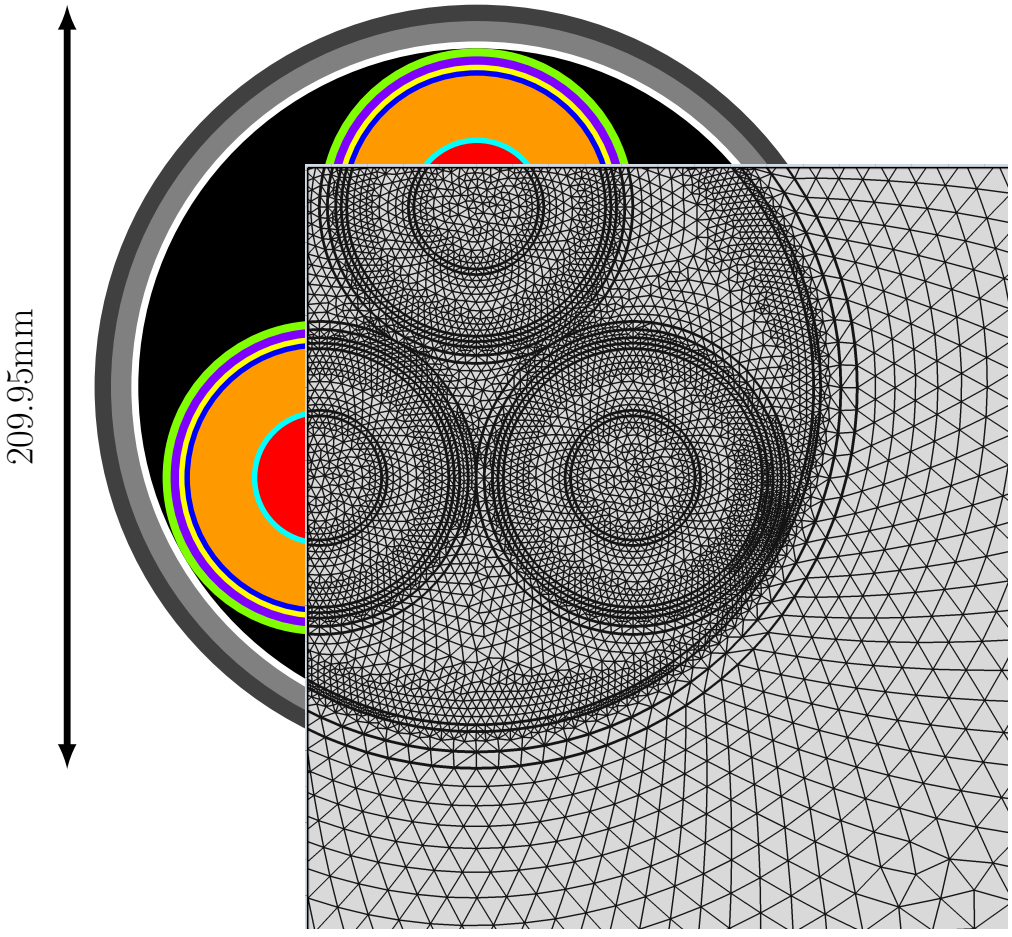

Fig. 2.6: An example FEM mesh for the cable schematic detailed in Figure 2.2. Elements in the mesh can take on different shapes than the triangular form pictured. For example quadrilateral elements are common, as are both tetrahedral and cuboidal (hexahedral) elements for 3D models.[71] *N.B.*: The elements seamlessly wrap around the designated geometry.

Nowadays, there are a number of software packages available that have been designed to aid in the implementation of the finite element method for solving PDEs. These packages offer customisation of the geometry, physics, mesh, and solver techniques to ensure that they are applicable to a broad range of problems. The COMSOL software packages (versions 4.3 and 4.4) have been used for the work contained in this thesis.

CHAPTER 3

Modelling Heat and Fluid Flow in Porous Media

Heat can be transferred by three different methods: conduction, convection, and radiation.[71,78] In a porous medium that is at least partially saturated, there is minimal radiative heat transfer. This is because water is very effective at absorbing radiation in the range of wavelengths likely to be emitted at typical cable surface temperatures (infrared).[24,25] Consequently, conduction and convection are likely to be the only processes that significantly contribute to the transfer of heat within a seabed environment.

3.1 Heat Transfer by Conduction and Convection

Heat conduction is described by the empirically derived Fourier's law:[79]

$$\mathbf{q} = -\lambda \nabla T \tag{3.1}$$

where $\mathbf{q}$ [Wm^{-2}] is the heat flux, and T [K] is temperature*. The parameter λ [$\mathrm{Wm}^{-1}\mathrm{K}^{-1}$] is the thermal conductivity. This quantity is material specific, and characterises how effectively heat can be transferred through a particular medium by conduction. The bulk thermal conductivity of a medium composed of a number of different materials can be determined by considering the relative amounts of each material, and their individual thermal conductivities. Several methods for estimating the bulk thermal conductivity from these quantities are discussed in Section 3.2. The seabed environments that accommodate buried submarine HV cables are relevant examples of a mixed medium, as they consists of a solid matrix of sediment particles and permeant seawater inbetween grains. From here on in, the thermal conductivities of the sediment matrix and the permeant fluid will be denoted by λ_s and λ_f respectively. These subscripts will also be used to refer specifically to other physical properties of the sediment and fluid accordingly. Bulk properties may also be explicitly indicated using a subscript "b", *e.g.* λ_b.

A general expression for describing heat transfer into and out of a Cartesian volume element of porous material comprised of a solid and liquid phase in the rest frame of the solid phase (see Figure 3.1) can be obtained by combining Fourier's law with heat advection and generation terms. The thermal energy per unit volume

N.B.: Of primary concern here are thermal properties relative to their ambient values, hence the quantity T is the difference in temperature to the ambient conditions. This is stated explicitly during the model construction to avoid ambiguities during reproduction of the model.

is:[71]

$$\rho c_p T \tag{3.2}$$

where ρ [kgm^{-3}] and c_p [Jkg^{-1}K^{-1}] are the density and specific heat capacity of the advecting material respectively; as before, T is the temperature.

The change in the amount of heat contained within the volume element denoted by V_f in Figure 3.1 in an infinitesimal time is equal to the amount of heat generated within the volume, minus the conductive and convective dissipation. The total change in thermal energy per with time can be expressed as:

$$\begin{aligned}\iiint_{V_f} \frac{\partial}{\partial t}\left(\rho_b c_{p_b} T\right) dV_f &= \iiint_V Q_{\text{in}} dV_f - \oiint_S \mathbf{q_{cond}} \cdot \hat{\mathbf{n}} dS - \oiint_S \mathbf{q_{conv}} \cdot \hat{\mathbf{n}} dS \\ &= \iiint_{V_f} Q_{\text{in}} dV_f - \oiint_S (-\lambda_b \nabla T) \cdot \hat{\mathbf{n}} dS - \oiint_S (\rho_f c_{p_f} T \mathbf{u}) \cdot \hat{\mathbf{n}} dS\end{aligned} \tag{3.3}$$

where Q_{in} [Wm^{-3}] is the amount of heat generated per unit volume within the element displayed in Figure 3.1. By applying the divergence theorem,[80] the surface integrals of the conductive and convective terms can be restated as a volume integral:

$$\oiint_S (-\lambda_b \nabla T) \cdot \hat{\mathbf{n}} dS = \iiint_{V_f} \nabla \cdot (-\lambda_b \nabla T) dV_f \tag{3.4}$$

$$\oiint_S (\rho_f c_{p_f} T \mathbf{u}) \cdot \hat{\mathbf{n}} dS = \iiint_{V_f} \nabla \cdot (\rho_f c_{p_f} T \mathbf{u}) dV_f \tag{3.5}$$

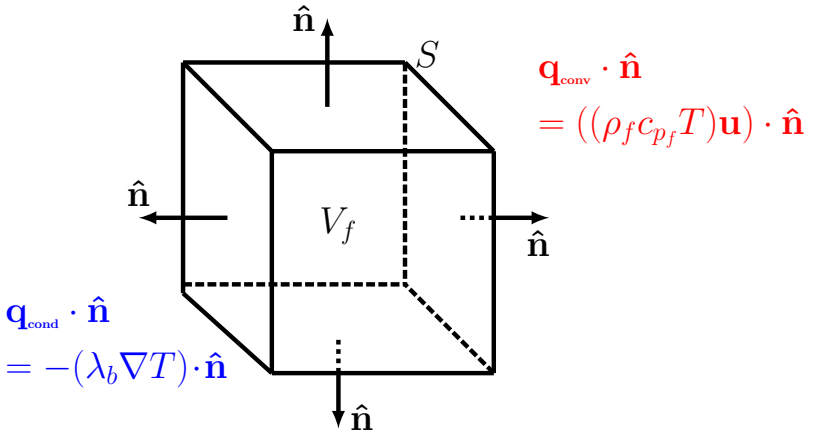

Fig. 3.1: Cartesian volume element with conductive (blue) and convective (red) fluxes through the faces normal to the surface labelled.

Substituting in these terms, equation (3.3) becomes:

$$\begin{aligned}
\iiint_{V_f} \frac{\partial}{\partial t}\Big(\rho_b c_{p_b} T\Big) dV_f &= \iiint_{V_f} \Big(Q_{\text{in}} - \nabla\cdot(-\lambda_b \nabla T) - \nabla\cdot(\rho_f c_{p_f} T\mathbf{u})\Big) dV_f \\
\frac{\partial}{\partial t}\Big(\rho_b c_{p_b} T\Big) V_f &= Q_{\text{in}} V_f + \nabla\cdot(\lambda_b \nabla T) V_f - \nabla\cdot(\rho_f c_{p_f} T\mathbf{u}) V_f \\
\frac{\partial}{\partial t}\Big(\rho_b c_{p_b} T\Big) &= Q_{\text{in}} + \nabla\cdot(\lambda_b \nabla T) - \nabla\cdot(\rho_f c_{p_f} T\mathbf{u}) \qquad (3.6)
\end{aligned}$$

The density and specific heat capacity of the pore fluid are weak functions of temperature themselves, *i.e.* $\rho = \rho\big(T(t)\big)$ and $c_p = c_p\big(T(t)\big)$. Nevertheless, the term on the left hand side of equation (3.6) can be simplified slightly. The chain rule can be employed to expand these terms as follows:

$$\begin{aligned}
\frac{\partial}{\partial t}\Big(\rho_b c_{p_b} T\Big) &= \rho_b c_{p_b} \frac{\partial T}{\partial t} + \rho_b T \frac{\partial c_{p_b}}{\partial T}\frac{\partial T}{\partial t} + c_{p_b} T \frac{\partial \rho_b}{\partial T}\frac{\partial T}{\partial t} \\
&= \left(\rho_b c_{p_b} + \rho_b T \frac{\partial c_{p_b}}{\partial T} + c_{p_b} T \frac{\partial \rho_b}{\partial T}\right)\frac{\partial T}{\partial t} \qquad (3.7)
\end{aligned}$$

By inserting approximate values[81] for the individual phases of the terms ρ_b and c_{p_b} in the expansion given in equation (3.7), it can be shown that the ratio of the first term and the sum of the other two is large:

$$\frac{\rho_i c_{p_i}}{\rho_i T \frac{\partial c_{p_i}}{\partial T} + c_{p_i} T \frac{\partial \rho_i}{\partial T}}$$

N.B.: the temperature here is the value above ambient (10 °C), and not the absolute temperature. For water ($i = f$), this ratio is approximately:[81]

$$\begin{aligned}
&\approx \frac{1000 \cdot 4200}{1000 \cdot (90-10) \cdot 0.9 + 4200 \cdot (90-10) \cdot 0.7} \\
&= \frac{4200000}{307200} \approx 14 >> 1 \qquad (3.8)
\end{aligned}$$

while for a dry porous sediment ($i = s$), it is around:[82,83]

$$\begin{aligned}
&\approx \frac{2500 \cdot 800}{2500 \cdot (90-10) \cdot 1 + 800 \cdot (90-10) \cdot 0.025} \\
&= \frac{2000000}{201600} \approx 9.9 >> 1 \qquad (3.9)
\end{aligned}$$

Therefore, the parameters ρ_b and c_{p_b} can be treated as being approximately independent of temperature, and hence time. One common assumption made in fluid

dynamics calculations is that the fluid is incompressible,[71,84] *i.e.* that $\partial_t \rho_f = 0$ and $\nabla \rho_f = 0$. Another commonly employed assumption in heat transfer problems is that the thermal conductivity of a material is approximately independent of temperature, *i.e.* $\partial_T \lambda_b = 0$.[71,84,85] Making the additional assumption that the bulk thermal conductivity and the specific heat capacity of the fluid are not explicitly dependent on position (*i.e.* $\nabla \lambda_b = \nabla c_{p_f} = 0$; the only variation in density, thermal conductivity, and specific heat capacity in space is a consequence of their variation with temperature, which can be neglected), and making use of the scalar identity $\nabla \cdot \nabla T = \nabla^2 T$,[80] equation (3.6) becomes:

$$\rho_b c_{p_b} \frac{\partial T}{\partial t} = Q_{\text{in}} + \left(\lambda_b \nabla^2 T - \rho_f c_{p_f} \nabla \cdot (\mathbf{u} T) \right) \tag{3.10}$$

By considering mass fluxes across a similar infinitesimal volume to the one illustrated in Figure 3.1, a mass continuity equation can be derived.[71,84] The increase in mass of the volume per unit time is equal to the inflow of matter:

$$\iiint_{V_f} \frac{\partial \rho_f}{\partial t} dV_f = \oiint_S \rho_f \mathbf{u} \cdot (-\hat{\mathbf{n}}) dS \tag{3.11}$$

By again employing the divergence theorem, this becomes:

$$\begin{aligned} \iiint_{V_f} \frac{\partial \rho_f}{\partial t} dV_f &= - \iiint_{V_f} \nabla \cdot (\rho_f \mathbf{u}) dV_f \\ \frac{\partial \rho_f}{\partial t} V_f &= -\nabla \cdot (\rho_f \mathbf{u}) V_f \\ \Rightarrow \frac{\partial \rho_f}{\partial t} + \nabla \cdot (\rho_f \mathbf{u}) &= 0 \end{aligned} \tag{3.12}$$

Note that the integration constant is identically zero, as mass is not spontaneously created. Under the condition of incompressibility previously used to arrive at equation (3.10), equation (3.12) can be reduced to:

$$\begin{aligned} \underbrace{\frac{\partial \rho_f}{\partial t}}_{=0} + \rho_f \nabla \cdot \mathbf{u} + \mathbf{u} \cdot \underbrace{\nabla \rho_f}_{=0} &= 0 \\ \nabla \cdot \mathbf{u} &= 0 \end{aligned} \tag{3.13}$$

In the specific case of steady state ($\partial_t = 0$) heat transfer from conduction (the first term on the right hand side of equation (3.14)) and convection (the second term on the right hand side of equation (3.14)) in the presence of a constant source,

Q_{in} (represented by the term on the left hand side of equation (3.14)), equations (3.10) and (3.13) can be combined to yield:[71,85]

$$Q_{\text{in}} = -\lambda_b \nabla^2 T + \rho_f c_{p_f} (\mathbf{u} \cdot \nabla T + T \nabla \cdot \mathbf{u})$$

$$Q_{\text{in}} = -\lambda_b \nabla^2 T + \rho_f c_{p_f} \mathbf{u} \cdot \nabla T \tag{3.14}$$

Here, only the permeant fluid is involved in any advective contribution to the transfer of heat (hence the density and specific heat capacity in the convective term are fluid properties, denoted by the subscript, f), while conduction is through the entire bulk medium.

When a current is transmitted along an HV cable, some of the energy being transferred is lost as heat generated within the cable conductors, and a number of other cable components. This heat generation is represented in equation (3.14) by the source term, Q_{in}. The amount of heat generated within the cable is related to both the cable current, I, and the cable resistance, R. The reasons for this heat loss, along with some of the existing methods for predicting the locations and relative amounts of heat generation within the cable have been discussed previously, in Chapter 2.

The convective term in equation (3.14) is dependent on the velocity of the fluid, $\mathbf{u}$. Hence, in order to comprehensively describe the transfer of heat through a porous medium, fluid transport within the medium must be fully understood. The equation that describes fluid flow within a porous medium is Darcy's law.[86] This equation is introduced in more detail in Section 3.3.

3.2 Estimating the Thermal Conductivity of a Porous Medium

Submarine HV cables are commonly buried at a depth of around 1 m under the seabed surface.[4] The material into which they are buried will be composed of a solid matrix of sediment grains or rock, as well as infiltrated seawater that is contained within the pore space of the solid matrix.

It can be challenging to determine an effective bulk thermal conductivity, λ_b for a porous medium composed several different materials. This is perhaps due in part to the wide scope of the term "porous", which can be applied to a vast range

of materials with different properties and microstructures.[87] One method might yield accurate results for granular materials while being completely inapplicable to fibrous media for example. The effective bulk thermal conductivity of a porous medium (such as that likely to be encountered by a buried HV cable) will be largely dependent on the spatial distribution and topology of each phase within the mixed medium,[88] the relative proportions of the constituent phases, and the individual conductivities of each phase.[87,89] There are several different methods that have been proposed for estimating the effective thermal conductivity of a porous medium.[87–90]

3.2.1 Upper and Lower Bounds for the Effective Bulk Thermal Conductivity

Making assumptions about the structure of the porous medium can help to determine upper and lower bounds for the actual effective bulk thermal conductivity λ_b.[88,89] Treating the medium as if it consisted of solid and liquid phases in parallel with each other, as illustrated in Figure 3.2(a), gives the upper bound for the bulk thermal conductivity as the weighted arithmetic mean of the contributions from the solid (λ_s) and liquid (λ_f) phases.[89]

$$\lambda_b = (1-n)\lambda_s + n\lambda_f \tag{3.15}$$

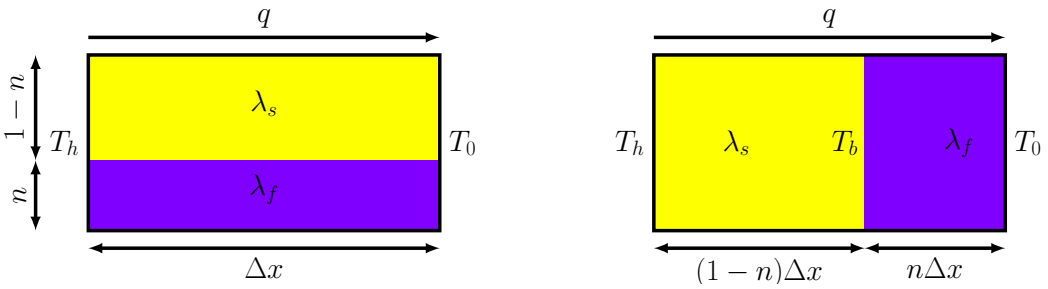

(a) Parallel phases (b) Series phases

Fig. 3.2: Comparison between two different models for estimating bulk thermal conductivity. Figure 3.2(a) assumes that the solid and liquid phases are in parallel, and Figure 3.2(b) that assumes they are in series. If $T_h > T_0$, then heat flows in the direction indicated by the arrows labelled q.

Similarly, the lower bound for λ_b can be derived by treating the two phases as being in series with one another (see Figure 3.2(b)).[89] If energy is being steadily transferred across the porous medium, then the heat flux through the isothermal surfaces labelled in Figure 3.2(b) as T_h, T_b and T_0 is constant and equal. Applying equation (3.1) implies:

$$q = -\lambda_s \frac{T_h - T_b}{(1-n)\Delta x} = -\lambda_f \frac{T_b - T_0}{n\Delta x} \tag{3.16}$$

$$\Rightarrow T_h - T_b = -\frac{q(1-n)\Delta x}{\lambda_s} \text{ and } T_b - T_0 = -\frac{qn\Delta x}{\lambda_f}$$

$$(T_h - T_b) + (T_b - T_0) = -\frac{q(1-n)\Delta x}{\lambda_s} - \frac{qn\Delta x}{\lambda_f}$$

$$T_h - T_0 = -q\Delta x \left(\frac{1-n}{\lambda_s} + \frac{n}{\lambda_f}\right)$$

$$q = -\left(\frac{1-n}{\lambda_s} + \frac{n}{\lambda_f}\right)^{-1} \cdot \frac{T_h - T_0}{\Delta x} \tag{3.17}$$

However, it also follows from equation (3.1) that:

$$q = -\lambda_b \frac{T_h - T_0}{\Delta x} \tag{3.18}$$

and hence by equating the q terms in equations (3.17) and (3.18):

$$\lambda_b = \left(\frac{1-n}{\lambda_s} + \frac{n}{\lambda_f}\right)^{-1}$$

$$\lambda_b = \frac{\lambda_s \lambda_f}{(1-n)\lambda_f + n\lambda_s} \tag{3.19}$$

This estimate for the bulk thermal conductivity is called the weighted harmonic mean. In reality, the actual structure of any porous medium will lie somewhere in between the parallel and series scenarios. Several methods of estimating the bulk thermal conductivity of a porous medium have been developed, many of them have been developed and optimised for application to porous media with a specific topological arrangement.

One method that is commonly used for estimating the thermal conductivity of a granular porous medium saturated with water is the geometric mean:[88,89,91,92]

$$\lambda_b = \lambda_s^{(1-n)} \lambda^n \tag{3.20}$$

which is commonly used if little is known about the microstructure of the porous medium.[88] It should be noted that this method is considered less reliable for dry porous media with pore spaces containing air,[92] or more generally if the ratio between the solid and liquid phase thermal conductivities, λ_s/λ_f exceeds ~ 20.[89] A comparison of the three different aforementioned methods for estimating the bulk thermal conductivity is given in Table 3.1. The table shows that there is a range of possible thermal conductivities of a porous medium for a given porosity. The actual bulk thermal conductivity will depend on the topology of the pore space. For very extreme porosities (either very high, or very low), there is less variation, as the bulk conductivity tends towards the individual conductivity of the more voluminous phase. The variation is maximised at the mid range porosities.

Porosity	**Arithmetic λ_b** $[\mathrm{Wm^{-1}K^{-1}}]$	**Geometric λ_b** $[\mathrm{Wm^{-1}K^{-1}}]$	**Harmonic λ_b** $[\mathrm{Wm^{-1}K^{-1}}]$
0.0	1.00	1.00	1.00
0.1	0.960	0.950	0.938
0.2	0.920	0.903	0.882
0.3	0.880	0.858	0.833
0.4	0.840	0.815	0.789
0.5	0.800	0.775	0.750
0.6	0.760	0.736	0.714
0.7	0.720	0.699	0.682
0.8	0.680	0.665	0.652
0.9	0.640	0.631	0.625
1.0	0.600	0.600	0.600

Table 3.1: Example bulk thermal conductivities calculated using three different estimation methods, given $\lambda_s = 1.0\ \mathrm{Wm^{-1}K^{-1}}$ and $\lambda_f = 0.60\ \mathrm{Wm^{-1}K^{-1}}$.

3.3 Darcy's Law

Quantitative evaluation of the convective contributions to heat transfer away from submarine HV cables relies on having a good understanding of the dynamics of fluids while contained within porous media. Stated another way, a necessary precondition of evaluating the rightmost term in equation (3.14) is the capability to evaluate the velocity field term, $\mathbf{u}$.

The equation that describes the motion of fluid within a porous medium is Darcy's law. This equation was originally derived by Henry Darcy as an empirical relation to describe the volumetric flux of fluid, Φ [m^3s^{-1}] through a block of porous material with a constant cross-section:[93,94]

$$\Phi = -\frac{\kappa g \rho A}{\mu}\frac{\Delta h_h}{L} \tag{3.21}$$

Here, g [ms^{-2}], A [m^2], μ [$Pa \cdot s$], h_h [m], and L [m] are the acceleration due to gravity, the cross-sectional area of the porous sample, the dynamic viscosity of the fluid, the hydraulic head, and the length of the sample respectively. The quantity κ [m^2] is the "intrinsic permeability" of the medium*. This parameter characterises the resistance to fluid flow. An extended discussion of the permeability, its significance to the problem of heat dissipation from submarine HV cables, and how it can be quantified is detailed in Section 3.5.

A theoretical basis for Darcy's law has since been developed. The general equation of motion for incompressible fluids (analogous to Newton's second law of motion for solid objects[98]) is the Navier-Stokes equation:[84]

$$\rho\left(\frac{\partial \mathbf{u}}{\partial t} + (\mathbf{u}\cdot\nabla)\mathbf{u}\right) = -\nabla p + g\rho\hat{\mathbf{y}} + \mu\nabla^2\mathbf{u} \tag{3.22}$$

where p [Pa] is pressure. As mentioned earlier at the beginning of Chapter 3, under the assumption of incompressibility, the mass continuity equation given in equation (3.12) implies that the fluid velocity field is non-divergent, *i.e.* $\nabla\cdot\mathbf{u} = 0$. If the nature of the fluid flow is additionally assumed to be steady (such that $\partial_t\mathbf{u} = 0$), and creeping (such that it can safely be assumed that terms that are nonlinear in $\mathbf{u}$ can be neglected[84]), equation (3.22) becomes:

$$0 = -\nabla p + g\rho\hat{\mathbf{y}} + \mu\nabla^2\mathbf{u} \tag{3.23}$$

as the $(\mathbf{u}\cdot\nabla)\mathbf{u}$ term is of order $\rho u^2/L$ (where L is some characteristic length scale[84,86] which, in the case of a granular porous medium is given by some representative grain size of the sediment), while $\mu\nabla^2\mathbf{u}$ is of order $\mu u/L^2$. The dimensionless ratio between these two terms is called the Reynolds number, and

*This term, κ is often referred to simply as the "permeability". The label "intrinsic" is given explicitly here to distinguish it from the hydraulic conductivity (also called the "coefficient of permeability"[95]), K [ms^{-1}], which is also sometimes referred to as the permeability.[96,97] The term "permeability" will hereafter refer to the intrinsic permeability unless explicitly stated otherwise.

represents the ratio of inertial to viscous forces. As such, it also serves to characterise the degree to which turbulent phenomena will be present in a particular fluid flow regime.

$$\mathcal{R}_e = \frac{\rho u L}{\mu} \tag{3.24}$$

Equation (3.23) is also known as Stoke's equation,[99] and describes creeping fluid flow at low velocities (that is to say, for flows with a low Reynolds number). The next step involves heuristically expressing the viscous forces as being negatively proportional to the flow velocity, *i.e.*:

$$\mu\nabla^2\mathbf{u} = -\mu n(\boldsymbol{\kappa})^{-1}\mathbf{u} \tag{3.25}$$

Here, $\boldsymbol{\kappa}$ [m^2] is a second rank contravariant tensor called the permeability tensor. The porosity, n is also included in the equation to account for the fact that the fluid is only flowing through part of the medium (the void space, and not the solid matrix). The areal and volumetric porosities are equal,[86] hence flow through a porous cross-section is proportional to n. Substituting this alternative term into equation (3.23) yields:

$$0 = -\nabla p + g\rho\hat{\mathbf{y}} - \mu n\boldsymbol{\kappa}^{-1}\mathbf{u} \tag{3.26}$$

A change of variables can be made to reduce the number of terms in this equation. Substituting $P = p + g\rho h_h = p + g\rho y$ (where $g\rho h_h$ is the pressure due to the hydraulic head, h_h) into equation (3.26) gives:

$$\begin{aligned} 0 &= -\nabla(P - \rho g y) + g\rho\hat{\mathbf{y}} - \mu n\boldsymbol{\kappa}^{-1}\mathbf{u} \\ 0 &= -\nabla P - g\rho + g\rho - \mu n\boldsymbol{\kappa}^{-1}\mathbf{u} \\ \Rightarrow \mu n\boldsymbol{\kappa}^{-1}\mathbf{u} &= -\nabla P \end{aligned} \tag{3.27}$$

Rearranging for the velocity yields:

$$\mathbf{u} = -\frac{\boldsymbol{\kappa}}{\mu n}\nabla P \tag{3.28}$$

N.B. For the remainder of the thesis, unless explicitly stated otherwise, the permeability shall be assumed to be isotropic. This allows the tensor quantity discussed above to be described completely by a scalar, κ if the respective bases are chosen such that $\kappa^{ij} = \kappa\delta^{ij}$. In this case, equation (3.28) can be expressed alternatively as:

$$\mathbf{u} = -\frac{\kappa}{\mu n}\nabla P \tag{3.29}$$

Equation (3.29) can also be expressed in terms of the total discharge through a cross-section (with area A m^2) of the porous medium[86] by noting that $\mathbf{u}$ is the velocity averaged over the entire bulk medium and hence the discharge per unit area is $\boldsymbol{\phi} = \mathbf{u} \cdot n$, and $\boldsymbol{\phi} = \boldsymbol{\Phi}/A$:

$$\boldsymbol{\Phi} = -\frac{A}{\mu}\boldsymbol{\kappa}\nabla P \tag{3.30}$$

where $\boldsymbol{\Phi}$ [m^{3}s^{-1}] is the total discharge per unit time. This is an equivalent form of Darcy's law to the empirical one quoted in equation (3.21)

The velocity field of the seawater contained within a porous sediment can be perturbed through inhomogeneous heating of the bulk medium (for example, from the conduction of heat generated within a submarine HV cable through its outer surface). Heating the seawater causes it to expand, reducing its density.[81,100,101] As a result of this expansion, a buoyancy force is induced in the fluid.

The coefficient of thermal expansion, β [K^{-1}] characterises the extent of the expansion of a material due to heating. It is defined in terms of the volume, V_f, and temperature, T as follows:

$$\beta = \frac{1}{V_f}\frac{\partial V_f}{\partial T} \tag{3.31}$$

$$\Rightarrow \delta V_f = V_{f_0}\beta\delta T \qquad \text{where } V_{f_0} = V_f(T_0) \tag{3.32}$$

Hence the density, ρ_f [kgm^{-3}] can be expressed as:

$$\begin{aligned}\rho_f &= \frac{m}{V_f} = \frac{m}{V_{f_0} + \delta V_f} \\ &= \frac{m}{V_{f_0} + V_{f_0}\beta\delta T} = \frac{m}{V_{f_0}} \cdot \frac{1}{(1+\beta\delta T)} \\ &\approx \rho_{f_0} \cdot (1 - \beta\delta T)\end{aligned} \tag{3.33}$$

where the last line follows from taking the binomial expansion of the term $(1+\beta\delta T)^{-1}$ and ignoring terms higher than first order in $\beta\delta T$.

The Rayleigh number, $\mathcal{R}_a$ is another dimensionless number that characterises the relative proportions of thermal energy that are transmitted through a fluid medium by convection and conduction. Below a certain critical value, most heat is conducted through the fluid. Once the critical Rayleigh number is reached, however, most heat is transferred by convection. The Rayleigh number can be thought of as

the product of the ratio of buoyancy to viscous forces, and the ratio of momentum diffusivity (μ/ρ_f) to thermal diffusivity ($\lambda_f/c_{p_f}\rho_f$):

$$\mathcal{R}_a = \frac{\text{Buoyancy forces}}{\text{Viscous forces}} \cdot \frac{\text{Momentum diffusivity}}{\text{Thermal diffusivity}}$$

For a horizontal layer of porous material heated from below with thickness b, and constant top and bottom temperatures, T_1 and T_0 (where $T_1 > T_0$), the Rayleigh number is:[85,86]

$$\mathcal{R}_a = \frac{\kappa c_{p_f} g \rho_f^2 \beta (T_1 - T_0) b}{\mu \lambda_b} \tag{3.34}$$

Equation (3.34), while geometrically distinct from the scenario of a buried HV cable, is helpful for qualitatively considering how each parameter is likely to affect the dynamics of heat flow in general. A full simulation of the relevant PDEs will provide a more in depth analysis of the particular case of heat dissipation from a buried submarine HV cable.

3.4 Sensitivity Analysis

To establish which parameters are likely to have the most influence on the nature of the heat transfer in and around the buried HV cable, a literature review was carried out to investigate the relevant quantities, and the typical ranges they might have in the marine environment. The quantities included in equations (3.14) and (3.29) were investigated. The findings are summarised in Table 3.2. The variation in the fluid properties is derived from the weak dependence on temperature that each of these quantities exhibits. The variations in the density and the coefficient of thermal expansion listed in the table are for pure water (measured values of these parameters for pure water are much more readily available, especially at higher temperatures). The values of these parameters for a given temperature will differ slightly from those of pure water. However, equations of state for the density of seawater (expressed in terms of temperature and salinity) suggest that its overall range is similar to the density of pure water.[102,103]

Parameter	Units	Lower Bound	Upper Bound	Range
b[31]	[m]	~ 0.25*	5	19
β[104]	[K^{-1}]	$8.80 \cdot 10^{-5}$	$6.96 \cdot 10^{-4}$	6.9
c_{p_f}[81]	[$Jkg^{-1}K^{-1}$]	4190	4210	0.0031
κ[86]	[m^2]	10^{-18}	10^{-7}	10^{11}
λ_f[81]	[$Wm^{-1}K^{-1}$]	0.580	0.675	0.16
λ_s[105,106]	[$Wm^{-1}K^{-1}$]	0.8	3.11	2.9
μ[81]	[$kgm^{-1}s^{-1}$]	$3.15 \cdot 10^{-4}$	0.00131	3.2
n[107,108]	-	0.30	0.61	1.0
ρ_f[81]	[kgm^{-3}]	965	1000	0.036

Table 3.2: Ranges of the various parameters relevant to heat transfer away from submarine HV cables. The range column is calculated by taking the difference of the upper and lower bounds, and normalising by the lower bound.

It is clear from Table 3.2 that the permeability can take on a range of values over many more orders of magnitude than any other quantity. With the exception of the dynamic viscosity and volumetric coefficient of thermal expansion, all of the quantities that are properties of the fluid have a comparatively small range of potential values compared with the other environmental variables that are independent of the nature of the fluid.

According to equation (3.34), if only the dynamic viscosity is considered, increasing the fluid temperature from ambient only serves to accentuate any convective behaviour (and help to reduce the temperature of the cable) as the viscosity is correspondingly reduced.[109] Increasing the local permeant fluid temperature also increases the volumetric coefficient of thermal expansion;[104] this will only aggravate any convective dissipation within the porous medium. According to equation (3.57), in the case of a temperature dependent coefficient of thermal expansion, the density contrast between the heated fluid and fluid at ambient temperature within the FEM simulations would be greater than an estimate using a constant value for β (based on its value at a low temperature) that is insensitive to temperature. Furthermore, both the dynamic viscosity and the coefficient of thermal expansion can only influence the convective component of heat transfer. However, owing to its superior range the permeability is expected to have a much greater influence

*This minimum value for b is enforced to ensure that the topology of the cable/sediment system is consistent (*i.e.* the cable remains buried, and is not directly exposed to the overlying seawater).

in determining the magnitude of the convective contribution to the dissipation of heat.

Although the porosity appears to have less influence over the system than some of the other environmental parameters (*e.g.* burial depth), several of the other quantities listed in Table 3.2 are themselves functions of the porosity, perhaps masking its true significance. Section 3.2 details how the bulk thermal conductivity is dependent on the porosity. The permeability of a sediment is also commonly considered to be a function of porosity; the relationship between these two quantities will be explored further in Section 3.5 below.

Sediments in a marine environment can be altered on a much more dynamic timescale that those on land. For example, migration of sedimentary bedforms can result in relative increases and decreases in the local seabed level height of up to several metres per year,[31] a phenomenon that does not occur in the comparatively static terrestrial environment. This implies that a cable that is originally buried at a certain depth may not remain buried at that depth below the seabed-seawater interface indefinitely. Any change in the cable burial depth is equivalent to altering the temperature gradient term in equation (3.14).

3.4.1 Prioritising Parameters for Investigation

Of all the bulk properties of the medium, the permeability exhibits by far the largest range, while the others (solid phase thermal conductivity and porosity) still have more variation than any of the permeant fluid parameters except the dynamic viscosity. The cable burial depth may also exhibit significant variation. These four parameters are also the ones which can be controlled the most (or rather, they are all properties that can vary significantly between different locations on the seabed independent of the thermal conditions), for example by selecting a route that runs through sediment of a particular permeability or thermal conductivity.

For the above reasons, the primary focus of the initial FEM models was to investigate how the nature of the heat dissipation is affected by variances in the permeability. A secondary priority was placed on assessing the impact of varying the porosity, solid phase thermal conductivity, and burial depth on HV cable temperatures.

3.5 Permeability

For an isotropic medium, the permeability, κ [m^2] is defined as the constant of proportionality in equation (3.30), the Darcy equation. It is a function of the properties of the porous medium only, and not of the permeant fluid.[110] Contributions to the thermal behaviour from the nature of the permeant fluid are represented through the dynamic viscosity, μ [$kgm^{-1}s^{-1}$] and fluid density, ρ_f [kgm^{-3}] terms. As discussed in Section 3.4, permeability can vary over numerous orders of magnitude between different sediment types. As demonstrated by equation (3.29), the permeability is consequently a significant factor in determining the velocity of permeant fluid contained within the sediment into which HV cables are buried, and hence the degree to which heat can be transferred away from the cable by convection.

It is therefore important that the permeabilities used in the FEM model developed herein are representative of the range of real sediment permeabilities that submarine HV cables might be expected to encounter. Unfortunately, permeabilities for real marine sediments are often difficult to evaluate. There are several different ways in which this problem can be addressed: *in situ* measurements of the permeability may be taken directly, or experiments may be performed in the lab to measure fluid flow through a sediment sample. Methods for measuring the *in situ* permeability of a marine sediment include:

- Recording the time taken for a water tracer to reach an observation point after release from a source (in conjunction with Darcy's law).[111] Alternatively, the concentration of the tracer can be measured over time, as it dilutes through the permeable medium.
- A "piezocone" can also be used. This apparatus essentially consists of a cone attached to a cylindrical shaft. The contraption is inserted into the sediment, which generates a pressure gradient within the sediment pores. The rate at which this excess pressure is dissipated is related to the permeability.[112]
- Permeability can also be predicted to within an order of magnitude using electrical resistivity measurements of the medium.[113,114] The electricity flow through a saturated medium is predominantly through the pore capillaries. Hence electricity flow can be thought of as being analogous to fluid flow.

Alternatively, the permeability can be estimated using empirical, or semi-empirical relationships that relate it to other, more easily measurable and conceptually

straightforward quantities. Each technique suffers from its own drawbacks. For example, it can be difficult to take core samples in a way that does not alter the permeability of the sample during extraction, transportation, and/or later analysis.[86,110] Additionally, for the experimental methods, the permeability may only be evaluated at discrete locations where a measurement has been taken, or a core has been extracted (not continuously across an entire sediment bed). Some detail may be lost when using these techniques, as transitions between different sediments on the shelf can occur very rapidly, over short length scales. In some regions around the UK, significant variations in sediment type can occur on length scales of metres to hundreds of metres.[29,30]

Owing to the desire to keep the applicability and descriptiveness of the FEM model as general as possible at this early stage in the research, it was decided that initially, the model permeability would be characterised using the latter approach. Estimating the permeability from other environmental parameters ensures that the model is able to encompass the widest possible range of typical sediment types found on the UK shelf.

3.5.1 Estimating Permeability

Over the years, many different relationships have been proposed for the task of estimating the permeability of a sediment from various other geophysical properties. However, the task is far from straightforward as the permeability of a porous medium depends on a number of different factors. These factors include:

- Grain size.[86]
- Porosity.[86]
- Grain sorting.[115]
- Packing.[116]
- Grain shape.[86]
- Grain size distribution.[117]
- Degree of cementation of the sediment.[96]
- Tortuosity of the path taken by the fluid through the porous medium.[116]

Developing a predictive equation to relate permeability to these quantities is made especially hard, as a lot of these quantities are covariant to a certain extent. For example, a sediment with a very wide particle size distribution is likely to have a lower porosity than a sediment composed of uniform grains, as the small grains can occupy the void space between the larger grains (see Figure 3.3). Often, estimation of the permeability involves examining its explicit functional dependence on one or two of the aforementioned parameters, while simultaneously considering some or all additional factors through a constant which may be determined empirically or semi-empirically.

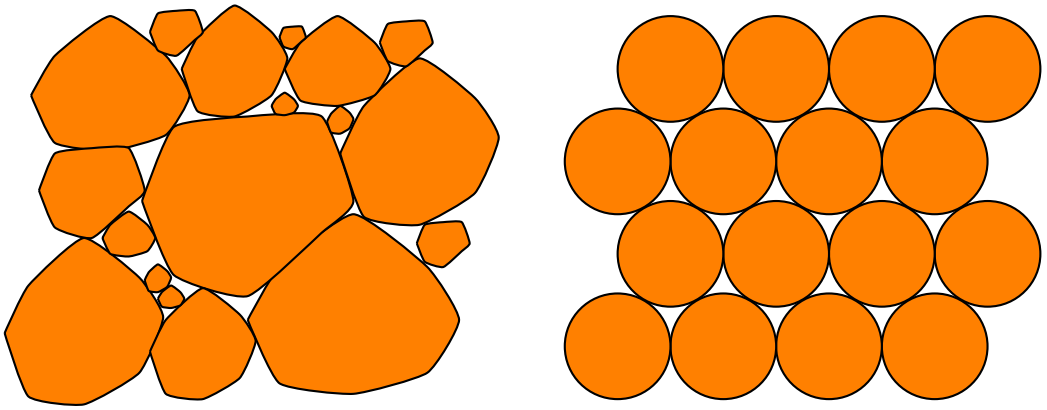

Fig. 3.3: The potential variation in the physical characteristics of a sediment are illustrated here. One sediment is composed of poorly sorted, randomly packed angular grains that have a wide size distribution. The other is composed of uniform close-packed spherical grains.

3.5.1.1 Theoretical Justification for $\kappa \propto d^2$

Most relations give $\kappa \propto d^2$ (at least approximately). Aside from simple dimensional arguments (*i.e.* κ has units of m^2), a theoretical basis for the dependence of the permeability on the square of the grain size can be derived (provided the porous medium conforms to certain conditions) by considering the analogy between fluid flow through porous media and Hagen-Poiseuille flow through a circular pipe.[86,118]

Direct comparison between Darcy and Hagen-Poiseuille flow relies on the assumption that a porous medium can be approximated (albeit crudely) by flow through an ensemble of circular conduits. The general form of the Navier-Stokes equation for an incompressible fluid is:[84]

$$\rho\left(\frac{\partial \mathbf{u}}{\partial t} + (\mathbf{u}\cdot\nabla)\mathbf{u}\right) = -\nabla P + \mu\nabla^2\mathbf{u} \tag{3.35}$$

where the substitution $P = p + \rho g y$ has been made from the previous instance of the Navier-Stokes equation given in equation (3.22). This can be simplified significantly by assuming that:

1. The fluid flow is steady, *i.e.*:
$$\partial_t = 0 \tag{3.36}$$

2. The flow is axisymmetric:
$$\partial_\theta = 0 \tag{3.37}$$

3. Fluid flows in the azimuthal ($\hat{\mathbf{z}}$) direction only:
$$u_r = u_\theta = 0 \tag{3.38}$$

4. The velocity of the fluid has a constant magnitude along the azimuthal direction:
$$\partial_z u_z = 0 \tag{3.39}$$

In cylindrical coordinates, the Laplacian operator is:[119]

$$\begin{aligned}\nabla^2\mathbf{v} = &\left(\frac{\partial^2 v_r}{\partial r^2} + \frac{1}{r}\frac{\partial v_r}{\partial r} - \frac{v_r}{r^2} + \frac{1}{r^2}\frac{\partial^2 v_r}{\partial \theta^2} - \frac{2}{r^2}\frac{\partial v_\theta}{\partial \theta} + \frac{\partial^2 v_r}{\partial z^2}\right)\hat{\mathbf{r}} \\ &+ \left(\frac{\partial^2 v_\theta}{\partial r^2} + \frac{1}{r}\frac{\partial v_\theta}{\partial r} - \frac{v_\theta}{r^2} + \frac{1}{r^2}\frac{\partial^2 v_\theta}{\partial \theta^2} + \frac{2}{r^2}\frac{\partial v_r}{\partial \theta} + \frac{\partial^2 v_\theta}{\partial z^2}\right)\hat{\boldsymbol{\theta}} \\ &+ \left(\frac{\partial^2 v_z}{\partial r^2} + \frac{1}{r}\frac{\partial v_z}{\partial r} + \frac{1}{r^2}\frac{\partial^2 v_z}{\partial \theta^2} + \frac{\partial^2 v_z}{\partial z^2}\right)\hat{\mathbf{z}}\end{aligned} \tag{3.40}$$

Under the assumptions mentioned above, all the terms in the radial and angular directions, $\hat{\mathbf{r}}$ and $\hat{\boldsymbol{\theta}}$ are identically zero. Hence in this case, the vector laplacian reduces to:

$$\begin{aligned}\nabla^2\mathbf{u} = &\left(\cancel{\frac{\partial^2 u_r}{\partial r^2}} + \cancel{\frac{1}{r}\frac{\partial u_r}{\partial r}} - \cancel{\frac{u_r}{r^2}} + \cancel{\frac{1}{r^2}\frac{\partial^2 u_r}{\partial \theta^2}} - \cancel{\frac{2}{r^2}\frac{\partial u_\theta}{\partial \theta}} + \cancel{\frac{\partial^2 u_r}{\partial z^2}}\right)\hat{\mathbf{r}} \\ &+ \left(\cancel{\frac{\partial^2 u_\theta}{\partial r^2}} + \cancel{\frac{1}{r}\frac{\partial u_\theta}{\partial r}} - \cancel{\frac{u_\theta}{r^2}} + \cancel{\frac{1}{r^2}\frac{\partial^2 u_\theta}{\partial \theta^2}} + \cancel{\frac{2}{r^2}\frac{\partial u_r}{\partial \theta}} + \cancel{\frac{\partial^2 u_\theta}{\partial z^2}}\right)\hat{\boldsymbol{\theta}} \\ &+ \left(\frac{\partial^2 u_z}{\partial r^2} + \frac{1}{r}\frac{\partial u_z}{\partial r} + \cancel{\frac{1}{r^2}\frac{\partial^2 u_z}{\partial \theta^2}} + \cancel{\frac{\partial^2 u_z}{\partial z^2}}\right)\hat{\mathbf{z}} \\ &= 0\hat{\mathbf{r}} + 0\hat{\boldsymbol{\theta}} + \left(\frac{\partial^2 u_z}{\partial r^2} + \frac{1}{r}\frac{\partial u_z}{\partial r}\right)\hat{\mathbf{z}}\end{aligned} \tag{3.41}$$

From equation (3.41) and the assumptions given in equations (3.36), (3.37), (3.38), and (3.39) it follows that for the angular component, both sides of equation (3.35) are identically zero:

$$\rho\left(\underbrace{\frac{\partial u_\theta}{\partial t}}_{=0}+(\mathbf{u}\cdot\nabla)\underbrace{u_\theta}_{=0}\right)=-\underbrace{\frac{\partial P}{\partial \theta}}_{=0}+\underbrace{(\mu\nabla^2\mathbf{u})\cdot\hat{\boldsymbol{\theta}}}_{=0} \tag{3.42}$$

The radial component becomes:

$$\begin{aligned}\rho\left(\underbrace{\frac{\partial u_r}{\partial t}}_{=0}+(\mathbf{u}\cdot\nabla)\underbrace{u_r}_{=0}\right)&=-\frac{\partial P}{\partial r}+\underbrace{(\mu\nabla^2\mathbf{u})\cdot\hat{\boldsymbol{r}}}_{=0}\\ 0&=\frac{\partial P}{\partial r}\end{aligned} \tag{3.43}$$

In other words, the pressure is a function of the azimuthal coordinate only:

$$P=P(z) \tag{3.44}$$

Rearranging the reduced form of the vector laplacian in equation (3.41) gives the $\hat{\mathbf{z}}$ component as:

$$\begin{aligned}\rho\left(\underbrace{\frac{\partial u_z}{\partial t}}_{=0}+\underbrace{(\mathbf{u}\cdot\nabla)u_z}_{=0}\right)&=-\frac{\partial P}{\partial z}+(\mu\nabla^2\mathbf{u})\cdot\hat{\boldsymbol{z}}\\ 0&=-\frac{\partial P}{\partial z}+\mu\cdot\frac{1}{r}\frac{\partial}{\partial r}\left(r\frac{\partial u_z}{\partial r}\right)\end{aligned} \tag{3.45}$$

This can be solved by rearranging to isolate the radial differential term, followed by integrating with respect to r:

$$\begin{aligned}\int\frac{\partial}{\partial r}\left(r\frac{\partial u_z}{\partial r}\right)\mathrm{d}r&=\frac{1}{\mu}\int r\frac{\partial P}{\partial z}\mathrm{d}r\\ r\frac{\partial u_z}{\partial r}&=\frac{r^2}{2\mu}\frac{\partial P}{\partial z}+C_0\\ \frac{\partial u_z}{\partial r}&=\frac{r}{2\mu}\frac{\partial P}{\partial z}+\frac{C_0}{r}\end{aligned} \tag{3.46}$$

Subsequent integration of equation (3.46) with respect to r yields:

$$u_z=\frac{r^2}{4\mu}\frac{\partial P}{\partial z}+C_0\ln(r)+C_1 \tag{3.47}$$

The integration constants C_0 and C_1 can be fixed by considering the boundary conditions of the system. One commonly applied constraint is the no-slip boundary condition,[84] which states that the velocity of the fluid is zero at any solid interface. For a cylindrical pipe, this condition can be summarised as:

$$u_z \nrightarrow \infty \text{ at } r = 0 \Rightarrow C_0 = 0 \tag{3.48}$$

$$u_z = 0 \text{ at } r = r' \Rightarrow C_1 = -\frac{1}{4\mu}\frac{\partial P}{\partial z}r'^2 \tag{3.49}$$

where r' is the radius of the pipe. Hence equation (3.47) becomes:

$$u_z = -\frac{1}{4\mu}\frac{\partial P}{\partial z}(r'^2 - r^2) \tag{3.50}$$

The maximum flow velocity is found at the centre of the pipe*, when $r = 0$, and is directly proportional to the square of the radius of the pipe. By considering simple geometrical scenarios, it should be obvious that (at least for uniformly graded sediment) the relation between pore space and grain radii is linear,[120–122] and hence that the permeability is proportional to the square of the grain size.

3.5.1.2 Hazen's Method

One of the first empirical relations of this type was developed by Allen Hazen in 1892. After conducting numerous experiments with filtered sands,[121] he proposed that the permeability is proportional to the square of the grain size. The equation he proposed was:[97,117,123]

$$\kappa = C d_{10}^2 \tag{3.51}$$

where C is an empirical constant, and d_{10} is the sieve size for which only 10% of the sediment (by weight) is able to pass through.[86,97,124] The sediment that Hazen used was uniformly graded. Since then, the range of grain sizes for which Hazen's formula has been demonstrated to be applicable is 0.1 mm $< d_{10} <$ 3 mm,[97,124,125] provided that the coefficient of grain uniformity[126] is less than 5,[124,125] *i.e.*:

$$U = \frac{d_{60}}{d_{10}} < 5 \tag{3.52}$$

Data from different types of sediment result in vastly different values for the empirical constant C. In fact, the range of published values for this parameter in the literature spans more than three orders of magnitude.[97]

N.B. $\partial_z P < 0$

Effective grain sizes other than d_{10} have also been the subject of investigation with respect to Hazen's formula. Among the proposed alternatives are: d_5,[121] d_{17},[121] d_{20},[121] and d_{50}.[126,127] However, these alterations do not provide a significant improvement to the inconsistencies and deficiencies in equations of this functional form that directly relate permeability to grain size only.

Aside from the lack of consensus on the value of the constant C, some studies have questioned the value of the exponent on the grain size as well. Shepherd 1989[117] collected and analysed numerous data sets from sediments with varying characteristics. The exponent on the grain size was empirically found to vary between 1.11 to 2.05, with an average of 1.72. The lowest values for the exponent corresponded to sediments that were less texturally mature (*i.e.* poorly sorted grains whose shape strongly deviated from that of a regular sphere). However, it is worth noting that some of the studies examined by Shepherd have as few as eight data points.

3.5.1.3 The Kozeny-Carman Equation

Most modern attempts to relate the permeability to other properties of the sediment take the functional form:[86]

$$\kappa = f_1(s) f_2(n) d_e^2 \tag{3.53}$$

where f_1 is the "shape factor" that incorporates variables like grain shape and sorting into a single term (this may be determined empirically, theoretically, or using combination of empirical and theoretical methods according to the stipulations of the particular relation used), n is porosity, and d_e is some representative grain size.[86] One of the more well known relations of this form is the Kozeny-Carman equation.[86,97,110,124,128–131] Josef Kozeny originally proposed that fluid flow within a porous medium can be approximated by a series of capillaries of equal length.[132] This concept was expanded upon by Philip Carman[118] to include variations due to factors like grain shape and fluid path tortuosity.[133] The Kozeny-Carman equation is:[86,134]

$$\kappa = \frac{1}{180} \frac{n^3}{(1-n)^2} d_e^2 \tag{3.54}$$

The factor of 180 fulfills the role of the $f_1(s)$ term in equation (3.53), and comes from considering a combination of the surface area of the grains, as well as an empirical coefficient that can be roughly correlated to grain shape;[134] d_m is the mean grain size. Some authors advocate using a different representative grain size that

is calculated from the grain size distribution and surface area instead.[97,128,133,135] For uniform, spherical grains, this distinction makes no difference.

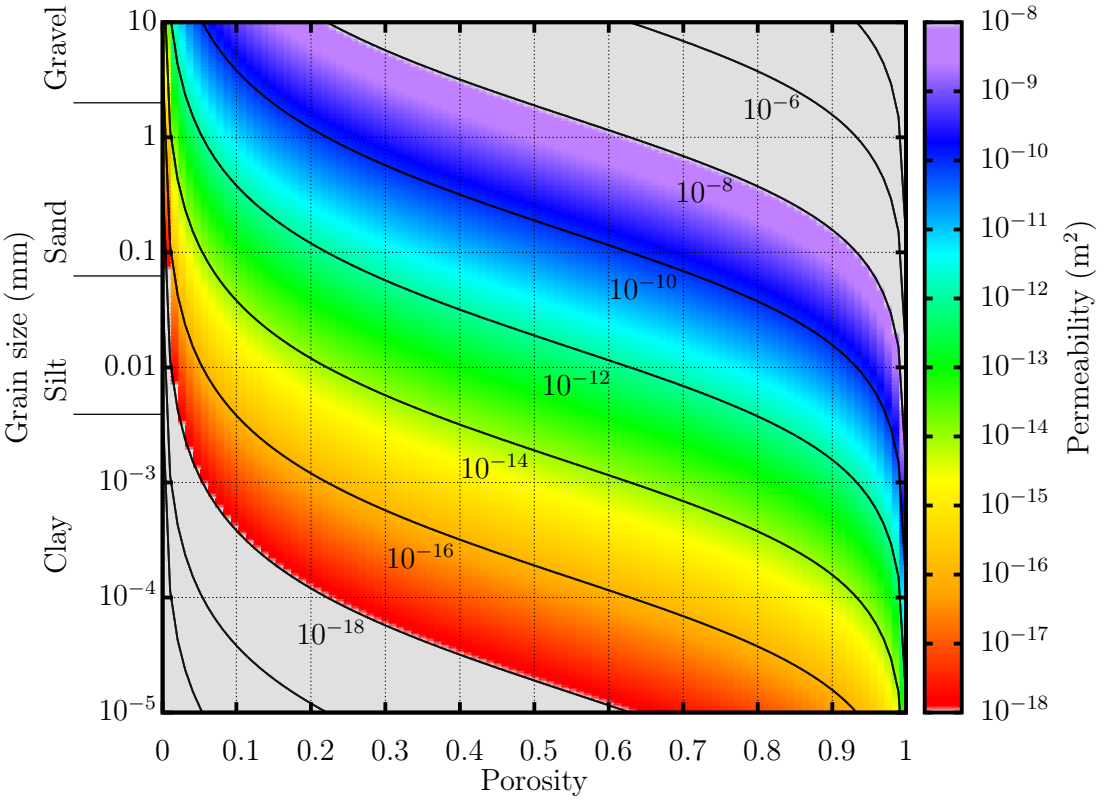

Fig. 3.4: Permeabilities predicted by the Kozeny-Carman equation for different porosities and grain sizes. The grey regions are outside the range of applicability as determined by Chapuis and Aubertin 2003.[133]

Carrier III 2003[97] gives an enthusiastic endorsement for the Kozeny-Carman equation, especially in comparison to the Hazen formula, equation (3.51). Also noted are some parameter ranges for which equation (3.54) is not valid. The formula assumes a laminar flow within the medium (*i.e.* low Reynolds number), and a low velocity within the pores (similar conditions of applicability are described in Section 3.3). Hence for very large grained sediments (gravels with $d_m \gtrsim 3$ mm[124]), the Kozeny-Carman formula cannot be used.

Electrochemical reactions between the soil and the permeant water are also unaccounted for, so equation (3.54) may not be appropriate for describing fine clays either.[97] Fluid flow in fine clays is non-Darcian because these electrochemical reactions produce changes in the effective viscosity of the permeant fluid.[86,97] Carrier III 2003 also states that equation (3.54) is inadequate for describing sediments with extreme particle size distributions (especially those with long tails towards

the fine end of the grain size parameter space), or sediments composed largely of grains whose shape differs considerably from spherical.

Chapuis and Aubertin 2003 provide a similar diagnosis for the Kozeny-Carman equation inasmuch as it seems to be accurate for well sorted mid-range grain sizes.[133] The range over which it is stated to be valid is $1 \cdot 10^{-18}\ \mathrm{m}^2 \lesssim \kappa \lesssim 1 \cdot 10^{-8}\ \mathrm{m}^2$. The inaccuracies are assumed to arise due to theoretical limitations of the equation or difficulties in measuring permeability in the lab, and relating measurements to *in situ* conditions.

3.5.1.4 Other Methods for Estimating κ

In addition to the ones discussed at length in sections 3.5.1.2 and 3.5.1.3, there are many other methods that have been proposed for estimating the permeability of a sediment from its other physical characteristics. Many of them have been developed with a particular type of sediment or range of applicability in mind, or are regarded as being most useful under certain conditions. For example, the Beyer formula is considered useful even for sediments with a highly heterogeneous grain size distribution (with a coefficient of uniformity up to 20).[124] Table 3.3 lists a few of the alternatives, some of which are also displayed in Figure 3.5 as a function of porosity.

Odong 2007 compared the Hazen, Kozeny-Carman, Beyer, Slichter, Terzaghi and USBR formulae to laboratory measurements of permeability for four sediment samples with varying physical properties extracted from cores.[124] It is stated that the USBR formula and Slichter methods (and to a lesser extent, Terzaghi) predict a lower value for the permeability than the other methods, and that these methods are considered inaccurate. The Kozeny-Carman equation was found to be the most reliable method when compared to the experimental values for permeability, but underestimated the permeability for sediments with a wide particle size distribution. The Beyer formula was found to be the most reliable for highly heterogeneous sediments.

Name	Equation	Range (if known)	Notes
Beyer[96,120,124]	$\kappa = C \cdot \log\left(\frac{500}{U}\right) d_{10}^2$	$0.06\text{ mm} < d < 0.6\text{ mm}$ $1 < U < 20$	Detmer 1995 gives $C = 4.5 \cdot 10^{-3}$ [96]
Ergun[136]	$\kappa = \frac{1}{150}\frac{n^3}{(1-n)^2} d^2$		*c.f.* equation (3.54)
Engelund[136]	$\kappa = \frac{1}{1000}\frac{n^2}{(1-n)^3} d^2$		
Koenders[136]	$\kappa = \frac{1}{290}\frac{n^3}{(1-n)^2} d_{15}^2$		*c.f.* equation (3.54)
Den Adel[136]	$\kappa = \frac{1}{160}\frac{n^3}{(1-n)^2} d_{15}^2$		*c.f.* equation (3.54)
Rumpf & Gupte[131]	$\kappa = \frac{n^{5.5} d^2}{5.6}$		
Slichter[125,137]	$\kappa = \frac{711}{C} d_{10}^2$	$0.01\text{ mm} < d < 5\text{ mm}$[124]	For uniform spheres, C=C(n).[125]
Soulsby[136]	$\kappa = \frac{1}{19.8}\frac{n^{4.7}}{(1-n)} d^2$		
Terzaghi[125,138,139]	$\kappa = C\left(\frac{n-0.13}{\sqrt[3]{1-n}}\right)^2 d_{10}^2$		$C \in [0.00613, 0.0107]$ angular $\rightarrow$ round. Applicable to large grains.
USBR[96,124,138]	$\kappa = 4.8 \cdot 10^{-4} d_{20}^{2.3}$	$U < 5$	$\kappa \not\propto f(n)$, $d_e = d_{20}$.

Table 3.3: List of alternative permeability estimation methods.

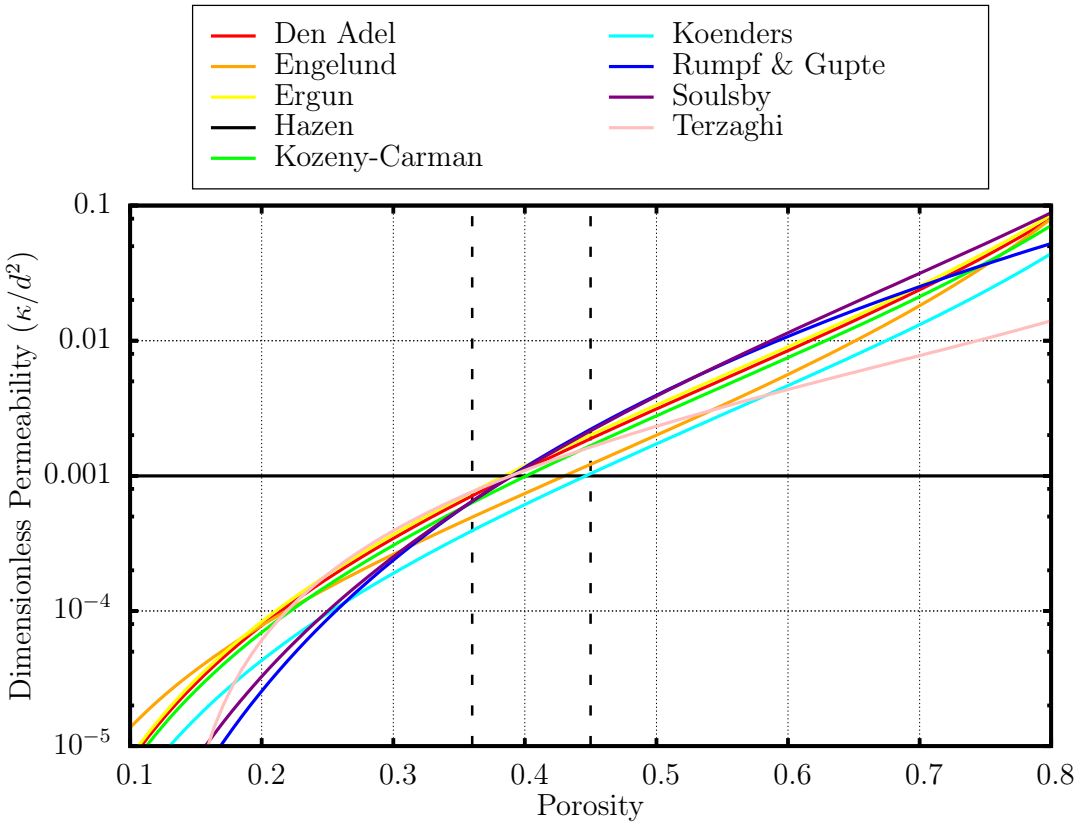

Fig. 3.5: A comparison of some permeability estimation methods listed in Table 3.3 for a uniformly graded sediment with spherical grains. The dashed lines give the porosity limits for random packed uniform spheres.[140]

3.5.1.5 Note for Results

It would be desirable to be able to directly compare the values of the permeability used in the FEM model to the properties of real sediments into which submarine HV cables are buried. This would allow predictions to be made regarding the thermal environment around a submarine HV cable that can be applied in real situations. The easiest and most general way of doing this is to relate the permeabilities used in the FEM model to other quantities of real sediments (porosity and grain size) that are conceptually more intuitive, and often have measurements more readily available. It should also be noted that an additional implicit assumption made in the FEM models is that the simulated sediment is composed of uniform spherical grains. This assumption, in conjunction with the Kozeny-Carman equation - equation (3.54), has been used to convert between the permeability space investigated in the FEM model, and the corresponding approximate grain size space equivalent useful for comparisons to the actual world. This method of estimation was selected over the others described in Section 3.5.1.4 on the testimonies

of Chapuis and Aubertin 2003,[133] Carrier 2003,[97] and Odong 2007.[124] In addition, it is much more prevalent in the wider literature than any of the other methods described in Section 3.5.1.4. For convenience, and to give a sense of scale, the permeabilities as predicted by equation (3.54) for some example grain sizes are listed in Table 3.4.

Wentworth Class[141,142]		**Grain Size** [mm]	**Estimated Permeability** [m^2]
Gravel	Fine pebbles	$(4, 8]$	$(1.58 \cdot 10^{-8}, 6.32 \cdot 10^{-8}]$
	Granules	$(2, 4]$	$(3.95 \cdot 10^{-9}, 1.58 \cdot 10^{-8}]$
Sand	Very coarse	$(1, 2]$	$(9.88 \cdot 10^{-10}, 3.95 \cdot 10^{-9}]$
	Coarse	$(0.5, 1]$	$(2.47 \cdot 10^{-10}, 9.88 \cdot 10^{-10}]$
	Medium	$(0.25, 0.5]$	$(6.17 \cdot 10^{-11}, 2.47 \cdot 10^{-10}]$
	Fine	$(0.125, 0.25]$	$(1.54 \cdot 10^{-11}, 6.17 \cdot 10^{-11}]$
	Very fine	$(0.0625, 0.125]$	$(3.86 \cdot 10^{-12}, 1.54 \cdot 10^{-11}]$
Silt	Coarse	$(0.0313, 0.0625]$	$(9.65 \cdot 10^{-13}, 3.86 \cdot 10^{-12}]$
	Medium	$(0.0156, 0.0313]$	$(2.41 \cdot 10^{-13}, 9.65 \cdot 10^{-13}]$
	Fine	$(7.81 \cdot 10^{-3}, 0.0156]$	$(6.03 \cdot 10^{-14}, 2.41 \cdot 10^{-13}$
	Very fine	$(3.91 \cdot 10^{-3}, 7.81 \cdot 10^{-3}]$	$(1.51 \cdot 10^{-14}, 6.03 \cdot 10^{-14}]$
Clay		$d \leq 3.91 \cdot 10^{-3}$	$\kappa \lesssim 1.51 \cdot 10^{-14}$

Table 3.4: List of estimated permeabilities from grain sizes using equation (3.54) and an assumed example porosity of 0.4. Here, square brackets and parenthesis are used to indicate respectively whether the boundary is explicitly included in, or excluded from the ranges.

3.5.2 Permeability of Marine Sediments

Many of the studies that measure permeability do so only as a means to an end; the permeability is only briefly mentioned, or discussion of its measurement is tangential to the main attention of the work. For example, there are a number of studies that discuss permeability within the context of pore water flow and solute fluxes through marine sands, *etc.*[115,143,144] Huettel *et al.* 1996[143] studied flux of acrylic grains through permeable sediments. Meanwhile, Lowe 1975[145] discusses how sediment properties (including permeability) affect and induce physical

structures within sediment beds (the treatment of permeability is fairly qualitative). Nevertheless, there has been some previous interest focusing more directly on permeability, and methods of determination for marine sands.

For example, Wilson *et al.* 2008[146] examined data from 23 studies to assess the validity of permeability/grain size relations applied specifically to marine sands. The permeabilities of all the undisturbed cores included in this study fall between $2 \cdot 10^{-12}$ and $4 \cdot 10^{-10}$ m^2. Interestingly, the permeabilities of continental sediments seems to be lower (by less than half an order of magnitude) than for near shore sediments of an equivalent grain size. The cause of this difference is speculated to be related to eutrophication, and the changes it causes to the depositional environment. Empirical regression relations perform (more) adequately when data is separated into these different categories. At the opposite end of the permeability range, Chu *et al.* 2002[147] investigated the consolidation and permeability of Singapore marine clays (the given measured values of the permeability are $10^{-17} < \kappa < 10^{-15}$ m^2). It is stated that consolidation generally increases with depth, while permeability generally decreases with depth. The observation of a reduction in permeability with increasing depth has also been made and commented on by Bennett *et al.* 2002.[148] While no correlation between these factors is drawn by the authors, it may hint at an interesting effect of packing and sorting on permeability measurements.

A collection of reported permeabilities for marine sediments is recorded in Table 3.5. It includes both measurements taken *in situ*, and measurements carried out on disturbed sediment, *e.g.* those taken from cores and analysed in a lab. Grain sizes and porosities (where available) are also included for context.

With the range in measured values in Table 3.5 spanning almost ten orders of magnitude (from $2{\cdot}10^{-18}$ m^2 to $\sim 1{\cdot}10^{-8}$ m^2), it is clear that the potential range in the order of magnitude of permeabilities for marine sediments is massive (especially within the context of the comparative ranges of the other parameters relevant to the thermal behaviour of submarine HV cable systems). This is consistent with the value initially used for the sensitivity analysis presented in Section 3.4, which made an heuristic assumption about the likely range in sediment types that might be encountered in the marine environment.

Study	Location	Environment	κ [m^2]	d [mm]	n	Sample
Bennett *et al.* 1990[108]	Great Bahama Bank	Shallow	$3.2 \cdot 10^{-12}$ - $7.0 \cdot 10^{-11}$	57 - 94% $\geq 0.625^*$	0.36 - 0.61	Undisturbed
Bennett *et al.* 2002[148]	Fort Walton Beach, Fl, USA	Shelf	$1 \cdot 10^{-12}$ - $6.1 \cdot 10^{-11}$	0.34 - 0.52	0.38 - 0.48†	Undisturbed
Billerbeck *et al.* 2006[149]	Janssand, North Sea	Intertidal	$5.2 \cdot 10^{-13}$ - $7.2 \cdot 10^{-12}$	-	0.176	Undisturbed
Bolton *et al.* 2000[107]	Woodlark Basin, Papua New Guinea	Shelf	$2 \cdot 10^{-18}$ - $1 \cdot 10^{-16}$	-	0.3 - 0.34	Undisturbed
Chu *et al.* 2002[147]	Singapore	Shallow	$1.0 \cdot 10^{-17}$ - $1.0 \cdot 10^{-15}$	-	-	Undisturbed
Ehrenberg *et al.* 2006[150]	Great Barrier Reef	Shelf	$1 \cdot 10^{-14}$ - $1 \cdot 10^{-8}$‡	-	0.05 - 0.5 ‡	Undisturbed
Forster *et al.* 2003[130]	South Baltic Sea	Shelf	$2 \cdot 10^{-12}$ - $2 \cdot 10^{-11}$	0.15 - 0.24	-	Undisturbed
Franke *et al.* 2006[151]	Lab	Shallow	$1.3 \cdot 10^{-11}$	0.18	0.352	Disturbed
Hamdi & Taylor-Smith 1982[152]	Various	Shelf	$1.0 \cdot 10^{-15}$ - $1.0 \cdot 10^{-12}$	-	0.4 - 0.7	Both
Huettel & Gust 1992[153]	Lab	Shallow	$2.6 \cdot 10^{-15}$ - $1.7 \cdot 10^{-10}$	0.004 - 0.73*	0.317 - 0.810	Disturbed
Huettel *et al.* 1996[143]	Lab	Shallow	$2.9 \cdot 10^{-12}$ - $4.5 \cdot 10^{-12}$	0.25 - 0.30	0.164 - 0.194	Disturbed
Huettel *et al.* 1998[154]	Giglio, Italy	Shallow	$5.1 \cdot 10^{-11}$	0.35	0.4	Disturbed
Huettel & Rusch 2000[155]	Lab & field	Shallow	$2 \cdot 10^{-13}$ - $1.0 \cdot 10^{-9}$	0.105 - 2	0.200 - 0.472	Mix
Huettel *et al.* 2007[156]	Hel, Poland	Shallow	$2.8 \cdot 10^{-11}$ - $3.7 \cdot 10^{-11}$	0.21	-	Undisturbed
Hunter *et al.* 2006[157]	South Atlantic Bight	Shelf	$4.7 \cdot 10^{-11}$	0.5	0.5	Undisturbed
Jahnke *et al.* 2005[158]	South Atlantic Bight	Shelf	$5 \cdot 10^{-11}$	0.505	-	Undisturbed
Janssen *et al.* 2005[144]	German Bight	Shelf	$3.0 \cdot 10^{-12}$ - $7.5 \cdot 10^{-11}$	0.163 - 0.672	0.33 - 0.37	Undisturbed
Precht & Huettel 2004[159]	Giglio, Italy	Shallow	$3.65 \cdot 10^{-10}$	0.370 - 0.500	0.369	Undisturbed
Rasheed *et al.* 2003[160]	Aqaba, Red Sea	Shallow	$1.85 \cdot 10^{-11}$ - $1.43 \cdot 10^{-10}$	0.229 - 0.559	0.33 - 0.47	Mix
Rasheed *et al.* 2004[161]	Great Barrier Reef	Shallow	$1.37 \cdot 10^{-11}$ - $3.75 \cdot 10^{-10}$	0.221 - 0.838	0.413 - 0.427	Disturbed
Reimers *et al.* 2004[162]	Mid Atlantic Bight shelf, USA	Shelf	$2.0 \cdot 10^{-11}$ - $2.4 \cdot 10^{-11}$	0.4 - 0.5	0.37 - 0.38	Undisturbed
Rusch 2000[163]	North Sea	Shallow	$3 \cdot 10^{-12}$ - $2 \cdot 10^{-11}$	0.4 - 0.75	-	Undisturbed
Wild *et al.* 2004[164]	Great Barrier Reef	Shallow	$1.2 \cdot 10^{-10}$	0.838	0.443	Disturbed
Wild *et al.* 2005[165]	Aqaba, Red Sea	Shallow	$2.7 \cdot 10^{-11}$ - $1.16 \cdot 10^{-10}$	0.229 - 0.559	0.35 - 0.44	Undisturbed
Wild *et al.* 2006[166]	Great Barrier Reef	Shallow	$1.7 \cdot 10^{-11}$ - $4.63 \cdot 10^{-10}$	0.221 - 0.829	43.7 - 45.6	Disturbed

Table 3.5: List of measured permeabilities of marine sediments.

*Grain size data is broken down into ranges.
†Estimated from comparison to similar sands.
‡Values estimated from graphs.

3.6 Modelling Heat Transfer from Submarine HV Cables

The finite element method described in Section 2.6 is among the most commonly used techniques for solving problems in both fluid dynamics, and heat transfer.[71] It has been used extensively for investigations of analogous problems involving heat transfer from HV cables buried on land. Making the heuristic judgement that the most natural way to commence the modelling of submarine cable environments is to emulate a familiar approach, it was decided to utilise the finite element method (see Section 2.6) for the foundational basis of the model.

The initial development of this FEM model is based on a scenario in which a submarine HV cable is buried at a depth of 1 m below the surface of the seabed, in a sediment that is perfectly homogeneous with respect to its thermal and physical properties. The simulations were carried out using the COMSOL 4.3 (and later, COMSOL 4.4) software package. Initially, the "double dogleg" solver (which is a combination of the Newton-Raphson and steepest descent methods) was used for the combination of speed and stability characteristic of this method. For some of the less stable situations encountered under more extreme circumstances, a purely non-linear Newton-Raphson solver was used instead to maximise stability.

It is assumed, as a consequence of geometrical homogeneity, that the problem exhibited (at least approximate) continuous translational symmetry (*i.e* there is no change in the thermal behaviour along the cable axis). If multiple cores are contained within the same submarine HV cable, they are arranged in a helical configuration within their mutual outer components.[4] While this introduces a degree of heterogeneity in the axial direction, the length of a single complete turn of the helical structure is typically large compared to the cable radius.[167] In addition, the cable armouring is commonly composed of a material with a comparatively high thermal conductivity, which will encourage a more even distribution of heat across surface of the cable outer serving. The principal novelty of this work is in the attention paid to the nature of the dissipation of heat into the environment (with less emphasis on internal heat transfer within the cable). In this context, a 2D cross-sectional model was deemed to be adequately representative of the thermal conditions in and around real submarine HV cables.

3.6.1 Constructing the Model

3.6.1.1 Equations

The flow of permeant fluid within the porous burial medium is assumed to be well described by Darcy's law, and the burial medium is assumed to remain fully saturated throughout the simulation run due to recharge from the overlying seawater. Consequently, a complete description of the transfer of heat (and fluid) in the situation described above (a homogeneous sediment) can be determined by solving equations (3.14) and (3.29) iteratively in tandem (reproduced here for convenience):

$$Q_{\text{in}} = -\lambda_b \nabla^2 T + \rho_f c_{p_f} \mathbf{u} \cdot \nabla T \qquad \text{where } \mathbf{u} = -\frac{\kappa}{\mu n} \nabla P$$

The substitution $P = p + \rho g y$ was originally made in Section 3.3 for mathematical convenience. By reversing this substitution and evaluating the gradient of the second term, Darcy's law can be expressed in the following form:

$$\begin{aligned} \mathbf{u} &= -\frac{\kappa}{\mu n} \nabla \Big(p + g \rho_f y \Big) \\ &= -\frac{\kappa}{\mu n} \Big(\nabla p + g \rho_f \hat{\mathbf{y}} \Big) \end{aligned} \tag{3.55}$$

To account for buoyancy forces within this Darcian model framework, the gravitational force term in equation (3.55) is altered to include temperature dependent density perturbations of the form:

$$\rho = \rho_0 \cdot (1 - \beta \delta T) \tag{3.56}$$

This essentially amounts to making a Boussinesq approximation;[71,85,100] *i.e.* assuming that all density perturbations are sufficiently small enough that they can be neglected except when calculating these buoyancy forces in the gravitational force term. When included in equation (3.55), it becomes:

$$\mathbf{u} = -\frac{\kappa}{\mu n} \left(\nabla p + g \rho_{f_0} \Big(1 - \beta (T - T_0) \Big) \hat{\mathbf{y}} \right) \tag{3.57}$$

which is the form of the equation that is implemented into the FEM model.

As explained earlier in Section 3.2, the bulk thermal conductivity λ_b can be estimated using a variety of different methods. Table 3.6 shows the results of some preliminary FEM simulations that were conducted to determine how much variation there could be between solutions of simulations that use the arithmetic method, and those that use the harmonic method. The value of the bulk thermal conductivity in each case was calculated using equations (3.15) and (3.19) respectively. This variation was assessed for a representative range of permeabilities (the significance of which will become apparent later), and for sediment porosities of 0.1, 0.4, and 0.7.

Permeability [m^2]	**Porosity** -	**Temperature with λ_b arithmetic λ_b** T [°C]	**Temperature with harmonic λ_b** T [°C]
$1 \cdot 10^{-14}$	0.1	77.4	78.5
	0.4	84.4	88.0
	0.7	93.7	97.4
$1 \cdot 10^{-12}$	0.1	77.3	78.5
	0.4	84.2	87.8
	0.7	93.4	96.9
$1 \cdot 10^{-11}$	0.1	73.9	74.8
	0.4	78.7	81.0
	0.7	84.2	86.1
$1 \cdot 10^{-10}$	0.1	53.6	53.8
	0.4	54.6	55.0
	0.7	55.7	56.1
$1 \cdot 10^{-9}$	0.1	39.4	39.4
	0.4	39.8	40.1
	0.7	40.4	40.6

Table 3.6: Comparison of different methods used for calculating λ_b. *N.B.*: $\lambda_b \to \lambda_s$ as $n \to 0$ for all methods, hence the smaller discrepancy for $n = 0.1$.

Unless otherwise stated, the bulk conductivity in the FEM model is estimated using the arithmetic method, equation (3.15). This method was selected as part of a broader conservative philosophy for considering the additional potential contribution to the dissipation of heat from convection. A robust demonstration that this contribution could be significant (and the development of a procedure for incorporating this additional consideration into cable current rating methodologies)

was judged to be of more value than attaining perfect accuracy in the simulation results, and a perfect correspondence to physical scenarios at this early stage in the work. Recall from Section 3.2 that the arithmetic method presented in equation (3.15) represents the upper bound for the bulk thermal conductivity of a multi-phase medium. Using this upper bound value for the porous sediment in the FEM model ensures that the amount of heat dissipated by conduction errs on the side of overestimation. This can be seen by considering equation (3.14); a larger bulk thermal conductivity, λ_b provides a greater dissipative capacity from conduction. This effectively minimises the convective flux required to reach a steady state for a given set of environmental parameters. If convection is observed in the FEM simulations, underestimation of the conductive flux can be ruled out as a potential alternative explanation for this apparent manifestation of convective phenomena exhibited by the simulation results.

3.6.1.2 Values of Auxiliary Parameters

All of the parameters that were not being specifically investigated were assumed to have a constant value in the FEM simulations. Strictly speaking, this is not true for many of the relevant parameters, as many of them have a weak dependence on temperature. For example, the thermal conductivity of liquid water varies between 0.580 $\mathrm{Wm^{-1}K^{-1}}$ at a temperature of 10 °C and 0.675 $\mathrm{Wm^{-1}K^{-1}}$ at a temperature of 90 °C.[81] However, it is clear from Table 3.2 that changes in the fluid density, fluid thermal conductivity, and fluid specific heat capacity due to temperature variations in the heuristically appropriate range (10 - 90 °C) are negligible when compared to the potential variation in the other environmental parameters which were the subject of the investigations described herein. Hence, they are assumed to be described well in the FEM model by a constant value.

The only variables that vary significantly over the aforementioned temperature range are the dynamic viscosity and volumetric coefficient of thermal expansion of the fluid. Neither of these quantities are influenced by changes in any other environmental parameter. As mentioned in Section 3.4, any changes in these parameters from their ambient value only increases the likelihood of significant convective behaviour. Hence, these parameters were also included within the FEM model as constants to ensure a conservative approach to the prospect of observing convective behaviour within the model. The values of the auxiliary parameters included within the FEM model are summarised in Table 3.7.

Variable Name	Symbol	Value
Burial depth (to cable axis)	b	$[0.5, 5]$ m
Volumetric coefficient of thermal expansion	β	$2.1 \cdot 10^{-4}$ K^{-1}
Fluid specific heat capacity	c_{p_f}	4200Jkg^{-1} K^{-1}
Gravitational acceleration	g	9.81 ms^{-2}
Permeability	κ	$[1 \cdot 10^{-18}, 1 \cdot 10^{-7}]$ m^2
Fluid thermal conductivity	λ_f	0.6 Wm^{-1}K^{-1}
Solid thermal conductivity	λ_s	$[0.25, 4]$ Wm^{-1}K^{-1}
Dynamic viscosity	μ	$1.002 \cdot 10^{-3}$ kgm^{-1}s^{-1}
Porosity	n	$[0.25, 0.7]$
Pressure offset	p_0	101325 Pa*
Total input heat	Q_{in}	100 Wm^{-1}
Fluid density	ρ_f	1000 kgm^{-3}
Ambient temperature	T_0	10 °C
Overlying water velocity	u_0	1 ms^{-1}

Table 3.7: List of parameters used in the FEM model. If a range of values have been used for a particular parameter, an interval is given. The constants used for the properties of water are rounded from their values at 20 °C.

3.6.1.3 Generating the FEM Mesh

The FEM simulations incorporate heat generation and transfer within the cable, and dissipation into the surrounding sediment. Both the cable and its constituent components, and an extensive domain of surrounding sediment material are rendered in the FEM models.

The cable used in the simulations is based on a generic 132 kV three-phase SL-type design. Three cores are arranged in a trefoil formation, encompassed within outer protective layering (as illustrated in Figure 2.2, with the component dimensions given in Table 4.1). This cable is embedded at a depth of b m (initially 1 m) below the top edge of a rectangular domain of porous material, as shown in Figure 4.2. This domain of sediment extends to a distance of 25 m to the left, right and beneath the cable axis. The mesh external to the cable representing the sediment is partitioned into two regions: within 2 m of the cable axis, the resolution of the mesh is made finer in an attempt to fully capture the physics proximal to the cable without compromising too much on simulation run times.

i.e. 1 atmosphere.

In addition to the mesh sensitivity analysis that was carried out as described later in Section 4.2.3, an investigation was conducted to determine an adequate size for the side lengths of the coarse meshed region surrounding the dense meshing in the vicinity of the cable structure in the FEM model. The main porous domain was made as large as illustrated in Figure 4.2 to minimise any effect of the imposed boundary conditions within the simulation, and to distance the area of interest from these edge effects as much as possible. A separate simulation with a reduced spatial extent was run that included elements only up to 20 m below and to the sides of the central cable axis (as opposed to the 25 m shown in Figure 4.2). The temperature field solutions to the two simulations were sampled every 0.1 m in the range $-1 \text{ m} \leq x \leq 1 \text{ m}$ and $-1 \text{ m} \leq y \leq 1 \text{ m}$. The maximum discrepancy found between the two solutions was 0.100 °C. However, the run times for the larger simulations with 25 m of elements around the cable axis were still deemed acceptable, and hence this became the standard simulation geometry.

3.6.1.4 Generation of Heat within the Cable

The heat loss within the cable is partitioned into individual losses in a number of cable components. These losses are calculated according to the IEC 60287 standard (the equations for which are quoted in Section 2.5.1), assuming a total heat loss of 100 Wm^{-1}. The values for the sheath and armour loss factors (λ_1 and λ_2) for the cable geometry used (see Figure 2.2 and Table 4.1) were calculated to be 0.168 and 0.829 respectively. The corresponding total loss in the cable conductors is then 49.5 Wm^{-1} (this loss is spread across all three conductor cores, *i.e.* the loss in each conductor is 49.5/3 Wm^{-1}). Similarly, the loss in each core sheath, the cable armour, and each core insulation are: 2.8 Wm^{-1}, 41.0 Wm^{-1}, and 0.391 Wm^{-1} respectively.

In real (AC) cables, the current density (and hence heat generation) will not be uniform across these components. It will be affected by phenomena such as the skin and proximity effects described earlier in 2.4. It is implicitly assumed that the timescales required to reach an approximate thermal equilibrium (through conduction) within the components that generate significant amounts of heat (namely, the conductors, sheaths, and armour) is very much shorter than the timescales of thermal transport through the other cable components, and the surrounding sediment. Hence in the model, heat is generated homogeneously within the appropriate component domains, according to their respective losses (as described in the previous paragraph).

By considering equation (3.10) under conduction only (sensible for within the cable), and assuming that changes in the density and specific heat capacity are proportionally small compared with changes in temperature, the rate of change of temperature with time is given by:

$$\frac{\partial T}{\partial t} = \frac{\lambda}{\rho c_p} \nabla^2 T \tag{3.58}$$

An insight into the relative rates of heat transfer through different materials can be attained through a comparison of the value of the constant: $\lambda/\rho c_p$ for each material respectively. Table 3.8 summarises some approximate values of this constant for the materials used in the FEM model (the details of which are given in Chapter 4).

Material	$\boldsymbol{\lambda}$ $[\mathrm{Wm^{-1}K^{-1}}]$	$\boldsymbol{\rho}$ $[\mathrm{kgm^{-3}}]$	$\boldsymbol{c_p}$ $[\mathrm{Jkg^{-1}K^{-1}}]$	$\boldsymbol{\lambda/\rho c_p}$ $[\mathrm{m^2s^{-1}}]$	$\frac{\lambda/\rho c_p}{\lambda/\rho c_p(\mathrm{PP})}$
Copper	401 [168]	8960 [168]	385 [168]	$1.06 \cdot 10^{-4}$	906
PE	1/3.5 [27]	~ 945 [168]	~ 2400 [169]	$1.26 \cdot 10^{-7}$	1.07
PP	1/5.5 [27]	~ 925 [168]	1680 [169]	$1.17 \cdot 10^{-7}$	1.00
Lead	35.3 [168]	11300 [168]	130 [168]	$2.40 \cdot 10^{-5}$	205
Stainless Steel	~ 15 [168]	7800 [168]	~ 490 [170]	$3.92 \cdot 10^{-6}$	33.5
Example sand	0.8-3.11 [105,106]	~2200-2900 [136]	700-900 [171]	$3.07\text{-}20.2 \cdot 10^{-7}$	2.79-18.4

Table 3.8: A comparison of heat transfer rates through the different materials used in the FEM model described in Chapter 4. The last column on the right gives $\lambda/\rho c_p$ relative to the value of this quantity for polypropylene.

CHAPTER 4

Effect of Sediment Properties on the Thermal Performance of Submarine HV Cables

The following chapter consists of a reformatted version of the paper:

Hughes, T.J., Henstock, T.J., Pilgrim, J.A., Dix, J.K., Gernon, T.M., Thompson, C.E.L., "Effect of Sediment Properties on the Thermal Performance of Submarine HV Cables", *IEEE Transactions on Power Delivery* **30**(6) p.2443-2450 (2015) DOI:10.1109/TPWRD.2015.2398351.

All material discussed therein is the work of Tim Hughes (supported by his supervisors, the other named authors), except the section entitled: "Impact on Cable Design", which was co-written by James Pilgrim and Tim Hughes.

N.B.: Some of the notation has been altered from the paper version to maintain consistency with the thesis style. Figures 4.4(b) and 4.4(d) have been added to aid with the contextualisation of the transition from conductive to convective thermal behaviour. Figure 4.6(b) has been aesthetically amended from the original.

N.B.: Some of the parameters listed in Tables 4.1 and 4.2 are inconsistent with the values given previously in Tables 3.8 and 3.2 respectively. The correct values are the ones listed in Chapter 3, namely:

- The thermal conductivities of copper, polypropylene, and stainless steel are: 401, 1/5.5, and 15 $Wm^{-1}K^{-1}$ respectively.[168]
- The lower bound for the dynamic viscosity of water is: $3.15{\cdot}10^{-4}$ $Wm^{-1}K^{-1}$.[81]
- The range in permeability is 10^{11} m^2.

Addendum: Figure 4.9 illustrates the extent to which the current rating of a submarine HV cable (represented by the 90 °C isotherm) depends on the permeability of the sediment into which it is buried, according to the FEM model presented in this chapter. It is clear that for cables buried in highly permeable sediments, heat can be dissipated from the cable more efficiently than is suggested by the IEC standard. Consequently, the current rating can be increased considerably.

Abstract: The thermal performance of high voltage submarine cables is controlled by the effectiveness of heat transfer through the sediments in which they are buried. This paper assesses the influence of sediment parameters on this heat transfer using finite element simulations. Particular attention is paid to the role of convective heat transfer, with a method being developed to define installation scenarios where this may become significant. The work shows that the permeability is the dominant factor and can have a significant impact on cable temperatures, even though it is typically neglected in conventional models.

Keywords: Underwater power cables, Finite element methods, Power transmission, Thermal analysis

4.1 Introduction

Determining how heat generated during the transmission of power along HV cables is dissipated in the surrounding environment is vital to ensure prolonged reliable operation of these assets. The thermal behaviour of terrestrial cables has been extensively investigated from both an analytical (e.g. IEC 60287[27]) and numerical perspective, making use of techniques such as the finite difference and finite element methods.[20,40] In contrast, very little work has been conducted specifically into how HV cables perform when buried under the seafloor, despite several key differences between the respective environments. The most conspicuous difference is the presence of a large body of seawater above the marine sediment in which the cable is buried, which acts as a heat sink whose effectiveness is controlled by heat transfer through the sediment. The fluid constituent of the porous medium will be seawater and freshwater for cables buried in the marine and terrestrial environments respectively. The degree of saturation of sediment under the sea is likely to be maintained at a very high level. In addition, the marine environment is subject to change on a much more dynamic timescale. For example, migration of sedimentary bedforms can cause variations in the depth of the seabed of up to $\sim$ 5m over the course of a year,[31] a phenomenon that does not occur in the comparatively static terrestrial environment.

Over its entire length, it is highly likely that a submarine HV cable will encounter a variety of different sediments, each with different thermo-physical properties. For example, around the UK shelf, existing and planned cable routes cross a broad range of substrate types (Figure 1) that so far are considered mainly as affecting ease of burial. On land, the thermal properties of the soil are very influential in

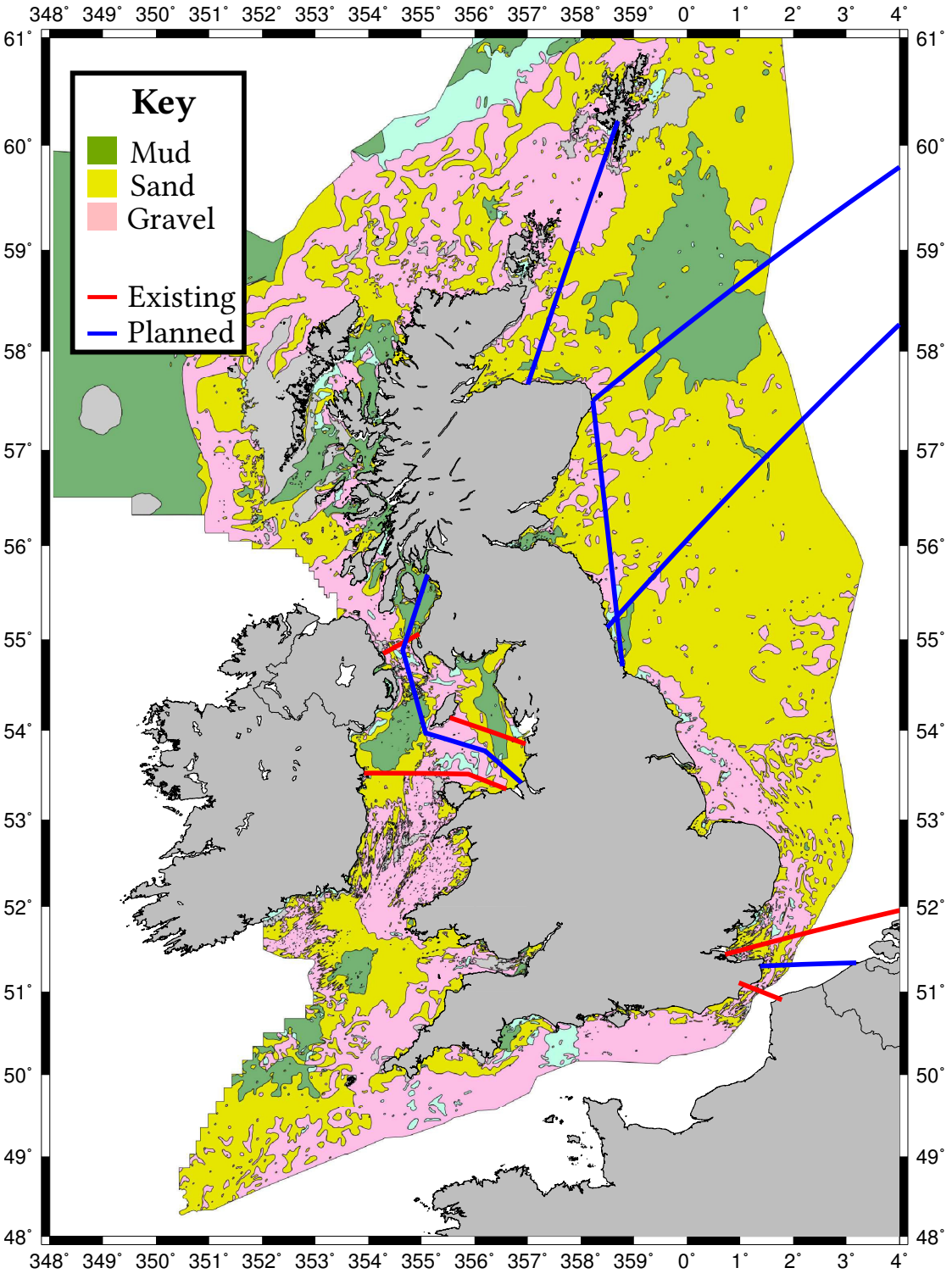

Fig. 4.1: Some existing and planned cable routes around the UK are displayed, along with data on seabed surface sediment types in the region. N.B. Most cables pass through a variety of different types of sediment along their routes. Contains British Geological Survey materials © NERC 2014

determining current ratings for HV cables.[39] In recognition of this, trenches are often backfilled with a material that has a high thermal conductivity to facilitate the dissipation of heat in the surrounding medium. Understanding how these properties affect the transfer of heat through marine sediments is essential for predicting the thermal performance of cables buried at sea.

2D finite element models have been developed using COMSOL 4.3 to investigate conductive and convective heat transfer in marine sediments surrounding HV cables at sub-tidal water depths. A strong emphasis is placed on how the properties of the sediment influence the thermal behaviour of the system, and whether the behaviour of cables under the seafloor is likely to differ significantly from the more familiar terrestrial environment.

4.2 Model Overview

The finite element method has previously been used many times to solve thermal problems relating to power cables buried on land. The same basic principles apply to modelling cables in the marine environment. Both conductive and convective heat transport are accounted for in the model described below by numerically solving time independent coupled fluid flow and heat transfer partial differential equations.

4.2.1 Governing Equations

In a steady state, heat transfer in the presence of a constant source, Q_{in} [$\mathrm{Wm^{-3}}$], can be described by:[71]

$$Q_{in} = -\lambda \nabla^2 T + \rho_f c_{p_f} \mathbf{u} \cdot \nabla T \tag{4.1}$$

where T is temperature [°C], λ bulk thermal conductivity [$\mathrm{Wm^{-1}K^{-1}}$], and ρ_f, c_{p_f} and $\mathbf{u}$ are fluid density [$\mathrm{kgm^{-3}}$], fluid specific heat capacity [$\mathrm{Jkg^{-1}\,°C^{-1}}$], and fluid velocity [$\mathrm{ms^{-1}}$] respectively. The bulk thermal conductivity of the medium can be estimated from the individual thermal conductivities of the fluid (λ_f) and solid phase (λ_s) of the medium, as well as the porosity (which characterises the ratio of water to solid in the medium). There are several different methods proposed for calculating the thermal conductivity of a porous material. This is due in part to the scope of the term "porous", which incorporates a wide range of different

materials with different properties and microstructures. The model uses the simple arithmetic method:[89]

$$\lambda = \lambda_s(1-n) + \lambda_f n \tag{4.2}$$

It is common practise for some thermal resistivity measurements to be made during pre-installation surveys (no measurements are taken during operation). However, these *in situ* measurements may only capture conductive heat transfer due to the methods used.[172]

The two terms on the right hand side of (4.1) represent the contribution of conduction and convection to the total heat transfer. The permeant fluid is assumed to be well described by Darcy's law, such that the velocity in (4.1) is given by:[86]

$$\mathbf{u} = -\frac{1}{n\mu}\boldsymbol{\kappa}\left(\nabla p + \mathbf{g}\rho_f\right) \tag{4.3}$$

where n, μ, $\boldsymbol{\kappa}$, p and $\mathbf{g}$ are the porosity, dynamic viscosity [Pa·s], intrinsic permeability (from here onwards referred to simply as "permeability") tensor [m^2], pressure [Pa] and gravitational acceleration [ms^{-2}] respectively. To account for buoyancy forces within the model, the gravitational force term in (4.3) is altered to include temperature dependent density perturbations of the form $\rho = \rho_0(1-\beta\Delta T)$ (here, β is the volumetric coefficient of thermal expansion [K^{-1}]). This amounts to making a Boussinesq approximation,[100] *i.e.* assuming that all density variations are sufficiently small to be neglected, except when calculating the buoyancy forces in the gravitational force term. The tensor description of the permeability may be reduced if the additional assumptions of isotropy and homogeneity are imposed. In this case, the scalar quantity κ sufficiently describes the permeability of the porous material surrounding the cable such that (4.3) becomes:

$$\mathbf{u} = -\frac{1}{n\mu}\kappa\left(\nabla p + \mathbf{g}\rho_{f_0}\Big(1-\beta(T-T_0)\Big)\right) \tag{4.4}$$

The model assumes that the sediment remains fully saturated with recharge from the overlying seawater irrespective of the properties of the sediment.

Equations (4.1) and (4.4) are the relevant PDEs that describe joint conductive and convective heat flow in the sediment surrounding buried submarine HV cables. They are solved iteratively across a 2D domain that represents an HV cable buried *in situ* (Figure 4.2) using the "double dogleg" solver included in COMSOL 4.3. This solver dynamically combines aspects of both the Newton-Raphson and steepest descent methods to provide a stable, yet efficient solving technique.[173]

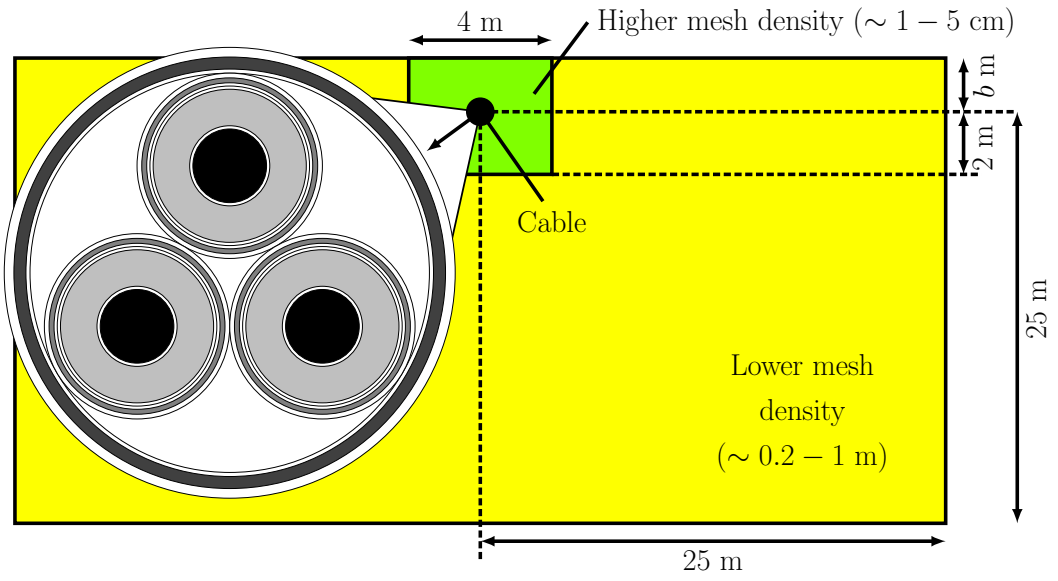

Fig. 4.2: Schematic of the simulation geometry (not to scale). The black dot at the centre represents the cable, the internal structure of which is described in Table 4.1. The shaded sections of the cable cross-section (left) indicate the regions of heat generation (darker shading denotes a higher heat generation).

4.2.2 Internal Heat Transfer within the Cable

Heat transfer within the cable is by conduction only. The internal structure for a generic 132 kV three phase SL-type cable (the details of which are given in Table 4.1) is used to model heat flow through the cable components. Heat is generated in the conductors, metallic sheaths, armouring, and dielectric of the modelled cable. The contributions to heating from these components are calculated using the IEC 60287 standard and enforcing that the sum of all the aforementioned contributions is equal to a constant value of 100 Wm^{-1} (this value was selected as being representative of the possible heat loss of the cable under maximum operational load). Hence, the losses in the conductors are calculated to be 49.497 Wm^{-1}. The ratio of conductor to sheath and armour losses respectively are $\lambda_1 = 0.168$ and $\lambda_2 = 0.829$ (*N.B.* λ_1 and λ_2 here correspond to the loss factor parameters used in the IEC 60287 standard and bear no relation to λ, the thermal conductivity), while the dielectric loss for a single core is $\mathrm{W}_d = 0.391$ Wm^{-1}. Heat is applied homogeneously across the surface area of each component.

Component	**Material**	**λ** [$Wm^{-1}K^{-1}$]	**Diameter** [mm]
Conductor	Copper	400	34.3
Conductor screen	XLPE	1/3.5	37.3
Insulation	XLPE	1/3.5	71.3
Insulation screen	XLPE	1/3.5	74.3
Swelling tape	Polymeric	0.2	77.3
Sheath	Lead	35.3	81.9
Oversheath	PE	1/3.5	86.3
Filler	PP	0.2	N/A
Binder tape	Polymeric	0.2	189.75
Armour	Steel	18	200.95
Outer serving	PP	0.2	209.95

Table 4.1: Relevant geometrical and thermal properties of the constituent components of the generic 132 kV cable design implemented in the FEM model.

4.2.3 Geometry and Mesh

The geometrical setup of the simulation is split up into two parts: the cable, and the surrounding porous matrix of sediment and permeant fluid. It was discovered that the sharpest temperature gradients and largest fluid velocity magnitudes in the porous domain are located in the region directly surrounding the cable. Consequently, an area of denser meshing is included in this region, which helps to sufficiently resolve some of the more sensitive features (particularly in the highly convective simulations). This dense region of meshing extends for two metres to the left, right and below the central cable axis. It accounts for approximately 40% of the total number of mesh elements in the simulation (with elements located in the cable interior accounting for a further 40%).

The maximum element side lengths for the denser region and the surrounding mesh are fixed at 0.05 m and 1 m respectively. A mesh sensitivity analysis was carried out on a representative sample of the simulations by comparing the results to those of an identical simulation with the maximum element side lengths decreased by a factor of two (this increased the number of elements in the simulation from $42,546$ to $99,451$). The simulated temperature field was sampled every 0.1m in the range $-1 \leq x \leq 1$ and $-1 \leq y \leq 1$; the largest discrepancy between the two different solutions was found to be 0.0737 °C (which equates to about a 0.64% difference).

4.2.4 Boundary Conditions

The coarser meshed region of the surrounding sediment is extended to such an extent that small perturbations in the expanse of this domain have no observable influence on the solution of the field variables T and $\mathbf{u}$ in the region of interest directly surrounding the cable.

Identical boundary conditions are placed on the bottom and sides of the coarser meshed domain of porous material. No fluid flow and no heat flux conditions are imposed across these boundaries:

$$\hat{\mathbf{n}} \cdot \mathbf{u} = 0 \text{ and } \hat{\mathbf{n}} \cdot (-\lambda \nabla T) = 0 \tag{4.5}$$

The interface between the cable and the sediment shares this no fluid flow condition, but there is free exchange of heat across the interface between the cable exterior surface and the environment. Conductive transfer within the cable is determined by Fourier's Law:

$$\mathbf{q} = -\lambda \nabla T \tag{4.6}$$

where $\mathbf{q}$ is the local heat flux density [Wm^{-2}]. In the case of a steady state, this results in a constant flux across the exterior cable surface equal to the heat generated within the cable.

The top boundary has a constant pressure condition applied to it (a common boundary condition for buoyancy flow problems[71,174]) that allows fluid flow in both directions across this interface. The heat flux is proportional to the gradient between the local interface temperature (T) and the temperature of the overlying seawater (T_0), and is a function of the velocity of the overlying fluid, u_0. A representative value of 10 °C is used for the temperature of the overlying seawater.

$$p = p_0 \text{ and } \hat{\mathbf{n}} \cdot (-\lambda \nabla T) = h(T - T_0) \tag{4.7}$$

The heat transfer coefficient h describes the rate at which heat can pass across the interface between the porous matrix and the overlying seawater. It can be calculated from the dimensionless Nusselt number, $\mathcal{N}_u$. For a flat plate, the local Nusselt number can be evaluated through a combination of analytical and numerical techniques;[175] the local heat transfer coefficient is then defined as:

$$h = \frac{\lambda}{x}\mathcal{N}_u = 0.332\frac{\lambda}{x} \cdot \left(\frac{c_{p_f}\mu}{\lambda_f}\right)^{\frac{1}{3}} \left(\frac{\rho_f u_0 x}{\mu}\right)^{\frac{1}{2}} \tag{4.8}$$

where x is the position along the boundary [m]. It is evaluated locally along the boundary length to determine the local heat transfer coefficient at each point (rather than taking an average value across the whole boundary edge). The value for the overlying flow velocity is based on an approximation of real marine current,[176] and is large enough that any small perturbation in its magnitude will have a negligible effect on the amount of heat that is able to be transferred across the interface. This boundary is analogous to a wind-cooled ground level interface that is sometimes used when numerically modelling terrestrial buried cables.[40]

4.2.5 Sensitivity Analysis

A brief review of the relevant literature was carried out to investigate the parameters in (4.1) and (4.3), and the typical ranges that they might be expected to have in a marine environment. The findings are summarised in Table 4.2, along with the difference between the upper (U) and lower (L) bounds normalised by the value of the lower bound. Variation in the fluid properties is due to the temperature dependence of these quantities.

Parameter	**Lower bound**	**Upper bound**	$(U-L)/L$
λ_s [$\mathrm{Wm^{-1}K^{-1}}$]	0.8 [105]	3.11 [106]	2.89
λ_f [$\mathrm{Wm^{-1}K^{-1}}$]	0.580 [168]	0.6753 [168]	0.164
ρ_f [$\mathrm{kgm^{-3}}$]	965.3201 [168]	999.6996 [168]	0.0356
c_{p_f}[$\mathrm{Jkg^{-1}\,{}^{\circ}C^{-1}}$]	4192.1 [168]	4205.0 [168]	0.00308
μ [$\mathrm{Pa \cdot s}$]	0.3147 [168]	0.001307 [168]	3.15
κ [$\mathrm{m^2}$]	10^{-18} [86]	10^{-7} [86]	10^{13}

Table 4.2: Range of possible values for each of the relevant parameters in (4.1) and (4.3).

It is clear from Table 4.2 that the permeability can take on a range of values over many more orders of magnitude than any other quantity. The dynamic viscosity and thermal conductivity have comparable ranges. However, the dynamic viscosity is not a property of the burial sediment; increasing the fluid temperature only serves to accentuate any convective behaviour as the viscosity is correspondingly reduced. As mentioned earlier, marine sediments can migrate on a relatively short timescale. Cable systems initially buried at a certain depth under the seafloor may not remain at that depth for long. Varying the burial depth is equivalent to

varying the temperature gradient term in (4.1). These three variables, permeability, thermal conductivity and burial depth exhibit a large amount of variation and are approximately independent of temperature. It is on this basis that they were selected for further investigation.

4.3 Permeability and its Relation to Properties of the Sediment

The permeability, κ is defined[110] as the constant of proportionality in (4.3). It is a function of the properties of the medium only[86] - contributions to behaviour from the permeant fluid are represented through the dynamic viscosity (μ) and fluid density (ρ_f) terms. Permeability can vary over several orders of magnitude between different sediment types, and is therefore likely to be a significant factor in determining the magnitude of the velocity field of the permeant fluid within a particular sediment. As the convective flux in (4.1) is directly proportional to the velocity of the fluid, the permeability is also likely to be a significant factor in determining the degree to which heat can be transferred by convection away from an HV cable buried under the seafloor.

4.3.1 Permeabilities of Real Sediments

Each model uses a fixed *a priori* value for the sediment permeability; in order to apply the results to real cables, it is therefore necessary to determine the permeability of seabed sediments. There are several ways in which this could be accomplished: *in situ* measurements of the permeability can be made directly, core samples can be taken and subsequently analysed in a lab, or it can be estimated from other physical properties using an empirical, or semi-empirical relation.[117]

Each method suffers from its own drawbacks. For example, it can be difficult to take core samples in a way which does not alter the permeability during extraction, transportation, and experimental analysis.[86,110] In addition, permeability can only be obtained at discrete points (where cores are taken), not continuously across an entire sediment bed.

Many different empirical and semi-empirical relationships have been proposed for estimating permeability from other sediment properties. However, the task is

far from straightforward. The permeability depends on a number of parameters (*e.g.* grain size, shape and packing, porosity, pore space connectedness, grain size distribution, *etc.*), and their innate covariance. Most derived relations express the permeability in the form:

$$\kappa = f_1(s) f_2(n) d_{\text{eff}}^2 \tag{4.9}$$

where n is the porosity, d_{eff}^2 is some effective grain size, and s is a so called "shape factor", that accounts for the contributions of the other dependent variables (and is often determined through empirical means). The dependence of the permeability on the square of the grain size is often justified by considering the analogy between flow in porous media and Hagen-Poiseuille flow through a circular pipe[86,118] (porous media are often modelled as an ensemble of capillaries).

4.3.2 The Kozeny-Carman Equation

One of the more commonly used methods[86,110] for estimating permeability from the aforementioned parameters is the semi-empirical Kozeny-Carman equation:[86,118]

$$\kappa = \frac{1}{180} \frac{n^3}{(1-n)^2} d_m^2 \tag{4.10}$$

where d_m is some representative particle size. Some authors advocate using the mean particle size,[86] while others suggest a slightly more complicated method for calculating d_m by considering the particle size distribution (*e.g.*[97]).

Equation (4.10) has been validated over a wide range of permeabilities,[133] including the entire set of values that are used for the permeability parameter in the numerical model. For this reason, it has been selected as a convenient method for obtaining corresponding approximate grain size equivalents. The illustrations of equivalent grains sizes in this paper are calculated using (4.10), assuming that the grains are perfectly spherical and of identical sizes. The porosity is taken as 0.4, representative of randomly packed spheres.[140]

It is important to emphasize that real sediments are considerably more complicated, as they are composed of grains of various sizes and shapes. The grain size comparisons in Figures 4.5, 4.6(b), 4.7, 4.8, and 4.9 are intended for approximate context only.

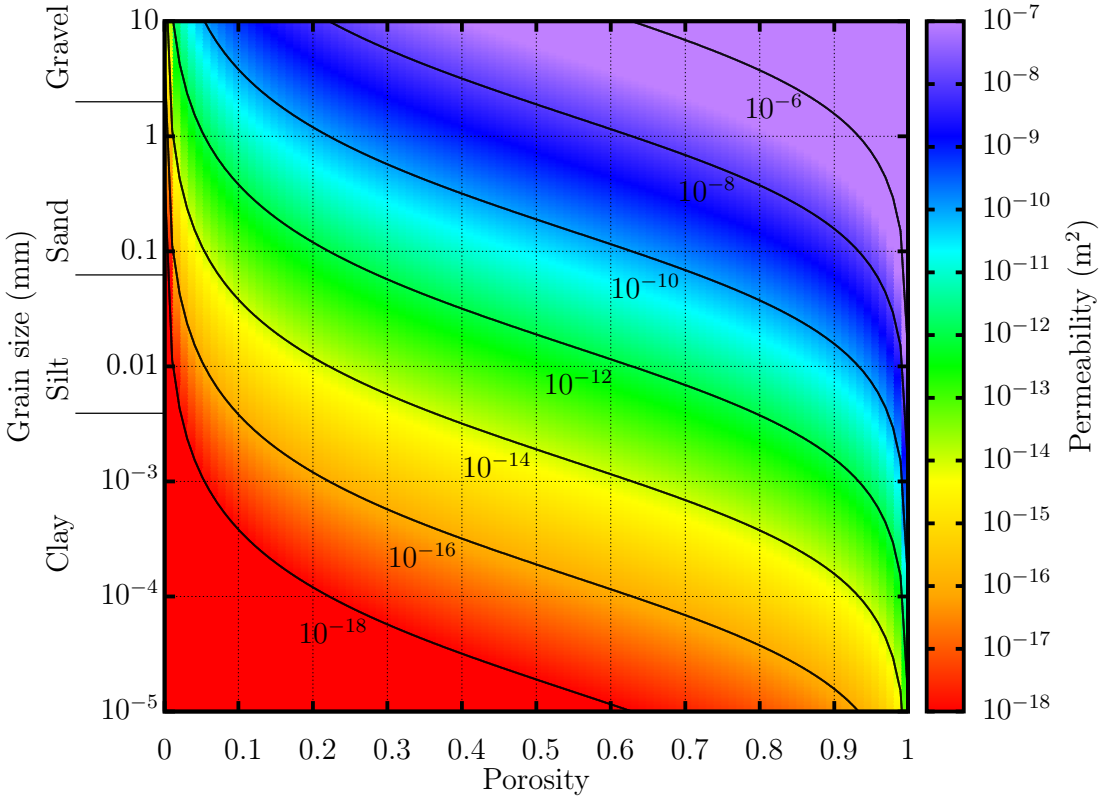

Fig. 4.3: Dependence of the permeability predicted by the Kozeny-Carman equation, (4.10) on grain size and porosity.

4.4 Results

4.4.1 Qualitative Overview

The permeability (κ), solid phase thermal conductivity (λ_s) and cable burial depth (b) were varied to establish the extent to which changes in these environmental parameters might affect the nature of the heat flow from the cable.

From the work that has been undertaken and investigations into the typical ranges for the dependent parameters (see table 4.2), it is clear that the permeability of the porous matrix is the most influential parameter in determining whether heat transfer from the cable is predominantly conductive or convective. The contribution to macroscopic thermal behaviour from the other relevant quantities is significant, but not nearly so critical as that of the permeability.

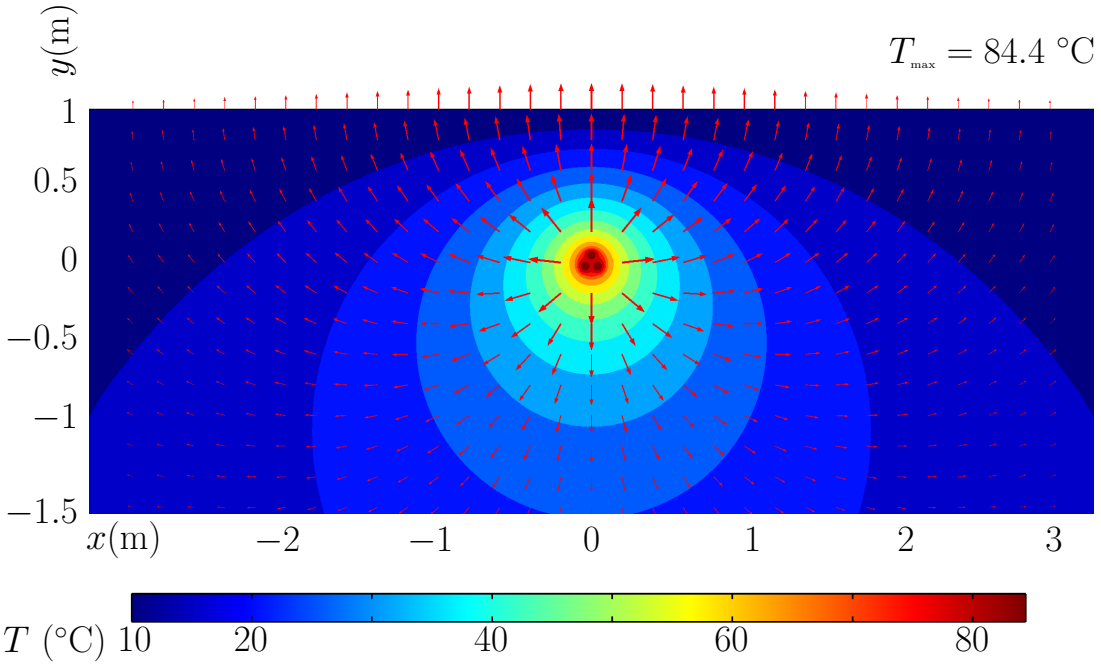

(a) Conductive: $\kappa = 1 \cdot 10^{-14}$ m^2 ($d \approx 3$ μm)

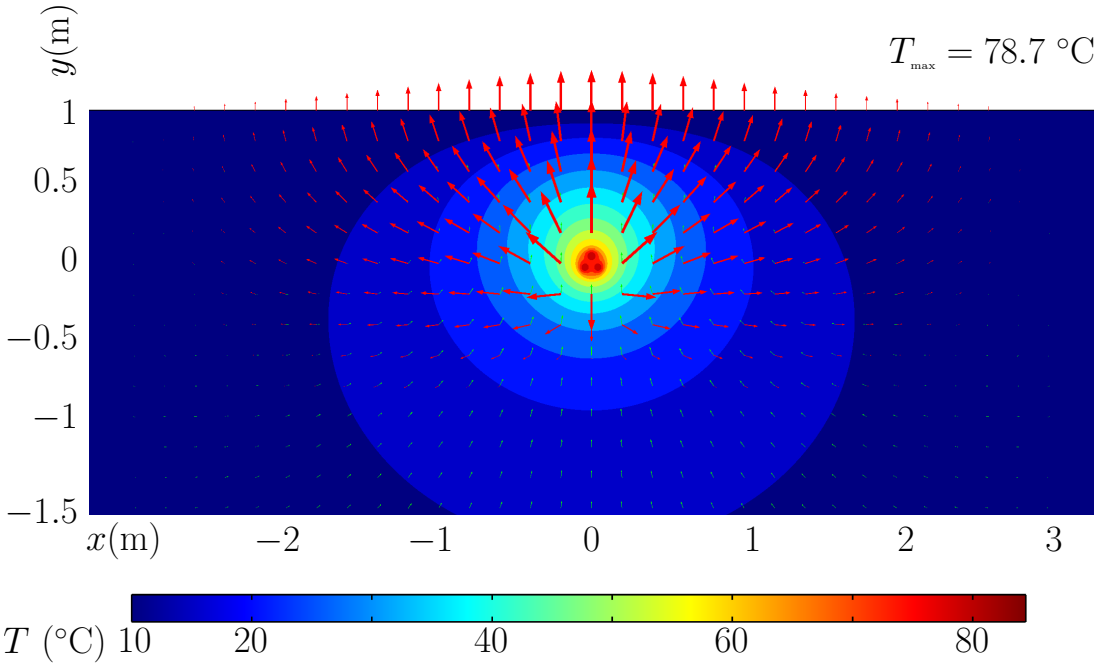

(b) Transition: $\kappa = 1 \cdot 10^{-11}$ m^2 ($d \approx 0.1$ mm)

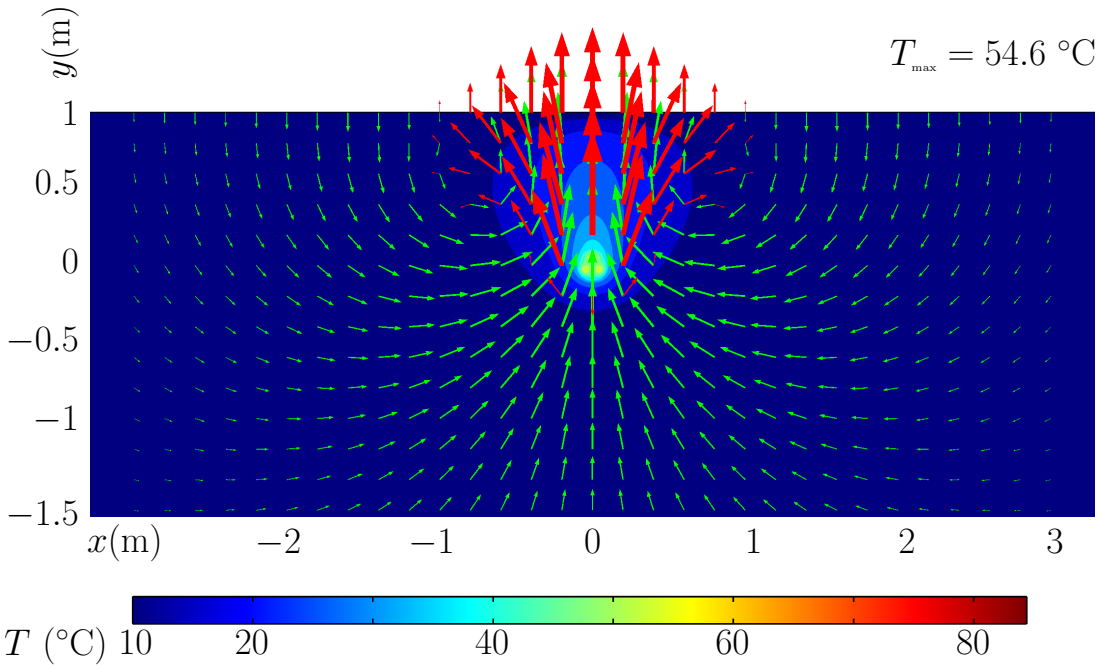

(c) Transition: $\kappa = 1 \cdot 10^{-10}$ m^2 ($d \approx 0.3$ mm)

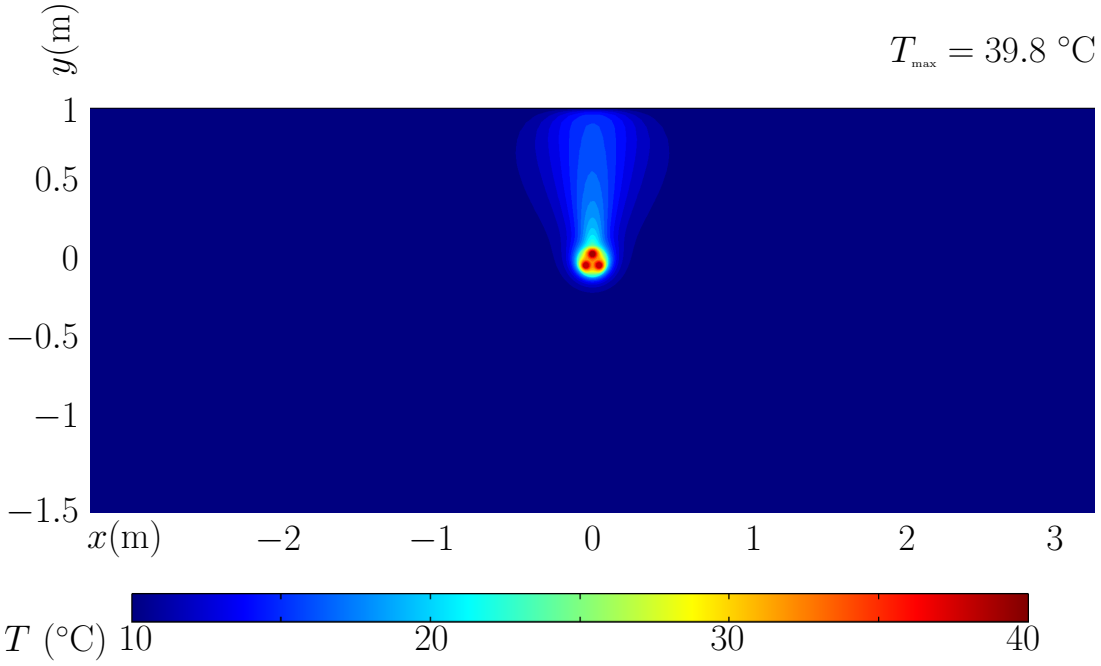

(d) Convective: $\kappa = 1 \cdot 10^{-9}$ m^2 ($d \approx 1$ mm)

Fig. 4.4: Example solutions for a low (4.4(a)) and high (4.4(c)) permeability sediment. The colour scale represents the temperature field; the red arrows illustrate the total heat flux away from the cable. The green arrows in Figure 4.4(c) represent the velocity field within the sediment. In both cases, the burial depth and the solid phase thermal conductivity are 1 m and 1 Wm^{-1}K^{-1} respectively.

At very low permeabilities ($\kappa < 10^{-14}$ m^2, $d < 3\mu$m), the fluid movement is restricted, and the heat transfer is dominated by conduction. The temperature field in this case is approximately isotropic (some degree of anisotropy is present due to the sea water acting as a heat sink above the top boundary). Figure 4.4(a) shows that the anisotropy is more pronounced at larger radial distances from the centre of the cable, with the temperature gradient being slightly steeper above the cable than below it.

At very high permeabilities, the reverse is true. Buoyancy forces drive fluid circulation. As a result, heat is transported largely in the upward direction; convection is the dominant mechanism by which heat is transferred away from the cable.

4.4.2 Varying Permeability and Thermal Conductivity

The dependence of the thermal behaviour of the system on permeability was investigated by solving the simulation numerous times using a parameter sweep over a range of permeabilities between 10^{-18} m^2 and 10^{-7} m^2. The intermediate values of κ solved for were selected such that there are five equally spaced values per power of ten on a $\log_{10}$ plot. As such, they can be calculated by using $\kappa_{i+1} = \kappa_i \cdot 10^{0.2}$. Of particular interest is the region in permeability space that characterises the transition from conduction to convection-dominated heat transfer. Qualitatively, the transition can be visualised as the continuous deformation of the temperature field from that shown in Figure 4.4(a) to the one in Figure 4.4(d) as the permeability is increased from 10^{-14} to 10^{-10} m^2 (or equivalently, as the grain size is increased from 3 to 300 μm) and beyond.

The transition to convective behaviour can be illustrated by plotting the maximum cable conductor temperature with varying permeability. As convective heat transfer becomes significant at around $\kappa = 10^{-11}$ m^2, there is a clear decline in this maximum temperature. In addition, the dependence of conductor temperature on the thermal conductivity is reduced. The cable surface temperature has a similar dependence on the permeability to that shown in Figure 4.5.

It is also possible to measure the conductive and convective fluxes within the simulation domain. An example boundary of length $4r$ (with r being the radius of the cable from central axis to the outer surface of the serving) was placed at a distance r above the top of the cable, (see Figure 4.6(a)) and the convective flux was measured across it for simulations with a variety of different permeabilities and thermal conductivities.

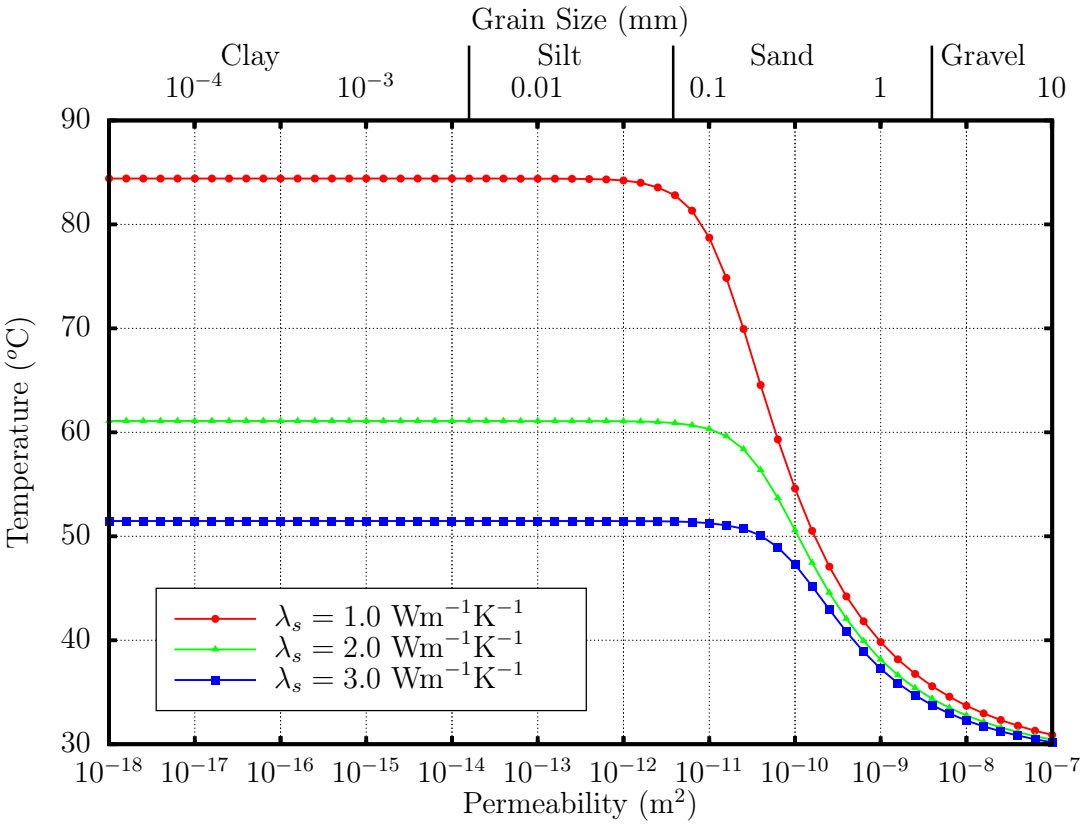

Fig. 4.5: Dependence of maximum conductor temperature with permeability for three different values of solid phase thermal conductivity. The cable burial depth in each case is 1 m. The second x-axis above the plot displays grain sizes (and traditional nomenclature) that approximately correspond to the permeability axis below, as calculated from (4.10) using $n = 0.4$. Equivalent thermal resistivities of the modelled sediments can be calculated by using (4.2).

For low permeability sediments (see Figure 4.6(b)), there is negligible convective heat transfer. Conversely, for very high permeability sediments, essentially all of the heat is transferred away from the cable by convection. It should also be noted that the initial onset of this convective behaviour itself appears to be dependent on the solid phase thermal conductivity of the sediment. Figure 4.7 shows that the permeability required for significant convection to take place is a function of the solid phase thermal conductivity of the sediment; for low solid phase thermal conductivities, significant convection can occur at a lower sediment permeability.

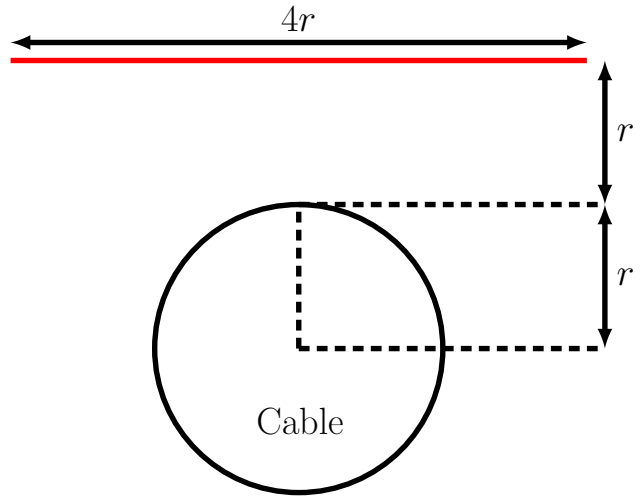

(a) The surface that the convective flux was measured across.

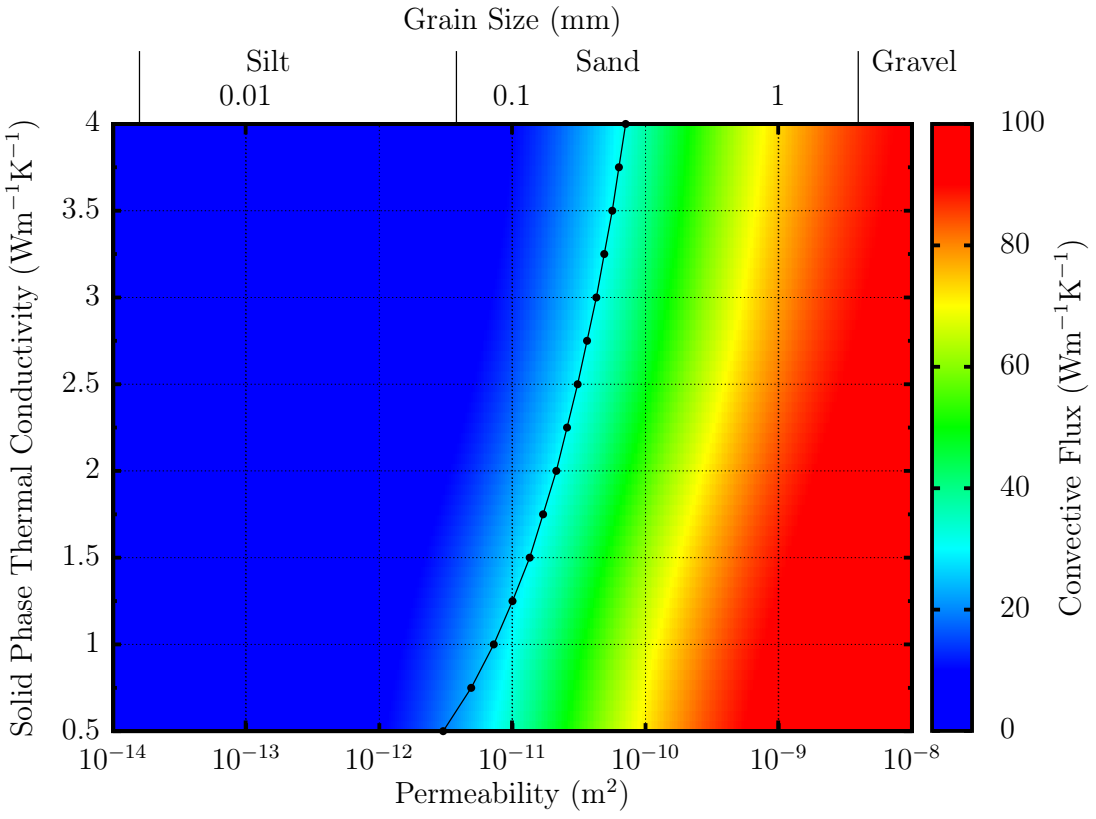

(b) Convective Flux

Fig. 4.6: Vertical convective flux measured at one cable radius above the cable for different permeabilities and thermal conductivities. The cable burial depth is 1 m.

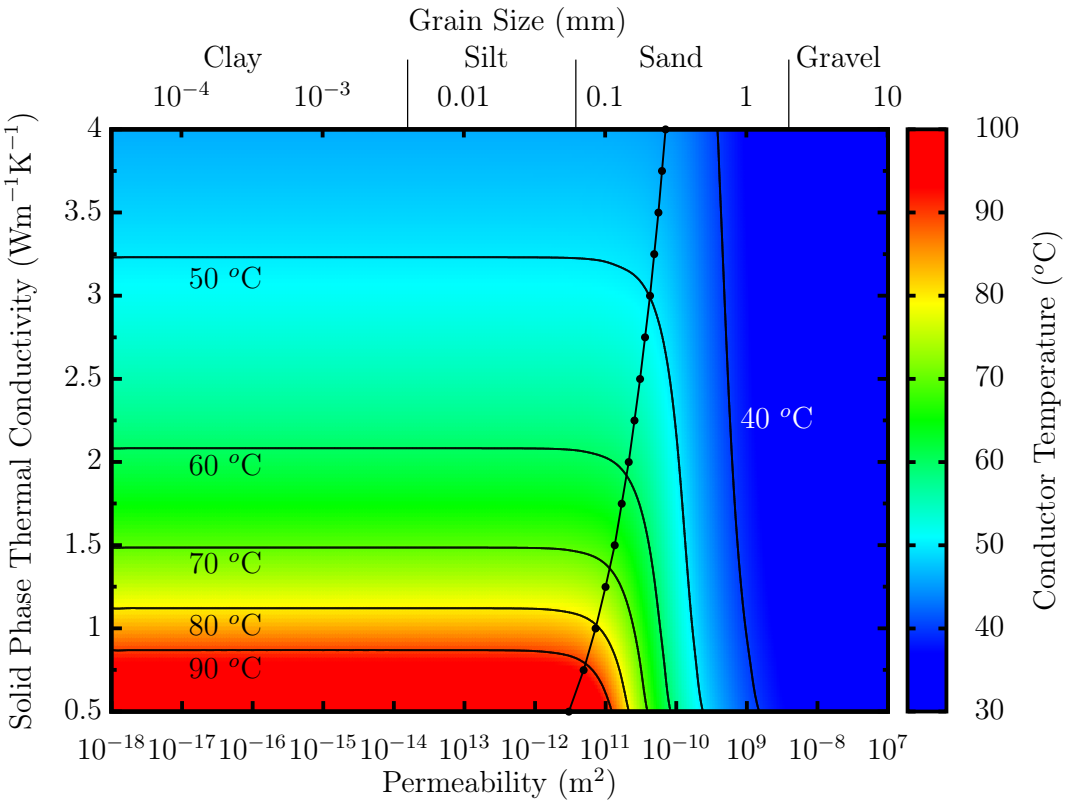

Fig. 4.7: Variation of maximum conductor temperature with permeability and solid phase thermal conductivity. The solid line with black dots shows parameters for which 20% of the heat transfer above the cable is convective.

4.4.3 Varying Burial Depth

In changing the cable burial depth, the distance from the cable surface to the overlying seawater heat sink is altered. This reduces the temperature gradient between the cable surface and the seabed-seawater interface. According to (4.1), this results in a reduction in efficiency of conductive heat transfer away from the cable. In the low permeability (i.e. negligible convection) limit, the maximum cable conductor temperature is increased for deeper burial depths. Figure 4.8 shows that as the permeability becomes more favourable to convective heat transfer, the conductor temperature becomes indifferent to the cable burial depth. This indicates that unlike conduction, the efficiency of convective heat transfer is not affected by the burial depth of the cable. As mentioned earlier, migration of sedimentary bedforms can produce a variation in burial depth of up to 5 m per year.

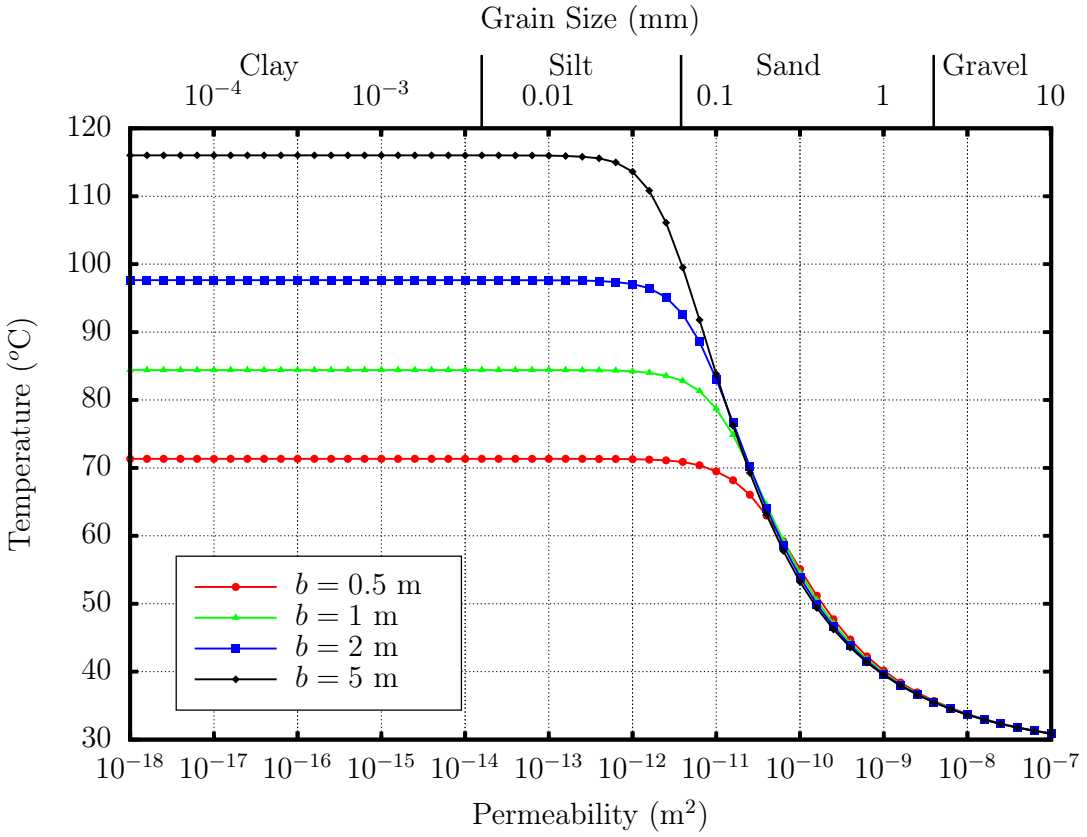

Fig. 4.8: Dependence of the conductor temperature on cable burial depth. In each case, the solid phase thermal conductivity is 1 $Wm^{-1}K^{-1}$.

4.4.4 Comparison to the IEC 60287 Standard

The temperature rise above ambient conditions predicted by the IEC 60287 standard for the cable design used in the model was compared to the value calculated by solving the finite element model for one low permeability (*i.e.* minimally convecting) burial sediment, and one with significant convection. It should be noted that the analytical approach assumes that heat transfer is only by conduction. Table 4.3 summarises the results of making the comparison for a variety of different thermal conductivities and burial depths of the sediment.

The agreement between the conductive modelled sediment (10^{-12} m^2) and the IEC 60287 standard in all cases is within 5%. One possible reason for this close agreement is that the convective heat transfer coefficient between the porous burial material and the overlying seawater will be a lot higher than the analogous coefficient between terrestrial soil and air.[71] Consequently, the physical seabed surface interface is better approximated by an isothermal condition (an assumption made in the IEC standard analytical approach) than a terrestrial cable. This is akin

λ_s	b	IEC T [°C]	κ_1 T [°C]	κ_2 T [°C]
1	0.5	69.2	71.3	55.1
2	0.5	51.5	53.5	49.3
3	0.5	44.2	46.1	44.7
1	1	82.5	84.2	54.5
2	1	59.2	61.1	50.6
3	1	49.7	51.5	47.3
1	2	95.7	97.1	53.9
2	2	66.9	68.7	50.4
3	2	55.1	56.9	47.9
1	5	113.0	113.6	53.2
2	5	77.0	79.3	49.8
3	5	62.2	64.4	47.7

Table 4.3: Predicted conductor temperatures for different thermal conductivities (λ, in $\mathrm{Wm^{-1}K^{-1}}$) and burial depths (b, in m) from the IEC standard and two modelled permeabilities: $\kappa_1 = 10^{-12}$ m^2 and $\kappa_2 = 10^{-10}$ m^2.

to situations on land where high wind speeds facilitate the transfer of heat from the soil to the air.[40] In this case, a higher wind speed results in a better correlation between numerical methods employing a convective condition, and analytical techniques assuming an isothermal boundary.

However, this concurrence only holds in situations where there is little or no heat transfer through the surrounding medium via convection (*c.f.* 10^{-10} m^2 column in Table 4.3). If this is not the case, then the model predicts a reduced conductor temperature (or alternatively, a higher cable rating), as heat can be transferred much more efficiently when both conduction and convection are at work.

4.5 Impact on Cable Design

The IEC 60287 standard analytical method for calculating cable current ratings assumes that all heat transfer through the sediment surrounding a cable is by conduction. However, the model suggests that convective processes can make a significant contribution to the dissipation of heat generated within these cables. This is supported by the results of an analogue experiment conducted in parallel with the modelling work discussed herein,[177] which clearly demonstrate that for thermal and sediment conditions representative of operational cables in the marine

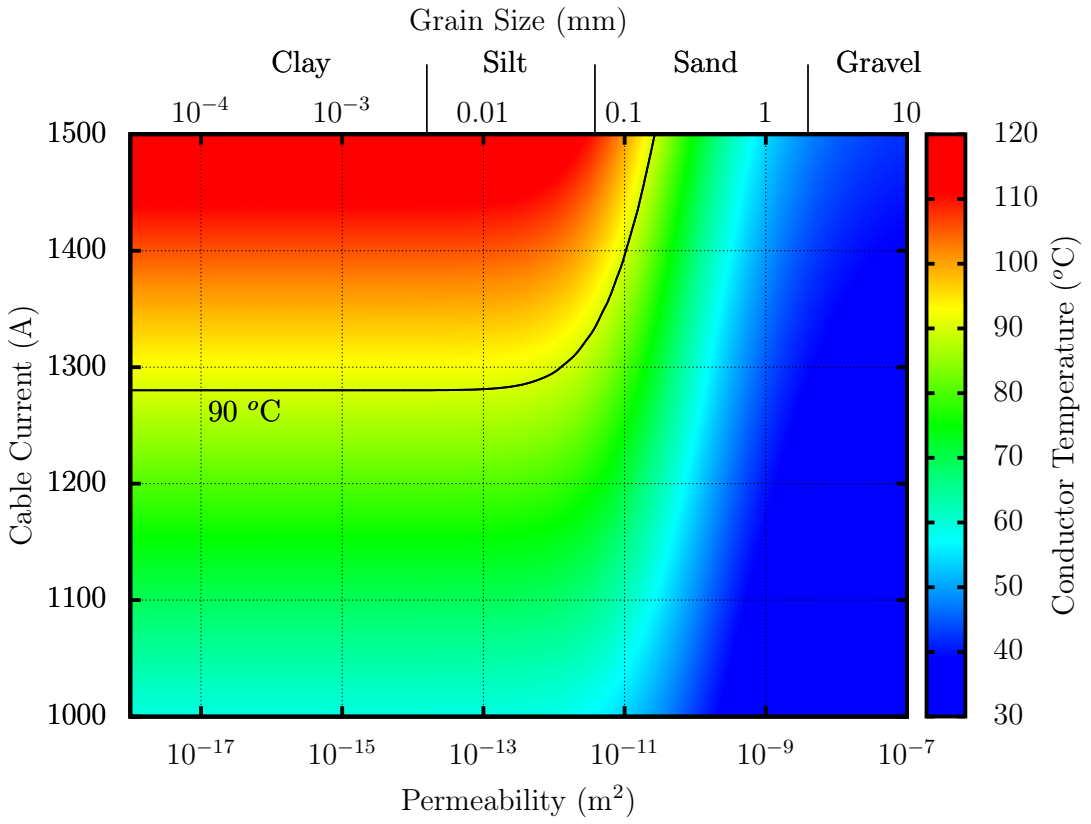

Fig. 4.9: Dependence of maximum conductor temperature on cable current load and permeability according to the FEM model. A burial depth of 1 m was assumed. The distribution of heat generation within the cable was calculated using IEC 60287.

environment, convective behaviour can occur. For cables that are buried in sediments that support convection, heat can be dissipated to the environment much more effectively than the IEC 60287 method suggests (see Table 4.3). Accurately determining the degree of convective cooling of the main cable lay could result in re-evaluating and increasing the overall transmission potential alongside artificial cooling of the short (10s metres) traditionally limiting sections, *e.g.* J-tubes, beach landing points. Regardless of whether the cable is the limiting factor or not, an augmented current rating would allow for a reduction in the amount of conductor material required for a cable to operate at a certain current.

It is also important to consider the dynamic nature of the seabed environment when assessing the thermal conditions of these assets. Migration of sedimentary bedforms, particularly in sands, may alter the burial depth of a cable by up to ~ 5 m with fluctuations occurring over time periods of less than a year. The impact of this change in depth on the cable conductor will particularly affect those in the transition between conductive and convective heat transfer corresponding

to fine sands (Figure 4.8). As seen in this figure and Table 4.3, this could cause temperature variations in excess of 30 °C for a single section of cable.

4.6 Conclusion

Finite element modelling of heat transfer away from buried submarine HV cables has been carried out, accounting for both conduction and convection. The cable temperature is controlled by a combination of the permeability, thermal conductivity and burial depth.

- Convection is likely to be the dominant mode of heat transfer away from submarine HV cables buried in medium sands ($0.25 - 0.5$ mm grains), or coarser sediments.
- The IEC 60287 standard only considers conductive heat transfer, potentially significantly under-rating submarine HV cables.
- Cable burial depth may vary on a relatively short timescale (months to years), leaving the cable exposed to a less favourable thermal environment.

In the marine environment, cables will encounter a range of different sediment types along their length. Understanding the associated variations in heat transfer is essential to accurately predict cable current ratings and for economical deployment of assets.

CHAPTER 5

Submarine HV Cables in Different Environmental Scenarios

5.1 Introduction

The simulations presented in the previous chapter describe the dissipation of heat from a submarine HV cable buried in a sediment that is completely spatially homogeneous in terms of its physical properties. Of particular interest was the conclusion that under certain circumstances (particularly when the sediment has a high permeability), convection can play much more of a role in the dissipation of heat than has been traditionally recognised for land buried cables.[178,179] While the results of the FEM simulations in Chapter 4 provide a valuable insight into how heat is dissipated from submarine HV cables in relatively simple burial scenarios, the applicability of the model to actual cables may be compromised by the assumption of sediment homogeneity.

Recall that previously, it was emphasised that marine environments are significantly more dynamic than typical terrestrial environments. For example, migrating bedforms (which can move across the bed at 10s of metres per year) result in relative increases and decreases in local bed level heights by several metres in the same time period.[31,180] Similarly, localised scour associated with seabed protruding infrastructure and natural outcrops can cause scouring to similar depths.[181] However, scouring can excavate sediment on shorter timescales, in some cases even down to hours.[60] The rate at which heat generated within the cable can be dissipated by conduction through the surrounding sediment is proportional to the cable burial depth (*i.e.* how far the cable is situated from the heat sink of the overlying seawater). Hence any rapid burial or excavation of sediment above a submarine HV cable will significantly alter the temperature of the cable for a given constant current flow.

It is possible, if not likely, that the dynamic nature of the seabed will also introduce heterogeneity into (or increase the extent of heterogeneity within) the sediment accommodating the cable. Whether or not the resulting inhomogeneities will have a sufficiently influential impact on the bulk properties of the burial medium to cause a significant departure in the thermal behaviour from the simple, homogeneous case (as detailed in Chapter 4) is hard to predict without a supplementary investigation. Several potential sources of inhomogeneities (to be described below) were identified by considering how the seabed (and its bulk properties) might be altered by common dynamic processes such as sediment deposition, and scouring.

The importance of each one was assessed by augmenting the FEM model developed in Chapter 4 into several different parallel models, each incorporating one of the different classes of inhomogeneity being investigated.

One of the main conclusions in Chapter 4 is that the permeability of the sediment can have a significant impact on the thermal environment to which a submarine HV cable is exposed, and hence on the resultant temperatures of the cable components. The various sources of inhomogeneity considered all either directly alter the permeability in a subregion of the sediment domain, or alter a property of the sediment on which permeability depends (*e.g.* porosity). It is therefore expected that alterations to the bulk sediment that increase the effective net permeability (and hence ease the flow of fluid through the medium) will increase the effectiveness with which heat can be dissipated to the surroundings (and vice versa). What is not known is the degree to which each source of inhomogeneity can alter the effective permeability of the bulk sediment, and whether the changes can be drastic enough to induce a substantial change in the way heat is dissipated from the cable.

Figure 5.1 depicts the configurations of the various scenarios examined in this chapter. An illustration of the homogeneous case is also provided in Figure 5.1(a),

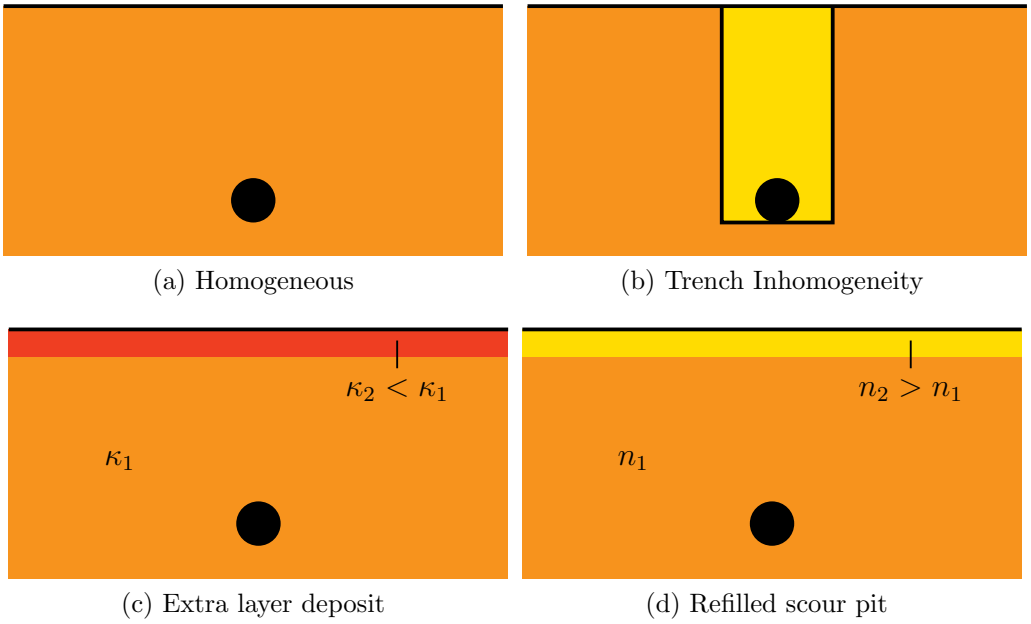

(a) Homogeneous (b) Trench Inhomogeneity

(c) Extra layer deposit (d) Refilled scour pit

Fig. 5.1: The environmental scenarios are illustrated here (not to scale). In each diagram, the cable is denoted by the black circle. Different sediment properties are denoted by different shades of colour; relative permeabilities (κ) and porosities (n) are indicated where discontinuities in these properties exists.

for clarity. Within each simulation, all of the environmental parameters that are not directly under scrutiny have been kept consistent with their values in the model developed in Chapter 4.

5.2 Homogeneous Sediment

In some cases, the properties of the sediment that backfills the trench dug to install the cable may return to their pre-installation values, rehomogenising the region proximal to the cable. If this happens, then a homogeneous sediment may indeed be a representative approximation of the actual cable situation. Recent CHIRP surveys around a European offshore wind farm site suggest that in some regions of the seabed, sediment backfilled into cable trenches can return to a state which is seismically indistinguishable from its surroundings.[182] This confirms findings from previous studies that have shown that some sediments (especially ones that are soft and unconsolidated[4]) can return to their pre-installation state almost immediately after the cable has been buried.[183] However, under different environmental circumstances, this may not be the case.

The thermal behaviour of submarine HV cables buried in homogeneous sediments has previously been studied using both numerical (see Chapter 4) and experimental (Emeana *et al.* 2016,[179] also see Appendix B) techniques. The reader is referred to these resources for a comprehensive discussion of a submarine HV cable buried in homogeneous sediment (in particular, Figure 4.4 qualitatively illustrates how the dissipation of heat from submarine HV cables differs according to the permeability of the sediment). For convenience, Figure 5.2 has been included to provide a basis for a qualitative comparison with the results of the other various FEM models developed to investigate the impact of different classes of sediment inhomogeneities on the nature of the heat dissipation from submarine HV cables.

5.3 Trench Inhomogeneity*

The first situation to be investigated that involves an inhomogeneous burial environment is one in which the sediment that backfills the trench containing the cable does not return to the ambient conditions after the installation procedure has been completed. There are a number of reasons why this might happen, for example:

- The environmental conditions during the period in which the trench is backfilled may differ from the ambient conditions during the original deposition of the background sediment. If this is the case, sediment in the trench region may be deposited in a slightly different way to the background material, imbuing it with different bulk properties.

- An extended period of time may be required to complete the backfilling of trenches dug into sediments that remain in suspension for a while after they are disturbed. Part of the material excavated during trenching may be transported away from the area by ocean currents. For example, assessments around the London Array offshore wind farm have found that fine sand disturbed during cable installation can be carried 1170 m in the 30 minutes it remains in suspension.[183] Silty material can remain in suspension for much longer (up to several days[183]), and is hence likely to be carried further by currents. A different sediment from a distant region of the seabed may be transferred to the trench to constitute a portion of the backfill.[183]

  Furthermore, in regions where bedrock or sediment with strong cohesion between grains is exposed at the seabed surface (it is common around the UK for clay to be exposed at the seabed surface), special techniques to trench into the rock are sometimes used.[4,180,184] In these cases, natural backfilling of the trench will not occur immediately.[4,183] Any backfill material (either from intervention during burial, or from gradual natural processes) is therefore likely to have significantly different bulk properties from the background medium.

- It is also intriguing to consider the potential benefits that might be gained by using an artificial backfill (provided it can be ensured that the backfill remains in place in the dynamic marine environment).

*This section has been inspired in part by the contents of the following conference paper: Hughes, T.J. *et al.*, "Thermal Ratings of Submarine HV Cables Informed by Environmental Considerations", in *Jicable'15 D9.6*, p.1-6, Versailles, France (21st-24th Jun 2015)

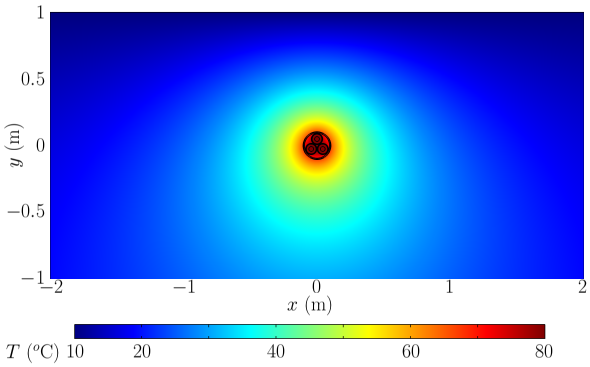

(a) Homogeneous: $\kappa = 10^{-13}$ m^2 ($d \approx 10$ μm)

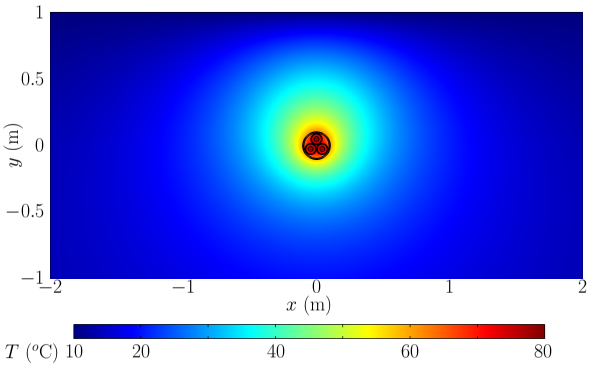

(b) Homogeneous: $\kappa = 10^{-11}$ m^2 ($d \approx 0.1$ mm)

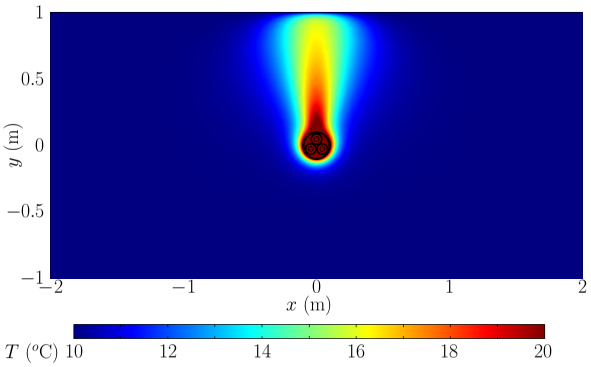

(c) Homogeneous: $\kappa = 10^{-9}$ m^2 ($d \approx 1$ mm)

Fig. 5.2: Temperature distributions for cables buried at a depth of 1 m in homogeneous sediments. The three permeabilities (increasing by a factor of 100 between each subfigure) illustrate the transition from conduction to convection dominated heat dissipation. The approximate grain sizes given are calculated using equation (3.54), with a porosity of 0.4.

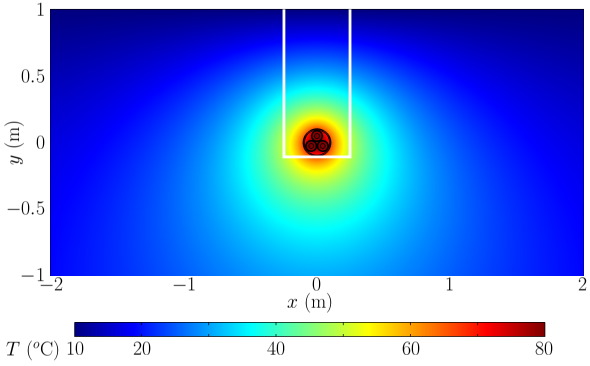

(a) Background permeability: $\kappa = 10^{-13}$ m^2 ($d \approx 10$ μm)

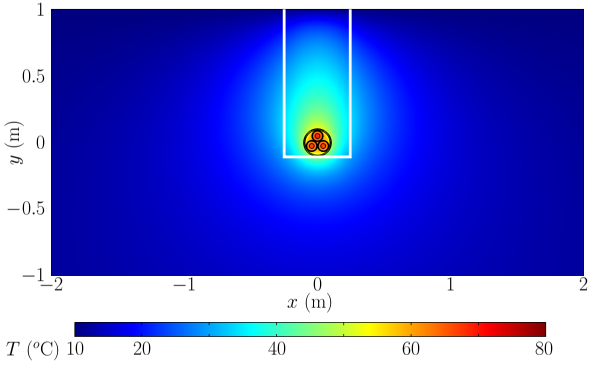

(b) Background permeability: $\kappa = 10^{-11}$ m^2 ($d \approx 0.1$ mm)

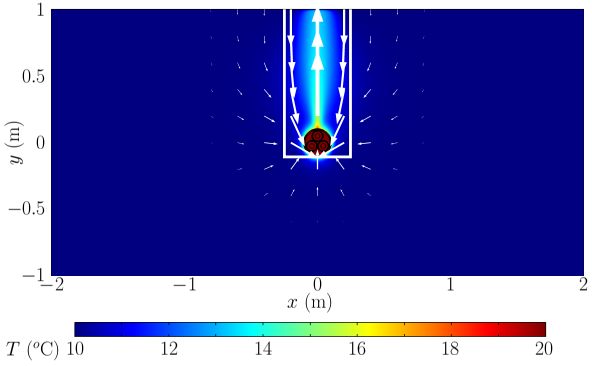

(c) Background permeability: $\kappa = 10^{-9}$ m^2 ($d \approx 1$ mm)

Fig. 5.3: Temperature distributions for cables buried at 1 m depth in sediments that include a trenched region with higher permeability. The permeability within each trench is a factor 10 higher than the outside. The white arrows in Figure 5.3(c) represent the fluid velocity field. The approximate grain sizes given are calculated using equation (3.54), with a porosity of 0.4.

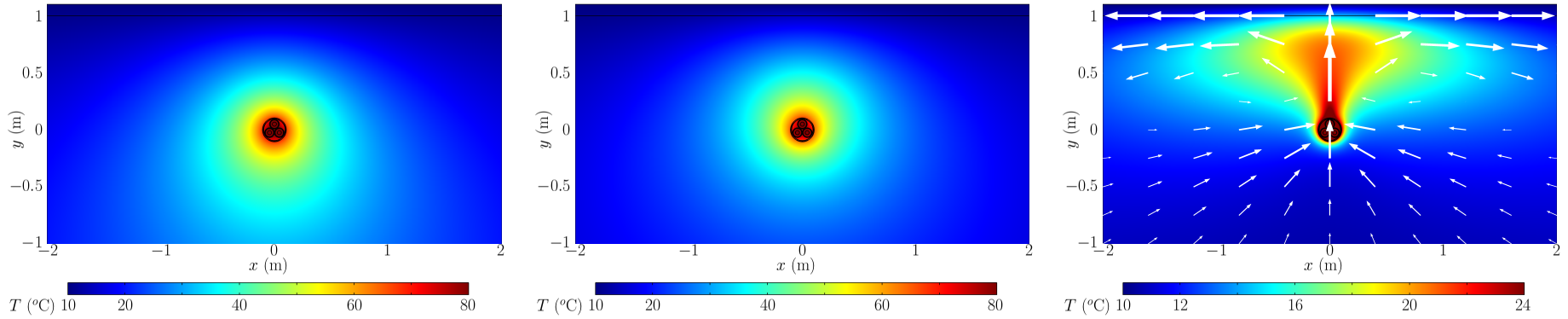

(a) $\kappa = 10^{-13}$ m^2 ($d \approx 10$ μm) (b) $\kappa = 10^{-11}$ m^2 ($d \approx 0.1$ mm) (c) $\kappa = 10^{-9}$ m^2 ($d \approx 1$ mm)

Fig. 5.4: Temperature distributions for cables in a sediment that includes a 10 cm thick low permeability deposit layer at the seabed surface. The white arrows in Figure 5.4(c) represent the fluid velocity field. The grain sizes use equation (3.54), with a porosity of 0.4.

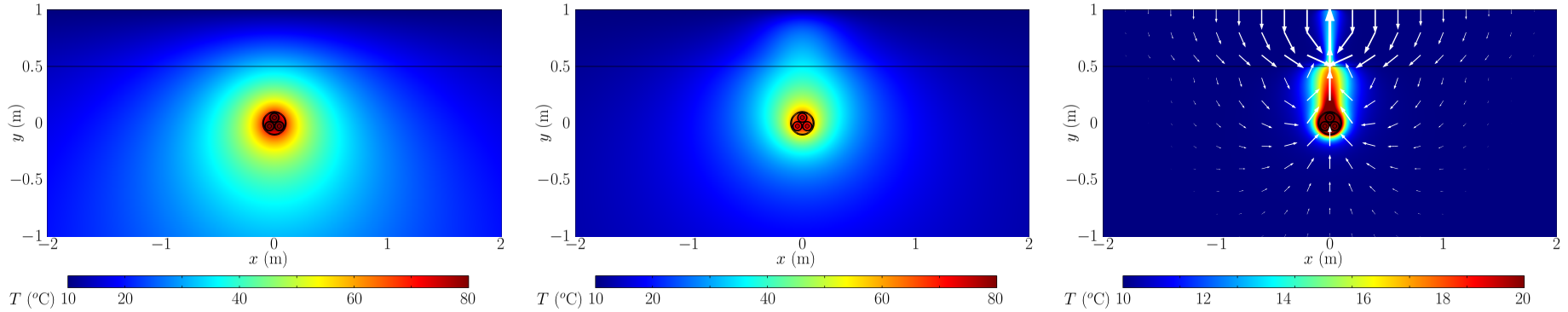

(a) $d = 0.0101$ mm: $n_{\text{top}} = 0.65 \Rightarrow \kappa_{\text{top}} \approx 1.27 \cdot 10^{-12}$ m^2

(b) $d = 0.101$ mm: $n_{\text{top}} = 0.65 \Rightarrow \kappa_{\text{top}} \approx 1.27 \cdot 10^{-10}$ m^2

(c) $d = 1.01$ mm: $n_{\text{top}} = 0.65 \Rightarrow \kappa_{\text{top}} \approx 1.27 \cdot 10^{-8}$ m^2

Fig. 5.5: Temperature distributions for cables buried underneath a 50 cm deep refilled scour pit for three different sediment grain sizes. For a porosity of 0.4, the grain sizes here give the same background permeabilities as those used in Figures 5.2, 5.3, and 5.4 so that permeability and grain size increase by factors of 100 and 10 respectively between adjacent subfigures. The porosity of the refilled sediment in each case is 0.65. The white arrows in Figure 5.5(c) represent the fluid velocity field.

A FEM model for this cable scenario was constructed from the one used in Chapter 4 by altering the geometry to include a trench region that allowed thermal and fluid exchange with the surrounding sediment, but had a different bulk permeability. The trench permeability was parameterised as a multiple of the background permeability (κ_r), ranging from 0.1 to 100. The width of the trench was also varied between 25 and 200 cm, while keeping the depth of the cable axis constant, at 1 m below the seabed surface. The permeability was altered in the trenched region in preference to any other parameters partly because of its dominance in determining the convective dissipative capacity (and hence, to a large extent, the total thermal dissipative capacity). Even though it may be hard to measure any variation in the permeability between real trench and background sediments directly, the permeability is also strongly dependent on factors like the grain size, porosity, and grain packing of a sediment. These are all quantities that might be expected to undergo changes during the trenching, and subsequent backfilling processes, and this approach combines their individual contributions into a single parameter to vary in the FEM model. Figure 5.3 shows the geometry of the altered FEM model, along with the results for three background sediments with different permeabilities that span the transition from conduction dominated to convection dominated heat dissipation. The examples in this figure describe a cable buried at a depth of 1 m in a 50 cm wide trench. The permeability of the sediment in this trench region is ten times that of the surrounding material, which is kept consistent with the material used in the homogeneous simulations displayed in Figure 5.2 (this corresponds to a difference in grain size of a factor of $\sqrt{10}$, according to equation (3.54)).

5.3.1 Results

The thermal implications of including a permeability contrast between the trenched region and the surrounding native sediment in the FEM model can be seen by comparing corresponding diagrams in Figures 5.2 and 5.3. At low permeabilities (*i.e.* when even the elevated trench permeability cannot sustain any convective heat transfer) there is no temperature difference. For example, the difference in maximum conductor temperature between Figures 5.2(a) and 5.3(a) is negligible*, as the trench sediment in Figure 5.3(a) has a permeability of 10^{-12} m^2 (which will convect only very slightly according to Figure 4.5). However, the dissipative

*around 0.01 °C according to a direct comparison between the results of the two models.

capacity of the environment will start to increase as soon as the (more permeable) sediment in the trench begins to support convective heat transfer. If the permeability of the material in the trench is high enough to support significant convection but the permeability of the background material is not, a convection cell is established within the trench. In this case, there is limited fluid exchange across the interface between the trench and the background sediment (for example, see Figure 5.3(b)). This convection aids in the cooling of the cable, causing the temperature of the cable conductors to be reduced.

As the discontinuity between the permeabilities of the background and trench sediments becomes more extreme, the effect on the thermal situation of the cable is amplified. This is illustrated clearly in Figure 5.6, where the difference in thermal behaviour from the homogeneous case ($\kappa_r = 1$) increases as κ_r gets (logarithmically) further from one. Consider an example case in which a submarine HV cable is installed into a 50 cm trench, and the permeability of the material in the trench is a factor of ten greater than the background sediment (as is the case in the examples shown in Figure 5.3). The FEM simulations predict a maximum 14 °C disparity in cable conductor temperature between this case, and the homogeneous sediment scenario (for an identical amount of heat generated within the cable). If the relative permeability of the trenched region is increased to 100 times that of the background, this figure becomes 28 °C. The largest differences occur at permeabilities that fall within the transition from predominantly conductive to predominantly convective thermal behaviour (at just over 10^{-11} m^2, or fine to medium sands depending on porosity - see Fig. 5.6). The implications for cable ratings of having a more effective dissipation of heat facilitated by having a more permeable sediment in the trenched region can be quite profound. For a 50 cm wide trench, a relative trench permeability of 100, and background permeabilities of 10^{-13}, 10^{-12}, $2 \cdot 10^{-12}$, and 10^{-11} m^2 respectively, the corresponding current ratings are: 1282, 1297, 1364, and 1916 A (*cf.* a homogeneous sediment in the conductive limit: 1279 A[185]).

In these 2D simulations, the width of the trench is also a significant factor in determining the extent to which the thermal conditions in and around the cable will differ from the homogeneous case. Assuming the discontinuity between the trench sediment and the background sediment remains sharp and independent of the trench width, narrower trenches have a smaller impact on the rate of heat dissipation than wider ones. This is consistent with the intuitive interpretation that with a larger trench, the situation is a closer approximation to one in which

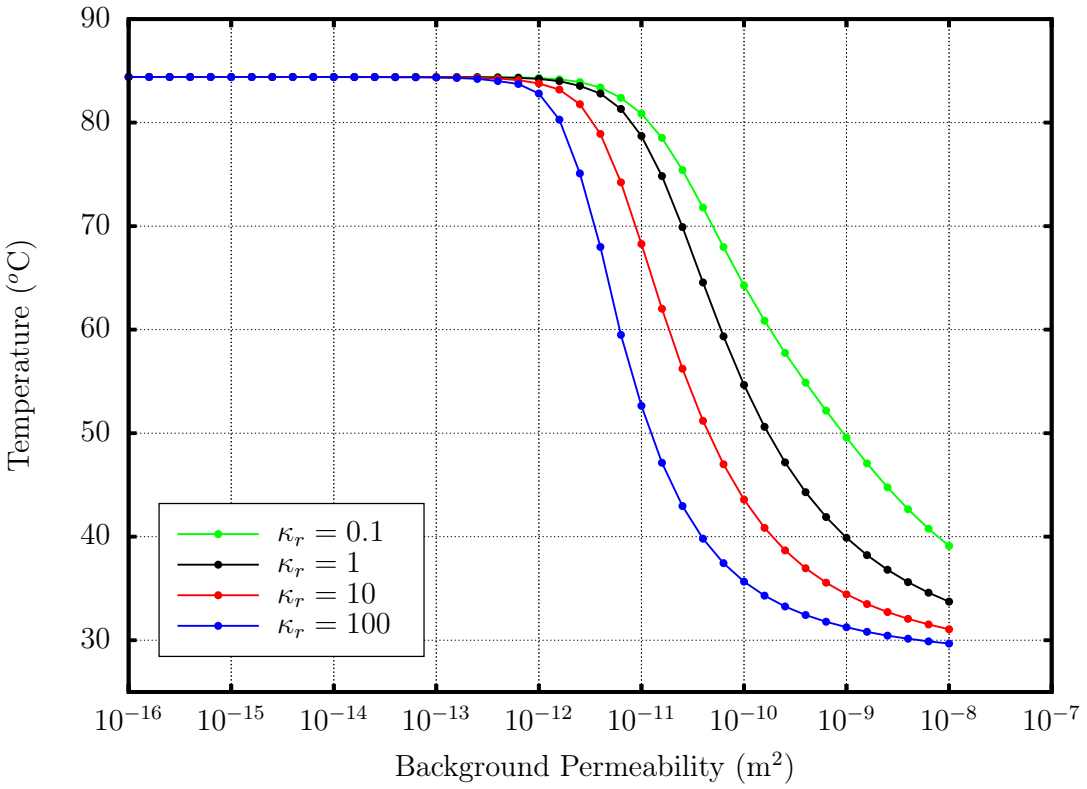

Fig. 5.6: A comparison of maximum cable conductor temperature for simulations that include higher permeabilities in the region of the trench initially dug to accommodate the cable. The trench width in each case is given by $w = 0.5$ m.

the cable is buried in a homogeneous sediment composed of material with a permeability equal to that of the trench material. A larger trench region containing a more permeable sediment will hence have a larger capacity for convective heat dissipation, which will in turn raise the total dissipative capacity (if the material in the trench is permeable enough to support convection). The rate of change in the cable temperature with respect to changes in trench width reduces as the trench width is increased. This is not surprising, as changes to the sediment bulk properties have the greatest effect nearest to the cable, where the highest temperature gradients in the sediment domain are likely to be found. The graphs presented in Figures 5.7(a) and 5.7(b) illustrate the effect of varying the width of the trench region surrounding the cable. The relative permeability between the trench and background sediments in these figures is kept at a constant value of $\kappa_r = 10$ and $\kappa_r = 100$ respectively. Unfortunately, for a permeability contrast of $\kappa_r = 100$ and a trench width of 25 cm, the FEM model was only stable for background sediment permeabilities of up to just over 10^{-10} m^2 (note that the permeability of the sediment in the trench is 100 times greater than this, which may contribute to the instability) however, it is still interesting to observe the thermal behaviour during

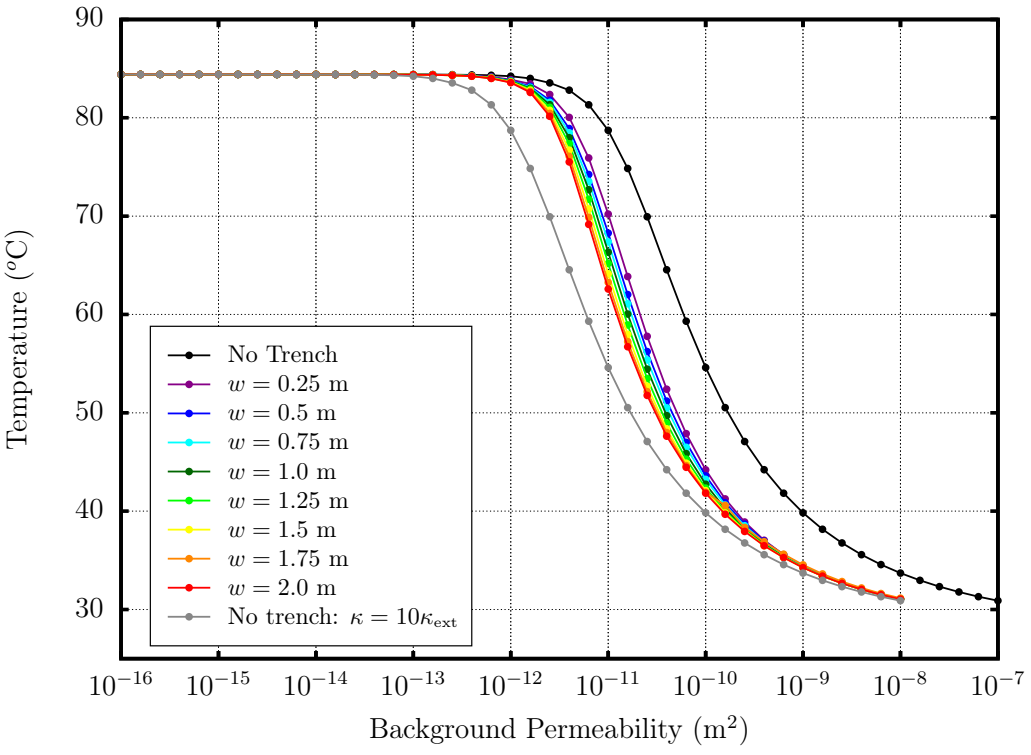

(a) $\kappa_r = 10$

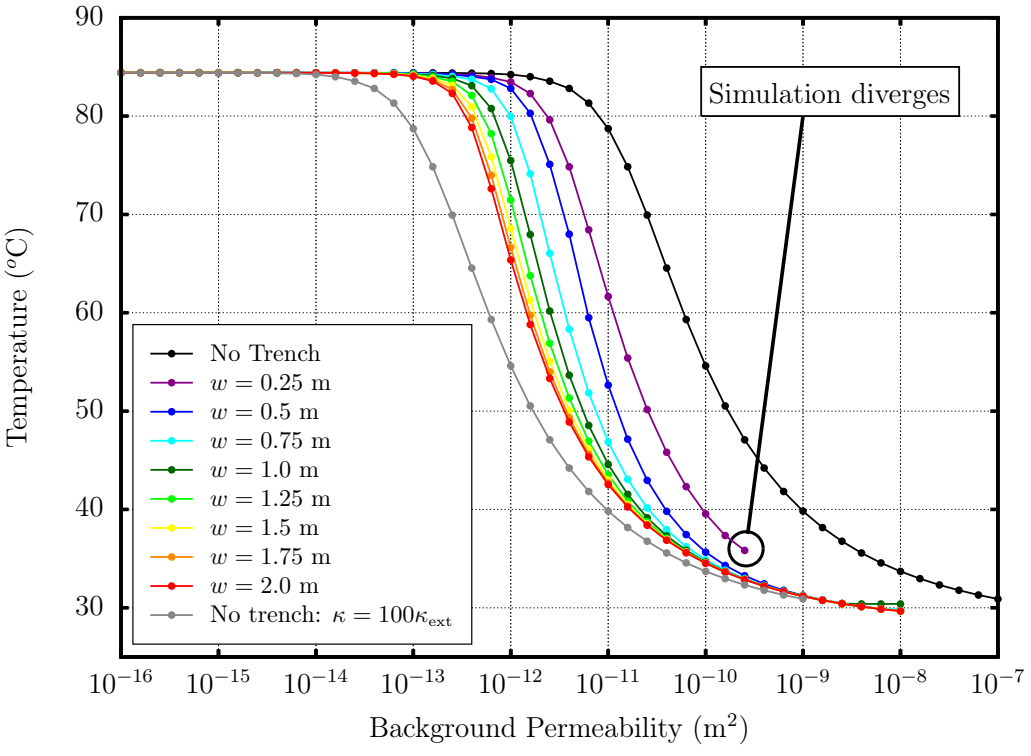

(b) $\kappa_r = 100$

Fig. 5.7: Two Illustrations of how the maximum cable conductor temperature varies with the width of the trench, for a permeability contrast of (a) 10 and (b) 100 between the trench and the background sediments. The x axis here denotes the permeability of the background material.

the beginning of the transition to convective thermal behaviour*.

The 2D simulations presented here consider heat and fluid flow only in directions perpendicular to the axis of the cable. However, there may be situations where a non-negligible amount of fluid is transferred parallel to the cable axis. Consider the example of a submarine HV cable installed into a sediment that initially has a low permeability (low enough that there is no fluid motion within the medium), before being perturbed by the cable installation process. If the permeability of the material in the trench is increased to a point where it can support convective heat dissipation, fluid flow within the sediment will be restricted to the disturbed material in this region only. As heated fluid is advected upwards through the trench and into the overlying seawater, recharging fluid will be forced to enter the sediment at the interface between the trench and the seawater (as it is prevented from permeating into the trench region from the background sediment). Localised fluctuations in temperature along the cable may result in heated fluid being more vigorously advected upwards above hotter regions of the cable. This in turn would force the cold recharge fluid from the overlying seawater to enter the trench above cooler spots, before being drawn along the cable to the warmer spots to continue the cycle of convection. In this way, variations in temperature may develop over length scales similar to the cable burial depth. While interesting to consider, exploring the potential for such behaviour is beyond the scope of this thesis.

The extent to which the cable is cooled with the inclusion of a trench with a different permeability to the background sediment depends on a number of factors. The greatest difference in the results between these simulations, and those modelling a homogeneous sediment occurs when: there is a large permeability contrast between the trench and background materials, when these permeabilities fall on either side of the transition between conduction dominated and convection dominated heat transfer, and when the trench width is maximised. To promote the conduction of heat away from cables on land, a material with a high thermal conductivity is often used to backfill the cable trench, rather than using the original excavated sediment. A similar approach could be employed for submarine HV cables, by using a high permeability sediment to backfill trenches dug into thermally resistive, impermeable sediments that stunt both conductive and convective dissipation. The feasibility of using a highly permeable artificial backfill material will be impacted by the more dynamic nature of the seabed environment. For it to be economical, there must be a long lasting benefit for the cable. It must

*The design for the cable used in the FEM model (as described in Table 4.1) has a diameter of around 21 cm, so a significantly narrower trench would not be possible anyway.

therefore be ensured that the trench region remains highly permeable for a long period of time. This will be jeopardised if the backfill material is eroded from the trench and transported away by currents in the seawater, or if less permeable sediment infiltrates the trench region and reduces its bulk permeability. The flow velocities required to erode, transport, and deposit sediment of a given grain size is illustrated in Figure 5.8. The formerly described process may be mitigated by the fact that larger, heavier grains are harder to transport suspended in seawater than finer, lighter ones. Hence, if the background sediment is static, the backfill will be as well. The process may still be necessary to consider in cases where a coarse material is used to backfill a trench dug into relatively immobile clay or bedrock, and the local currents are strong enough to shift the backfill material.

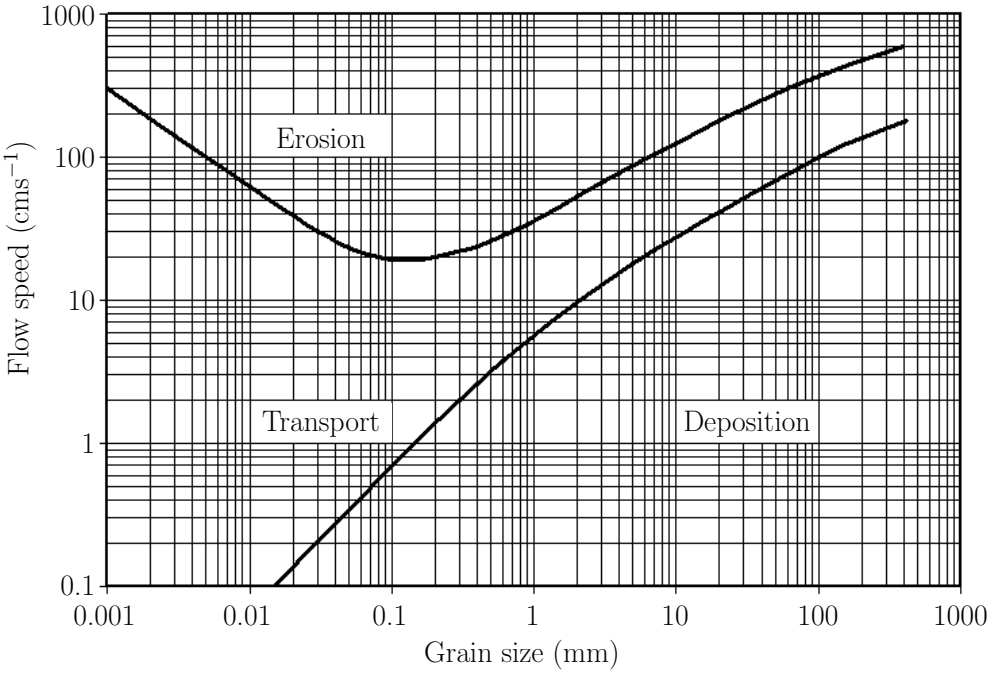

Fig. 5.8: Hjulström curve illustrating the flow velocities for which sediment grains will be eroded, transported, and deposited. This image is licensed under CC BY-SA 3.0, and has been modified from the original (accessed: 2016-07-23 ∼14:20 UTC+1) provided by wikipedia user Karrock, under the same licence.

5.4 Capping Silt Deposit Layer

The second type of inhomogeneity to be investigated describes situations where a finer sediment is deposited on top of the initial burial sediment over time. This may occur either during the trenching process (finer grains remain in suspension

for longer than coarse grains, and will take longer to resettle onto the seabed), or through the deposition of sediment transported to the area by seawater currents. Due to the dynamic nature of the marine environment, transport of sediment can take place over short timescales. The presence of a finer capping sediment on coarser material can be particularly common in inter-tidal, and immediate sub-tidal zones where reduced flow velocities associated with high water can deposit finer sediments in the near surface.[186] The situation may also be relevant if (in a hypothetical case) a highly permeable material was used to artificially backfill a trench upon completion of the cable installation, and the area was then subject to deposition of additional background (or some other finer) material at the seawater interface.

In addition to being a function of porosity, recall that the permeability of a sediment is also strongly dependent on its characteristic grain size.[86] Hence, the accumulation of a fine grained material on the seabed surface will produce a layer of low permeability in the region of deposition. The amount of heat that can be dissipated across this layer will be smaller relative to the more convective background sediment.

To simulate this situation, the model developed in Chapter 4 was again altered to include a 10 cm thick layer of low permeability material which was added to the top of the simulation domain (such that the distance from the cable axis to seabed surface was then 1.1 m). The permeability of this layer was selected to guarantee that there would be no fluid flow (and hence no advection of heated seawater) through it. The amount of heat dissipated by convection is dependent on other environmental parameters, such as the sediment thermal conductivity, and cable burial depth (see Figures 4.5, 4.6(b), and 4.8). For a cable buried at a depth of 1 m in a sediment with a solid phase thermal conductivity of 1 $\mathrm{Wm^{-1}K^{-1}}$, the "no fluid flow" condition applied to the top layer of sediment is applicable for permeabilities less than $\sim 10^{-12}$ $\mathrm{m^2}$ (see Figure 4.5). Using the Kozeny-Carman formula, equation (3.54), this corresponds to grain sizes less than ~ 0.03 mm (silt). For more thermally conductive sediments or deeper burial depths, this condition holds for larger grain sizes. The effect of this type of burial situation on the temperature of the cable will be most extreme under the circumstances described above, where the deposit is completely impermeable to seawater. However, the deposition of any sediment that has a lower permeability than the background material will have a similar, but milder effect if it impedes the path of heated fluid being advected towards the overlying seawater.

5.4.1 Results

Figure 5.4 shows some temperature distributions for the same background sediment permeabilities used in Figures 5.2 and 5.3. The presence of an overlying low permeability deposit resulted in an increase in the temperature of the cable for all sediment permeabilities. In the conductive limit, the increase in temperature can be attributed to the additional distance between the cable and the seabed surface, (which has been increased by the depth of the overlying deposit). This amounts to an alteration of the temperature gradient term in equation (3.14). The increase in temperature from the homogeneous case is maintained as convection begins to make a contribution to the dissipation of heat (see Figure 5.9).

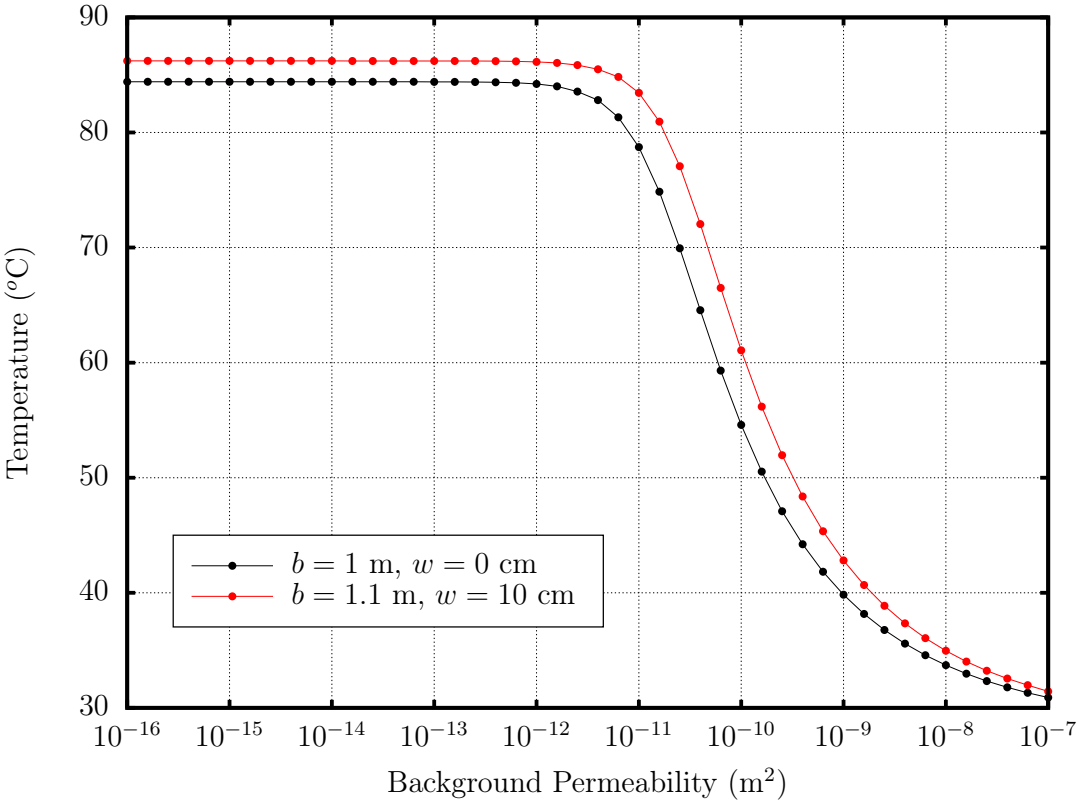

Fig. 5.9: A comparison of maximum cable conductor temperatures for scenarios that include a low permeability layer deposited at the seabed surface. The total distance between the cable axis and the seabed surface is given by the parameter b, which is equal to one metre plus the depth of the deposited sediment (10 cm in this case).

Again, the greatest variation in cable temperature due to this type of inhomogeneity (7.5 °C) occurs when the permeability of the native sediment is in the transition zone between conductive and convective behaviour.

The morphology of the temperature distribution shown in Figure 5.4(c) is unlike any of those illustrated previously in this chapter, or in Chapter 4. In this case, as expected from the previous results, convection plays an important role in dissipating the heat generated within the cable. However, the heated pore fluid is prevented from reaching the cool overlying seawater by the "ceiling" of the impermeable deposit layer. A large thermal gradient is established across the layer, as it is heated from below by the fluid, and cooled from above by the seawater. The flux of heat conducted across the impermeable layer is determined by its thermal conductivity, and the magnitude of the temperature gradient across it. A larger surface area contact between the heated fluid and the impermeable layer is required to dissipate all of the heat arriving from below to maintain a steady state.

5.5 Refilled Scour Pit

The dynamic nature of the seabed can result in the removal of sediment around buried submarine HV cables through the process of scouring. Marine sands are generally much more susceptible to the process of scouring than sediments composed of either finer or coarser material.[181] Finer, more consolidated sediment (*e.g.* clay) is able to resist erosion more effectively than loose, sandy material. Any scouring of cohesive sediments will occur at a much slower rate, and will be much more limited in extent than in unconsolidated material.[181] Coarse sediment (such as gravel) requires a higher water flow rate than sand to become mobile, and hence will also be more resistive to scouring than lighter sandy material (see Figure 5.8). Therefore, scouring is most likely to become an issue for submarine HV cables when they are buried in sands (that have a characteristic grain size in the range: 62.5 μm $\lesssim d \lesssim$ 2 mm), rather than gravels or clays.

Post-installation surveys around the Arklow Bank offshore wind farm (located in the Irish Sea) have revealed that in some places, the export cable has become directly exposed to the seawater.[183] A similar effect has been observed at the Scroby Sands offshore wind farm (North Sea), where scouring around the base of offshore structures has led to the exposure of inter-array cables.[183] Unconsolidated sands make up the superficial sediment at the seabed surface in both of these regions.

Data acquired recently from the aforementioned surveys of a European offshore wind farm revealed that the scour pits established around HV cables at the site

were often periodically (at least partially) refilled.[182] The wind farm export cables will be correspondingly subject to changes in the burial conditions around these volatile locations. Often, a disturbance of the seabed sediment (for example, from scouring and subsequent refilling of the pit) will result in a higher porosity than the initial seabed material.[187] Such a change in the porosity of the overlying material will alter its permeability,[86] and its bulk thermal conductivity.[91] Another aspect of scour pits relevant to the thermal environment surrounding submarine HV cables is the intermediate steps in the process of scouring and subsequent refilling. The burial depth is an important parameter in determining the temperatures of cables buried on land. Sediment scouring above the cable may leave it much more shallowly buried, or even exposed to or spanning gaps on the seabed surface.[183]

Two sets of FEM models were constructed to investigate cases where a scour pit of depth s cm had been completely refilled (such that there was no net change in the cable burial depth), and cases considering intermediate steps in the scouring/refilling process respectively. The latter intermediate stage models were constructed in a similar manner to the homogeneous case, with the burial depth of the cable altered to several different values.

Unlike the FEM simulations described in the sections above and in Chapter 4 which were all run in permeability space, the simulations for the refilled scour scenarios were conducted in grain size space. The reason for this was that the environmental parameter that is primarily being varied in this case is the porosity. Note that not only is the convective term in equation (3.14) directly dependent on the porosity, but several other terms in the equation are too. Changes in porosity will also affect the sediment thermal conductivity and permeability (see Chapter 3). The porosity therefore has a slightly more complicated effect on the nature of the flow of heat in and around the cable, as both the conductive and convective terms in equation (3.14) will be further altered by changes in the sediment permeability and thermal conductivity respectively due to their dependence on porosity. The bulk thermal conductivity will usually be decreased by increasing porosity (the individual conductivity of the permeating fluid is usually lower than that of the sediment grains), while the permeability will increase with increasing porosity. The bulk thermal conductivities used in the FEM model were calculated in the usual way, but using different values for the porosity in the appropriate domains. The permeabilities used in the model were estimated by substituting the relevant porosities for each region into equation (3.54), the Kozeny-Carman equation.

Figure 5.10 shows how the temperature of a cable conductor might vary with porosity and grain size using a permeability calculated according to the Kozeny-Carman equation. Interestingly, sandy sediments lie on/near the transition from conductive to convective thermal behaviour. Conductor temperatures will therefore be influenced more by altering the porosity of the burial medium for cables in sandy sediments (while keeping the grain size exactly the same) than for cables buried in other types of sediment. The porosity appears to have a weak effect on the cable temperature even when the grain size (which is strongly correlated with permeability) is relatively large (> 1 mm). This is an artifact of the dependence of the permeability on the porosity, as it has previously been stated that the permeability has a strong effect on thermal behaviour, especially when it is large.

For the simulations with no net change in burial depth, porosities of 0.4 and 0.65 were used for the regions of background sediment and refilled scour pit respectively. The porosity contrast between the two sediment types was purposefully selected to be this large to establish whether or not this change in the burial conditions could

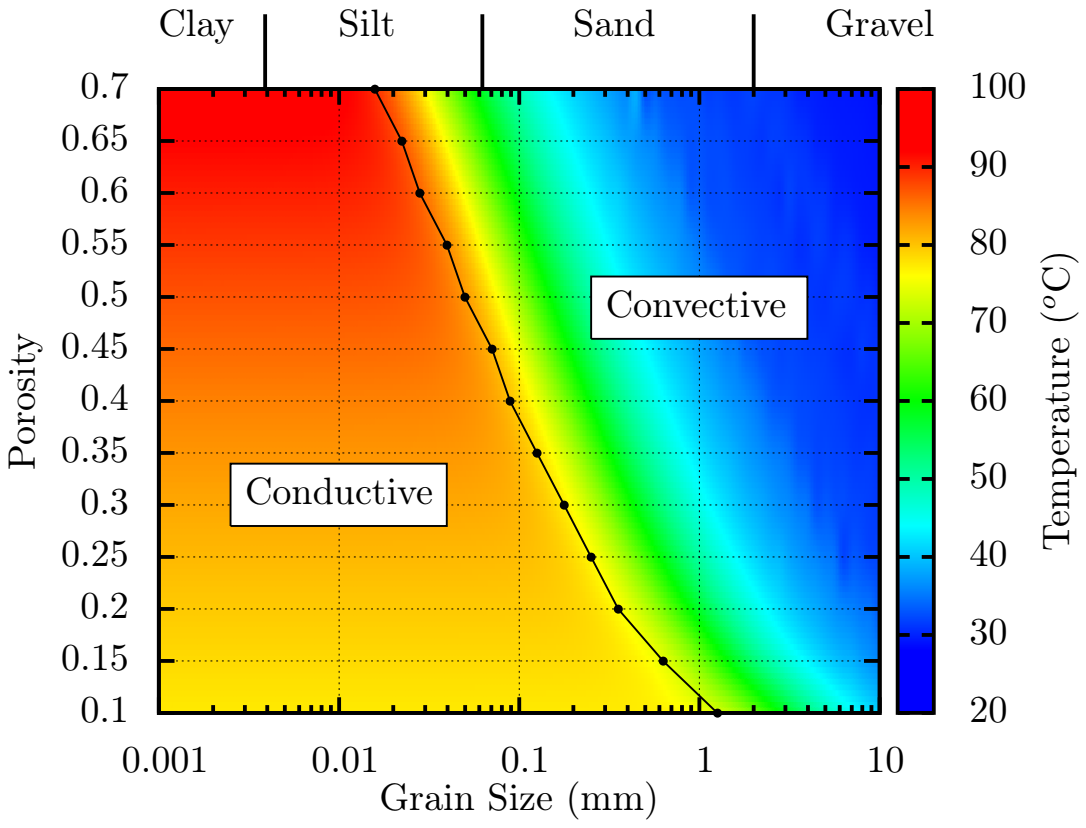

Fig. 5.10: The dependence of the cable conductor temperature on the sediment porosity and grain size is shown. The dotted black line distinguishes between greater than and less than 20% convective heat transfer.

have an appreciable effect on cable temperatures under favourable conditions, before addressing whether it may be likely (or not) in more realistic scenarios.

5.5.1 Results

For sandy sediments that have a high permeability and are capable of supporting convective heat dissipation (and are more likely to undergo scouring), cable temperatures will be lower than the homogeneous case. Heat transfer through the refilled material is more efficient, as a higher level of convection can be sustained in this region. Conversely, for cables buried into silts and clays (characterised by grain sizes smaller than sands, and low permeabilities) that dissipate heat solely by conduction, any scouring and subsequent refilling of the scour pit is liable to increase the predicted cable conductor temperature. This occurs because the thermal conductivity of the sediment grains is greater than that of the pore fluid. For larger proportions of fluid, the effectiveness of conduction through the bulk medium is reduced. Figure 5.5 shows the qualitative change in thermal behaviour as the permeability of the background sediment is increased.

The cable in Figure 5.5(c) is initially buried in a coarse sand that supports some convection. However, some heat is still conducted to the grains of the sand from the heated water as it is advected upwards towards the base of the refilled scour pit. The more porous sand in the refilled scour pit is more permeable than the sediment beneath it. There is less conduction of heat from the advecting plume of water to the sediment in this region, hence the narrower isotherms in the refilled scour pit.

Figures 5.5(b) and 5.5(c) depict cables buried in a very fine sand (with a limited capacity for convective dissipation), and a very coarse sand (highly convective) respectively. The temperature distributions around the cables differ somewhat in appearance from the corresponding homogeneous cases in Figures 5.3(b) and 5.3(c). Despite this, however, the presence of a refilled scour pit with increased porosity has a muted effect on the cable conductor temperature unless the refilled pit is quite deep (*cf.* the depth of the cable). For example, a refilled pit with a depth of 40 cm will induce, at most, a change in temperature of 2.1 °C from the homogeneous case. For a 70 cm deep pit, the maximum temperature difference is 6.5 °C (see Figure 5.11). The greatest differences occur for fine sands (that are more susceptible to scouring than other sediment types), during the transition from conductive to convective behaviour.

Sediments with low permeabilities saw the strongest contrast in results from the simulations with varying burial depths. In the low permeability limit, the maximum conductor temperatures for a cable buried at a depth of 75, 50, and 25 cm differed from the 1m burial depth case by 5.4, 13, and 26 °C respectively. This drastic effect is diminished at higher permeabilities, as the significance of conductive heat transfer is reduced (see Fig. 5.12).

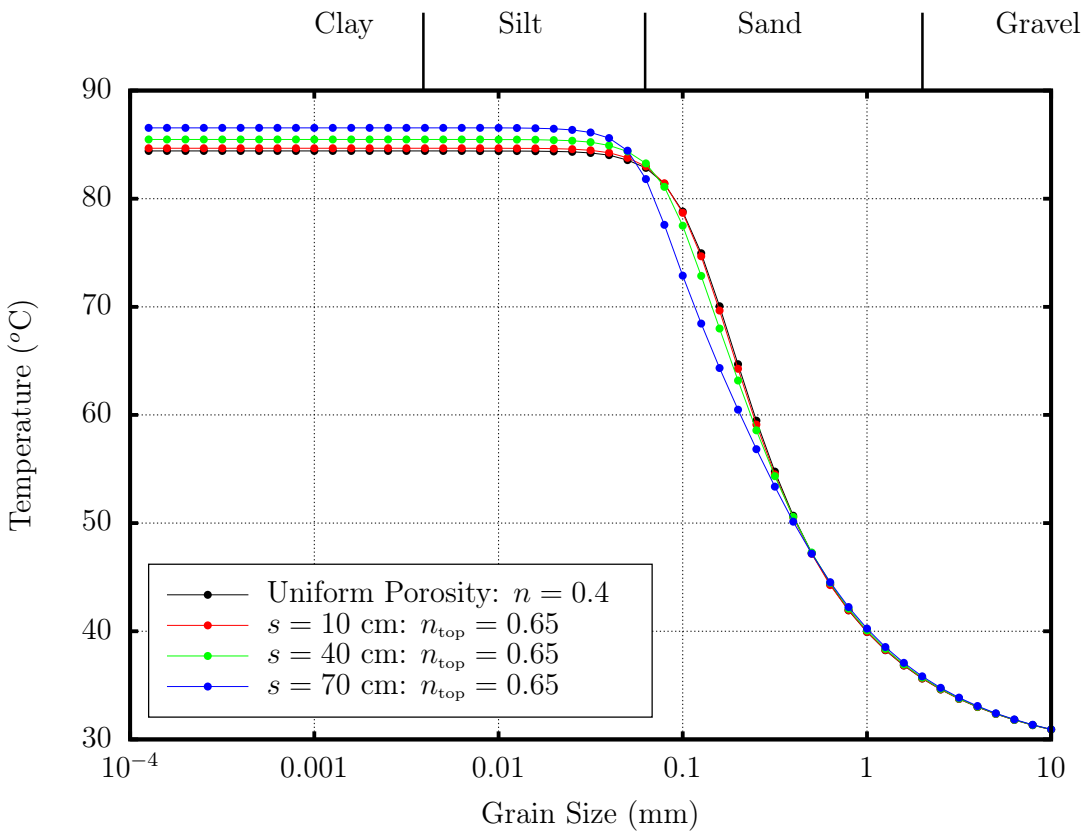

Fig. 5.11: A comparison of maximum cable conductor temperature for refilled scour pits of different depths. In each case, the total amount of overlying sediment (refilled and native) was 1 m. The depth of the sediment constituting the refilled pit in each case is given by s.

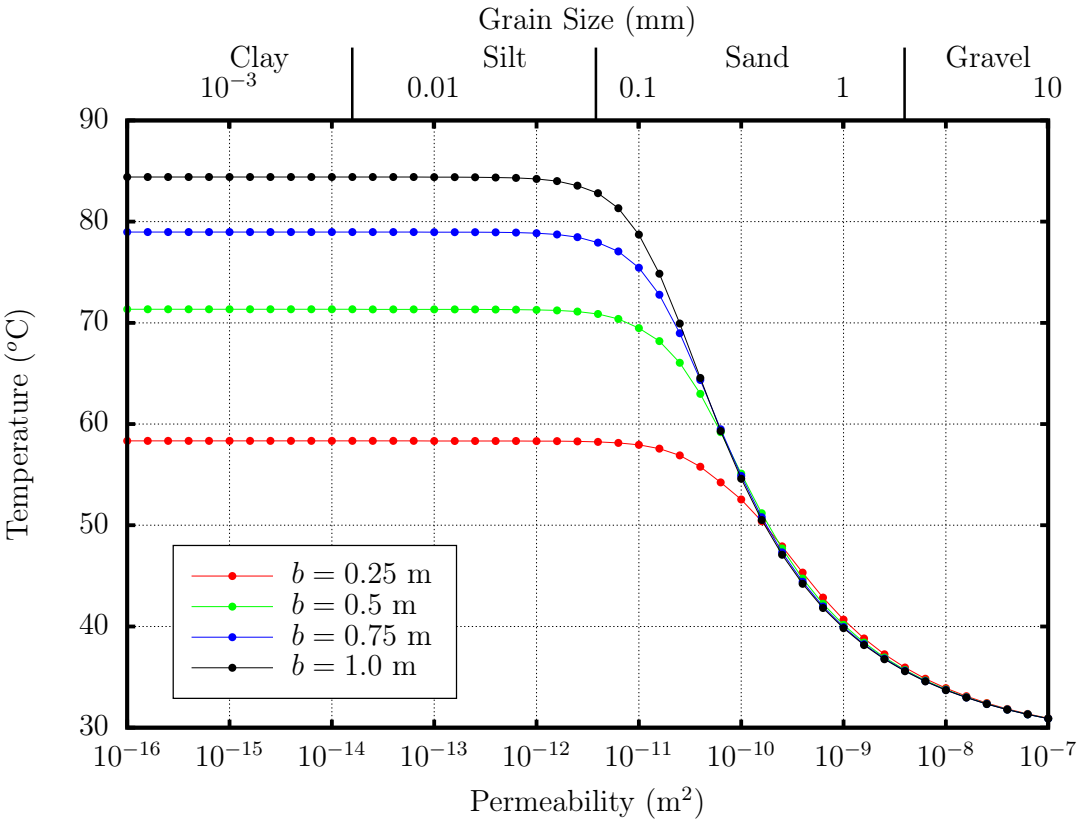

Fig. 5.12: Cable conductor temperature as a function of sediment permeability for four different cable burial depths. Approximate grain size equivalents (calculated using equation (3.54), assuming $n = 0.4$) for the permeabilities used in the model are given on the top axis

5.6 Discussion

Of the three potential sources of inhomogeneity discussed, discontinuities in the thermophysical properties between the trench and the native sediment have the greatest potential to have an appreciable impact on the temperatures of submarine HV cables. This is perhaps unsurprising, as this is the only scenario in which the altered inhomogeneous sediment is in direct physical contact with the cable surface. Additionally, the location of the altered sediment in the trench mirrors the path of any convective heat transfer, creating an uninterrupted route from source (the cable) to sink (seawater). Note that inhomogeneities arising from trenching are incapable of causing an increase in cable conductor temperatures above that of the homogeneous case in the low permeability limit (even if the trenched material is less permeable than the background - refer to Fig. 5.6). This is due to the simplified way in which the FEM models for this scenario have been set up; there is a discontinuity in permeability between the trench and background sediments, but

the porosity remains consistent between the two regions. The thermal behaviour of the simulated cable is independent of the permeability in the conductive limit (as permeability only affects convective heat flux), hence the similarity in results to the homogeneous case. In reality, changes in the permeability are likely to be induced (at least in part) by changes in the porosity (which can affect the conductive heat flux through the medium), a complexity which is beyond the scope of this simple model framework (but would allow the cable conductor temperatures to exceed those recorded for the case of a homogeneous sediment in the conductive limit if implemented). By contrast, the other two sources of sediment inhomogeneity investigated do predict cable conductor temperatures in excess of those expected for a completely conductive homogeneous sediment.

The deposition of low permeability sediment at the seabed surface was the only source of inhomogeneity that had an impact on the cable conductor temperatures even at medium to high permeabilities. At low permeabilities, the increase in conductor temperatures observed in Figure 5.9 can be attributed to the change in the burial depth of the cable, rather than an inhomogeneity in sediment properties.

It may seem to follow from the results in Figure 5.11 that the presence of refilled scour pit material will not significantly change the instantaneous thermal conditions around a cable (at least for shallow pits, and assuming no net change in burial depth). However, it is worth reiterating that the conductor temperature is still dependent on the burial depth of the cable for fine(r) sands that dissipate a significant amount of heat away from the cable by conduction. The processes of excavation and subsequent refilling of a scour pit involve changes in the burial depth of the cable. Hence, a transition from a homogeneous sediment to a scenario similar to the one detailed in Section 5.5 will involve significant changes in the thermal conditions around the cable. Comparing Figure 5.11 and 5.12 for very fine sands, it is clear that conductor temperatures are much more sensitive to the cable burial depth than they are to any porosity change brought about during the refilling of scour pits. Furthermore, the change in porosity brought on by the scour pit phenomenon in the FEM models was an extremely generous estimate, and is hence unlikely to have a significant effect on the thermal environment of real submarine HV cables.

One of the ways in which the environmental impact of HV cables is assessed (with respect to the thermal implications of operation) is through the "2 K criterion",[4] recommended by environmental conservation authorities in Germany. The motivation behind the regulation is to protect the habitat of marine organisms living

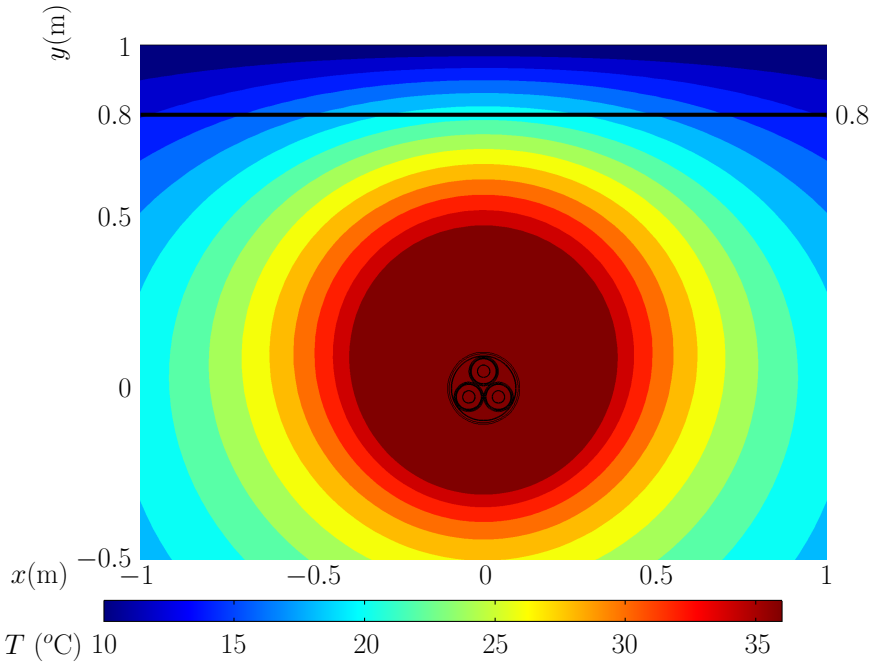

(a) Homogeneous: $\kappa = 10^{-11}$ m^2

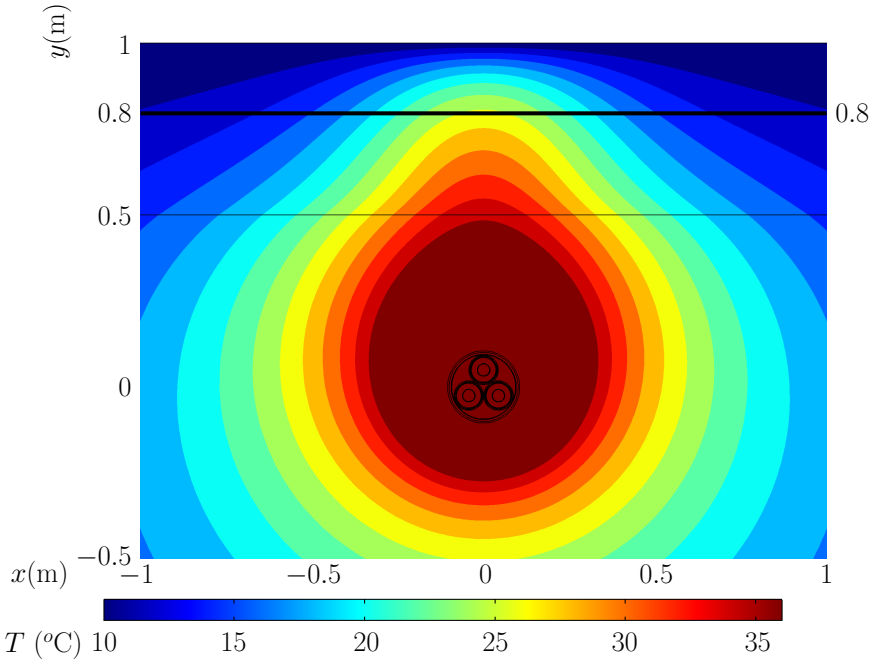

(b) Refilled scour pit: $\kappa = 10^{-11}$ m^2

Fig. 5.13: Illustrated above are the temperatures in the top 20 cm of the burial sediment for cables buried in (a), a homogeneous sediment (with a permeability of 10^{-11} m^2) and (b), a sediment with a 50 cm deep refilled scour pit. The top 20 cm of sediment in each case is above the thick black line. In both cases, temperatures in the top 20 cm of sediment reach 10 °C above ambient.

close to the seabed surface. The FEM simulations suggest that the 2 K criterion can be violated for some sediments that fall in the transition zone between conductive and convective behaviour. In these cases, the convective cooling effect is not strong enough to cool the cable conductors greatly, while still being large enough to reduce the isotropy of the net dissipation of heat (and ensure more heat is transported from the cable vertically upwards). This effect can be exacerbated by the presence of a refilled scour pit containing sediment with a higher porosity, and hence a higher permeability (see Figure 5.13).

5.7 Conclusion

Changes in the surrounding seabed environment can have significant implications for thermal considerations relevant to the operation of submarine HV cables. Being aware of the dynamic nature of the seabed, and the impact that inhomogeneity of the burial sediment may have on thermal situation of submarine HV cables can aid in more efficient and safer deployment of these assets.

- The greatest potential change in the thermal behaviour from sediment inhomogeneities is from changes in the thermophysical properties of the trench initially dug to accommodate the HV cable. For the permeability at which the difference from the homogeneous case is greatest, altering the grain size of the trench material by a factor of 10 induces a comparable change in the cable conductor temperature to reducing the cable burial depth from 1 m to 25 cm.

- The effect of any inhomogeneities in the sediment on cable temperatures is reduced for sediments with a naturally high permeability. This is especially true of the trench and refilled scour inhomogeneities.

- The discrepancy in cable temperatures between homogeneous sediments and sediments with permeability (or porosity) inhomogeneities is largest for sediments with permeabilities that fall in the transition region between conductive and convective heat dissipation.

- For sediments with a low permeability, changes in the burial depth of the cable can significantly alter the cable temperature. This effect is much stronger than any changes resulting from the presence of a refilled scour pit, or a layered deposit of impermeable material at the seabed surface.

CHAPTER 6

Time Dependent FEM Simulations

The FEM models detailed in Chapters 3 - 5 are all based on steady state solutions to the heat flow equation, equation (3.14). For a number of reasons, it would be valuable if the FEM techniques used in the models described in these chapters could be modified to incorporate time dependence. Variability in electricity demand means that real submarine HV cables are unlikely to be required to transmit power at their static rated current for prolonged periods of time.[4] Being able to model the temperature response time of a submarine HV cable (given the starting conditions and applied load) would be useful for assessing the duration for which the asset could be overloaded, allowing a higher current than the steady state rating to be transmitted for a limited amount of time.[4,188] Time dependent simulations also allow environmental factors that vary in time to be included in the model to improve the accuracy of the ratings calculations (one example of potential relevance to determining thermal ratings for submarine HV cables might be the consideration of seasonally variable seawater temperatures).

A time dependent model was developed to extend the scope of the original framework (as described and used in Chapters 3 - 5) to explore some of the topics mentioned above. Part of the motivation for this originated from a curiosity to learn how the temperature response of a cable buried in a low permeability sediment (with conductive heat dissipation only) might differ from one buried in a highly permeable sediment that, in a steady state, supports both conductive and convective heat transfer. Also of interest were the timescales required for the establishment of a stable, convective system.

6.1 Developing a 2D Time Dependent FEM Model

In Section 3.1 the expression in equation (3.10) was derived, providing a description of heat transfer through porous media from a combination of conductive and convective processes. In the steady state models described previously, the time derivative term in equation (3.10) is identically zero. The form of the heat transport equation that is implemented in the time independent FEM models is consequently given by equation (3.14). However, when time dependence is being considered, the term on the left hand side of equation (3.10) includes some new parameters that are not necessary in the time independent picture. As mentioned in Section 3.1, the density and specific heat capacity parameters in the convective component (rightmost term) of equation (3.10) refer exclusively to properties of

the permeating fluid (as only the fluid will be involved in the convection of heat). However, the density and specific heat capacity in the time derivative term on the left hand side of equation (3.10) are properties of the bulk medium. A more explicit way of writing equation (3.10) is:

$$\rho_b c_{p_b} \frac{\partial T}{\partial t} = Q_{\text{in}} + \lambda_b \nabla^2 T - \rho_f c_{p_f} \mathbf{u} \cdot \nabla T \tag{6.1}$$

where an assumption of incompressibility ($\nabla \cdot \mathbf{u} = 0$, see Section 3.1) has also been incorporated into this form of the equation. The density and specific heat capacity of the solid phase of the burial medium are set to $\rho_s = 2650$ kgm^{-3},[136] and $c_{p_s} = 700$ Jkg^{-1}K^{-1} respectively (approximately representative of a range of actual sediment types).[168,189] The bulk properties ρ_b and c_{p_b} are taken as simple arithmetic combinations of the separate phases, similar to the model for bulk thermal conductivity given in equation (3.15), *i.e.*:

$$\rho_b = (1 - n)\rho_s + n\rho_f \tag{6.2}$$

$$c_{p_b} = (1 - n)c_{p_s} + nc_{p_f} \tag{6.3}$$

Equation (6.1), combined with the form of Darcy's law expressed in equation (3.57) formed the basis of the time dependent FEM model.

6.2 Heat Up Time

The first time dependent FEM simulations to be run used the same geometrical configuration for the cable components and surrounding burial medium as the early time independent models (with a burial depth of 1 m). These simulations investigated the time taken for cables buried in sediments with different permeabilities to heat up from an ambient temperature to their steady state temperature (given a heat generation profile identical to the one used in the steady state simulations described in Chapters 4 and 5, with 100 Wm^{-1} distributed within the cable components according to the IEC 60287 standard). The times taken to reach equilibrium were inferred from inspection of the time dependent FEM model data by identifying the first interval (increasing logarithmically in time) for which the change in the conductor temperature was less than 0.25% of the difference between the maximum steady state (the values for which were taken from the time independent FEM simulations with identical environmental conditions) and ambient temperatures.

6.2.1 Results

The results presented in Chapter 4 showed that the dissipation of heat from cables buried in highly permeable sediments is much more effective, and results in considerably lower characteristic cable temperatures than for their counterparts buried in lower permeability sediments. The results from the first time dependent FEM models (presented in Table 6.1 and Figure 6.1) reveal that cables buried in low permeability sediments require a long time to heat up to a state of thermal equilibrium with their environment (many months, or sometimes longer). Conversely, cables in highly permeable sediments may take as little as a single day to heat up completely.

Permeability	T_{max}	**Time to Equilibrium**	
[m^2]	[°C]	[s]	[days]
$1.0 \cdot 10^{-14}$	84	$4.0 \cdot 10^{7}$	460
$1.0 \cdot 10^{-12}$	84	$4.0 \cdot 10^{7}$	460
$4.0 \cdot 10^{-12}$	83	$3.2 \cdot 10^{7}$	370
$1.0 \cdot 10^{-11}$	79	$1.6 \cdot 10^{7}$	180
$4.0 \cdot 10^{-11}$	65	$2.5 \cdot 10^{6}$	29
$1.0 \cdot 10^{-10}$	55	$7.9 \cdot 10^{5}$	9.2
$4.0 \cdot 10^{-10}$	44	$4.0 \cdot 10^{5}$	4.6
$1.0 \cdot 10^{-9}$	40	$2.0 \cdot 10^{5}$	2.3
$4.0 \cdot 10^{-9}$	36	$7.9 \cdot 10^{4}$	0.92
Outer serving at ambient T	28	$4.0 \cdot 10^{4}$	0.46

Table 6.1: Time taken to heat up a submarine HV cable from ambient to a state of thermal equilibrium. The time taken to reach equilibrium is defined as being the time after which the change in temperature between adjacent measurements (increasing logarithmically in time) becomes less than 0.25% of the total difference between the steady state (taken from the time independent FEM model solutions) and ambient temperatures. The bottom row represents the results from a simulation where the temperature of the outer surface of the cable was enforced to be at ambient.

The initial heat up of the cable conductors occurs at the same rate in each case shown in Figure 6.1, regardless of the permeability of the burial sediment. Only when the temperature of the cable conductors approaches the permeability dependent steady state temperature (as defined by the temperatures obtained from the time independent FEM simulations) does the rate of heating begin to slow down. This behaviour is likely (at least partially) attributable to the time taken

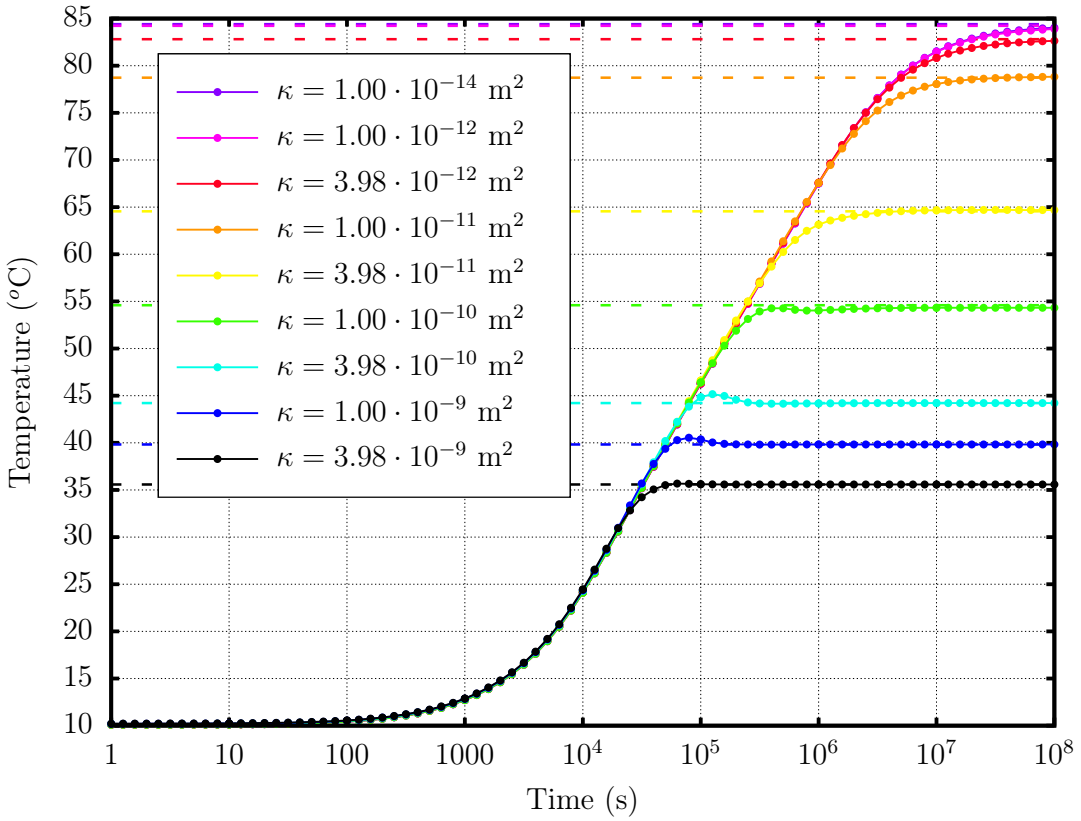

Fig. 6.1: Results from a time dependent FEM model illustrating the difference in the time taken for the conductors of cables buried in sediments with different permeabilities to heat up from ambient, to a steady state temperature. The dashed lines represent temperatures calculated by a steady state FEM simulation for an identical geometry and set of parameters.

for the cable components to heat up from their initial ambient temperature. A temperature gradient must be established across the entire cable before heat can be conducted through it, and into the surrounding environment. However, the thermal diffusivity of some of the cable components is quite low (see Table 3.8). A comparatively long time is therefore required for these components to heat up from ambient, and enable the conduction of heat outwards through the cable serving.

Once through the serving, the rate at which heat can be dissipated is determined by the environmental conditions. If the dissipation of heat through the surrounding sediment is perfectly efficient, the temperature at the outer surface of the cable will be maintained at ambient (as is the case for the bottom row of Table 6.1). An equilibrium will quickly be reached as the amount of heat lost to the environment rapidly approaches the amount generated within the cable. The bottom two rows of Table 6.1 indicate that a cable buried at depth in a highly permeable sediment has a comparable heat up time to one whose outer surface is artificially maintained

at an ambient temperature by enforcing a constant temperature boundary at the cable surface. Both scenarios fulfilled the criteria detailed above for estimating the point at which thermal equilibrium has been reached ($\Delta T/\Delta t \leq 0.0025 \cdot (T_h - T_0)$) after a similar length of time in the FEM model. This indicates that the dissipation of heat through a highly convective sediment is relatively effective. In this case, the time taken to heat the cable components up (to temperatures sufficient to conduct all of the internally generated heat out into the surrounding environment) accounts for the majority of the time required to reach a state of thermal equilibrium.

Heat dissipation in less permeable sediments is less effective. Not all the heat conducted through the serving can be dissipated immediately, which results in the heating of the sediment surrounding the cable. To reach a steady state, temperatures inside the cable must rise further to maintain a gradient with the surrounding sediment capable of dissipating the heat being generated within the cable. This increases the length of time needed for a state of thermal equilibrium to be reached.

6.3 Cool Down Time

Another set of simulations were run to investigate the time taken to cool the cable (the design used was identical design to the previous models) from a state of thermal equilibrium with its surroundings to an ambient temperature for a number of different sediment permeabilities. The initial temperature field within the simulation was specified by a corresponding solution to the steady state FEM simulations (detailed in Chapter 4) according to the sediment permeability being modelled. The heat generated within all cable components was set to be identically zero for the duration of the simulation. This corresponds to setting $Q_{\text{in}} = 0$ in equation (6.1). The model was then allowed to cool for a total of 10^8 s of simulated time.

6.3.1 Results

Illustrated in Figure 6.2 are the cool down times from equilibrium to ambient for a range of sediment permeabilities. In a similar manner to the results from the cable heat up simulations presented above, the temperature response times for cables buried in highly permeable sediments were much more rapid for the cooling phase. Despite this, the difference in cooling times is not quite as extreme as

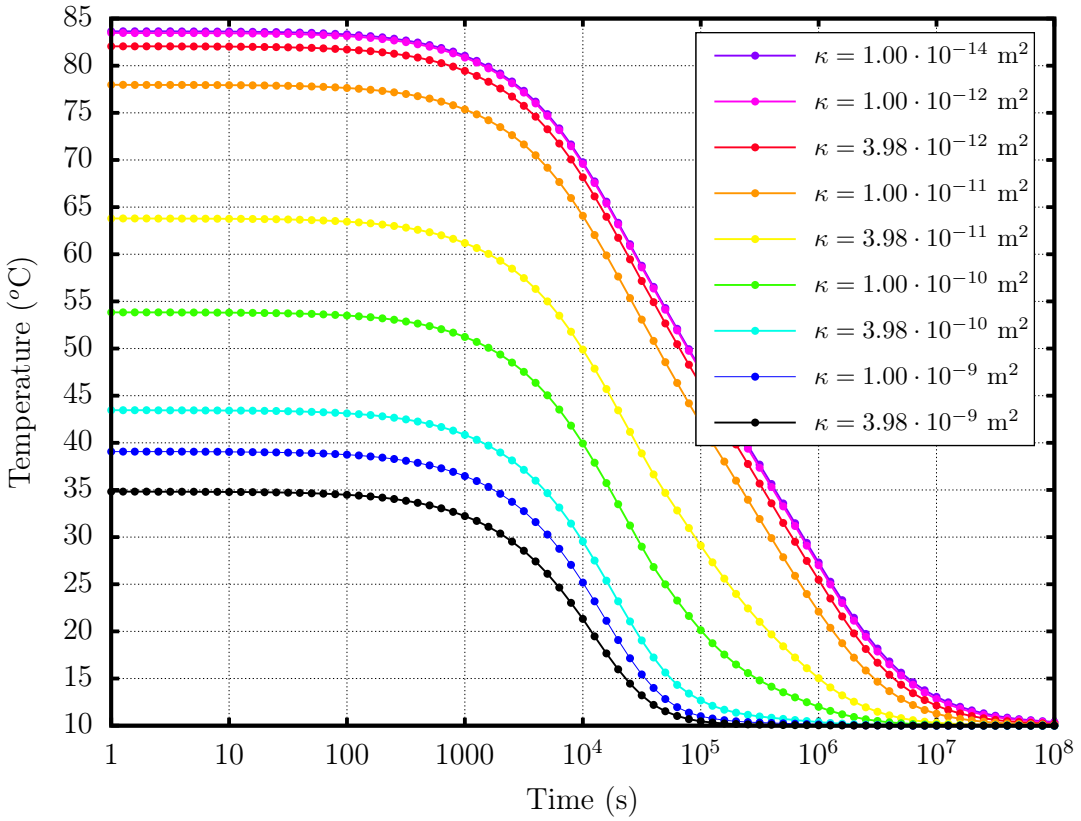

Fig. 6.2: Time dependent FEM model results depicting the time taken for the cable conductors to cool down from a steady state temperature to ambient (for a range of sediment permeabilities).

the difference between heat up times for cables buried in sediments with differing permeabilities. Even the most permeable sediment shown in Figure 6.2 takes over 10^5 s to approach ambient from a steady state. Cross-referencing with Figure 6.1, it can be seen that this is about half an order of magnitude more time than was required to heat up a cable buried in a similar environment to a steady state. Conversely, the heat up and cool down times for the low permeability sediment were reasonably consistent.

6.4 Comparing Heat up and Cool Down Times

The discretised temperature differential after 10^8 s for the least permeable sediment investigated ($\kappa = 10^{-14}$ m^2) for the heat up and cool down phases were similar, with a change of $+0.079$ °C and -0.085 °C respectively in the final $2.07 \cdot 10^7$ s of simulated time (between the penultimate, and final times in the data set). By comparison, the discretised temperature differentials for the $\kappa = 3.98 \cdot 10^{-9}$ m^2

sediment after 10^5 s were $+0.023$ and -0.15 °C respectively. The discrepancies between the heat up and cool down times of cables buried in sediments with permeabilities of 10^{-14} and 10^{-9} m^2 are illustrated in Figure 6.3

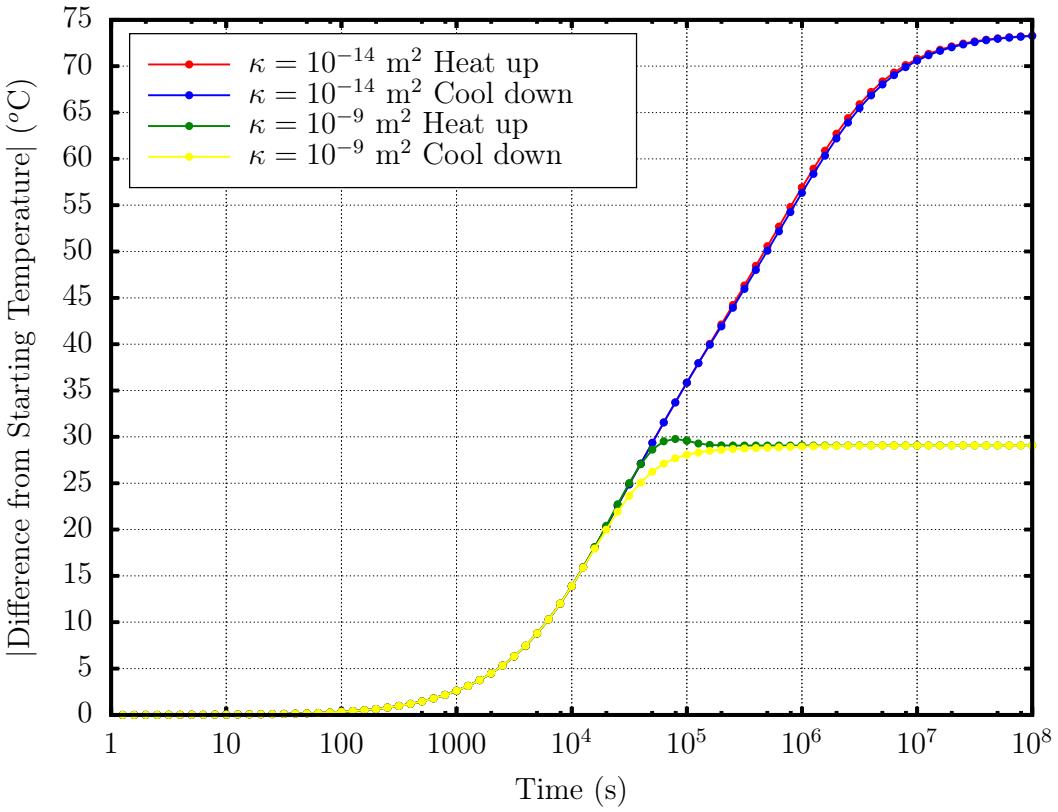

Fig. 6.3: Time dependent FEM model results depicting how the maximum temperature of the cable conductors evolves in time from its initial value. Both heat up and cool down phases are represented.

The reason for the discrepancy between heat up and cool down times for highly permeable sediments may be related to the definition that has been used for what constitutes a "steady state". The cable conductors are encased within the XLPE insulation, which has a comparatively low thermal diffusivity (see Table 3.8). It may be that this slows the diffusion of heat away from the conductors on a timescale that is noticeable in the case of a highly permeable sediment, but not for a low permeability sediment (given that the time taken to reach equilibrium for low permeability sediments is greater by a factor of $\sim$ 100 - 1000). Another contributing factor to this is the considerable amount of heat that is generated outside of the conductors, through induced currents in the cable sheaths and armour. This may quicken the heat up phase relative to the cool down phase, as heat generated in these components does not have to pass through the thermally resistive XLPE insulation before it can be dissipated into the surrounding environment. During

the cool down phase, the conductor will remain warm, contained within the insulation while the sheath, armour, and other outer components experience more rapid cooling. However, the metric for determining when thermal equilibrium has been reached during this phase relies solely on the conductor temperature, hence the longer time required for cool down.

6.5 Discussion

The temperature response of submarine HV cables depends greatly on the permeability of the sediment into which they are buried. As with the steady state simulations, the greatest change in behaviour occurs during the transition from conductive to convective heat dissipation. The maximum time required for a cable to heat up will occur for a sediment that does not support any convective heat dissipation at all (this is illustrated by the consistency in heat up times between the 10^{-14} and 10^{-12} m^2 permeability sediments in Figure 6.1). The shortest possible time taken to reach thermal equilibrium will occur in the hypothetical case in which the outer serving of the cable is maintained at ambient temperature by a perfectly efficient convective cooling effect within the burial medium.

The similarity in the temperature response (particularly the heat up times) between cables buried in highly permeable sediment, and those with a surface at ambient temperature indicates that the dissipation of heat through highly convective sediments is very effective. The heat up time for cables in these sediments is primarily dictated by the heat up time of the internal cable components. By contrast, for conductive sediments, the dissipation of heat through the surrounding sediment accounts for a much larger proportion of the total time required to reach a state of thermal equilibrium.

Using a percentage change in the temperature of the cable conductors to gauge whether the simulated cable had reached a state of thermal equilibrium revealed that the heat up and cool down times differed for cables buried in high permeability sediments. The choice of this metric is not altogether unwarranted, as the temperature of the cable conductors is of primary importance when considering implications for the current ratings of submarine HV cables. However, this may not result in a representative impression of how heat is dissipated from the cable as a whole.

It is interesting to consider the implications of the dependence of the temperature response in the wider context of the day to day operation of submarine HV cables. The temperature of cables buried in convective sediments will respond quickly to changes in their current load. It seems *prima facie* that this would limit the amount of time that these assets can be safely overloaded. However, it must also be recognised that it is unlikely that a cable passing through a variety of different sediments will be thermally limited by sections of convective sediment (the equilibrium temperature for these environments is lower than it is for conductive sediments, despite the faster temperature response). Care must be taken to acknowledge the asymmetry between the heat up and cool down periods for cables buried in highly permeable sediments to ensure that they are sufficiently cooled after a period of overloading. On the other hand, it is unlikely that submarine HV cable sections (either interconnectors, or renewable energy export cables) buried in conductive sediments will be required to operate constantly at (or above) their rated current for the lengths of time that Figure 6.1 suggests would be required for them to approach thermal equilibrium (many months to years). Overloading of cables buried in conductive sediments should be possible for more prolonged periods, due to the slower temperature response time. Caution must still be taken in these cases, however, to ensure that the relaxation time after a period of overloading is sufficient to cool the cable before the asset is overloaded again.

It should be noted at this point that the bulk thermal conductivities of the sediments modelled in Figures 6.1 and 6.2 are identical, as the permeability parameter in the simulations has been altered while leaving the porosity (and hence the thermal conductivity) consistent. Were the porosity, and hence thermal conductivity (*i.e.* the efficiency of conductive heat transfer) of the burial sediment to vary between the cases displayed in Figures 6.1 and 6.2, the time response would also differ for the less permeable scenarios, as seen in Figure 6.4.

Finally, it is worth noting that it should be possible to infer the permeability of the sediment into which a given submarine HV cable is buried given its temperature response (or possibly even the difference between the temperature response of its heat up and and cool down phases). Hence, an augmented current rating that takes account of any convective cooling in the burial sediment can be calculated at points along existing cables without the need to conduct surveys to directly determine the properties of the seabed material.

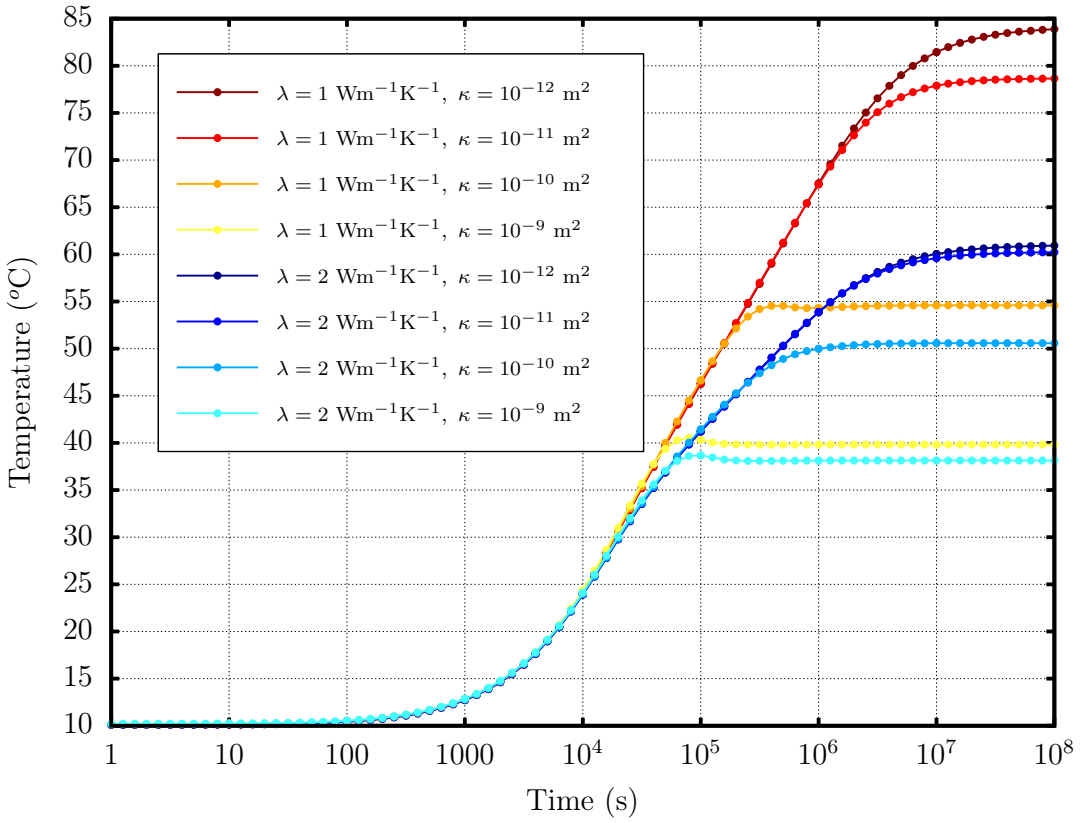

Fig. 6.4: Comparison of conductor heat up times for cables buried in a sediment with a thermal conductivity of 1 $\mathrm{Wm^{-1}K^{-1}}$ (red shades), and one with a thermal conductivity of 2 $\mathrm{Wm^{-1}K^{-1}}$ (blue shades).

CHAPTER 7

Discussion and Conclusions

The work presented herein has been predominantly concerned with investigating the thermal conditions that operational submarine HV cables are exposed to; a topic that thus far has been surprisingly under-examined considering their increasing prevalence, and the increasing breadth of available literature on analogous investigations into the thermal environments of terrestrially buried cables. Of particular interest, therefore, was how the environmental conditions under which submarine HV cables operate might differ from the conditions experienced by their counterparts on land, and the extent to which these environmental differences could induce changes in the thermal behaviour of the cable. Determining the potential impact of any physical processes unique to the submarine environment on the operation of HV cables was also of interest.

The theoretical background of the problem was set out in Chapters 2 and 3. The design of submarine HV cables, and the physical mechanisms behind the generation of heat within them were laid out in Chapter 2. The IEC 60287 standard was also introduced in this chapter.

The equations that describe coupled heat and fluid flow through a porous medium, and the various parameters that appear in them were introduced in Chapter 3. Of particular interest was the permeability of the burial medium, and the extraordinary range it exhibits between different naturally occurring marine sediments. It was hypothesised that the permeability of the sediment is the environmental parameter most likely to significantly alter the thermal behaviour of submarine HV cables.

The results from the first FEM simulations are presented in Chapter 4. Several environmental parameters were varied to evaluate their impact on the nature of the heat dissipation from the cable. These simulations show that the most influential parameter in determining the effectiveness of the dissipation of heat into the surrounding burial environment is the sediment permeability.

The seabed burial environments of many submarine HV cables may not be particularly well represented by the idealised sediment used in the models in Chapter 4. Chapter 5 extends the applicability of the simple FEM model introduced in the previous chapter to several inhomogeneous burial scenarios. The greatest change in the thermal conditions compared with a cable buried in a uniform medium occurs when the properties of the sediment contained in the trench region are altered. Cables with a time varying burial depth are also subject to large changes in their thermal conditions.

An introduction to time dependent FEM simulations of submarine HV cables was given in Chapter 6. The time taken to reach a state of thermal equilibrium was found to depend on the permeability of the sediment. Cables buried in highly permeable sediments reach their steady state temperature after considerably less time than conductive sediments.

7.1 Contribution of Work

A series of 2D FEM models have been developed to address the questions posed above. Simulations were developed with an appreciation of the existing methods for modelling land-based cables (in terms of the approaches followed and equations used) as the foundation for their development. However, the FEM models developed herein derive their individuality from the commitment to the hypothesis that the differences between land and submarine cable burial environments will result in a difference in the thermal behaviour between the two cases. Hence, the thermal behaviour of submarine HV cables requires a unique description that is distinct from that of the more familiar terrestrial setting.

One of the main insights provided by the results from the FEM simulations is that under certain circumstances, convection can play a significant role in the dissipation of heat from submarine HV cables. This conclusion runs contrary to the established expectations and predictions regarding the thermal state of cables buried on land. Convection is traditionally neglected or downplayed in ratings calculations for terrestrial cables; the only consideration of a fluid phase is whether the cable temperatures will cause localised drying of the substrate (and hence alter the bulk thermal conductivity of the medium). The behaviour predicted by the FEM models developed herein can ultimately be attributed to a difference in burial environments between land and submarine cables. The additional convective cooling effect is enabled by recharge from the water layer and is largely controlled by the intrinsic permeability of the sediment. The extent of the influence that the permeability of the burial sediment has over the temperatures in and around a submarine HV cable is evidenced by the depiction in Figure 7.1. When plotted on identical temperature scales to facilitate a direct comparison, it becomes very clear that the range in thermal behaviour that can result from variations in the sediment permeability is monumental.

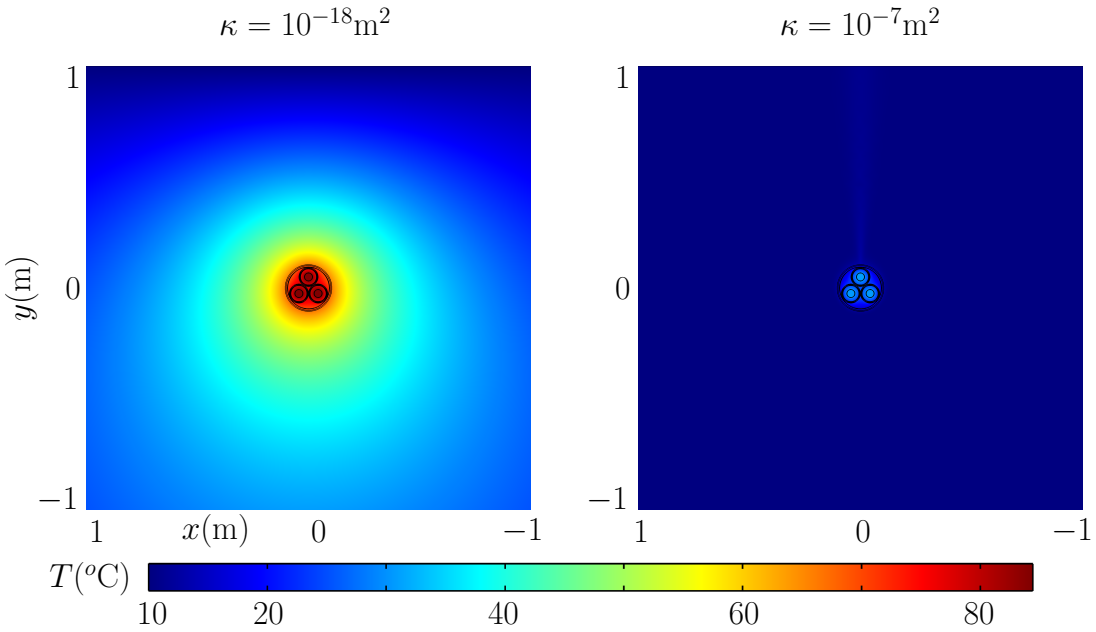

Fig. 7.1: Temperatures predicted by the FEM model in and around two cables are illustrated here. The only difference between the two cases is the permeability of the surrounding sediment: 10^{-18} m^2 and 10^{-7} m^2 for the left and right hand figures respectively.

There are a number of important implications that this additional convective dissipation has for the design, manufacture, installation, and operation of submarine HV cables:

- The thermal current ratings for cable sections that pass through sediments that can support convective heat dissipation can be raised significantly (by 100s of Amps, see Figure 4.9). While cables themselves are seldom the thermally limiting component of a transmission system (*cf.* J-tubes and beach landings,[178,190,191] for example), the potential increase in transmissive capacity may be large enough in individual circumstances to warrant considering taking advantage of this by artificially cooling the limiting components and sections (an admittedly costly venture).

- Maintaining the cable at lower temperatures through increased convective dissipation helps to slow the rate of degradation of the XLPE insulation, prelonging the thermal lifetime of the cable. A reduction in the operational temperature of a cable by $\sim$ 10 °C due to convective cooling might see its thermal lifetime approximately double[4] (see Section 1.2). Furthermore, the resistance of the cable conductors is dependent on their temperature according to equation (2.13). Joule losses in the conductors will be reduced if the cable operates at a lower temperature.

- Alternatively, considering the contribution to the thermal dissipation from convection during the design stage of submarine HV cable routes would allow sections of, or even the entire cable (depending on the nature of the seabed along the route) to be manufactured using less material (and hence a considerably lower cost) for the conductor(s).

  For example, the amount of copper required for all three conductors in a cable identical in design to the one used in the FEM simulations in Chapters 4 - 6 is:

$$\begin{aligned} 3 \cdot \pi r^2 \cdot \rho &= 3 \cdot \pi (0.0343/2)^2 \ \cdot 8960 \\ &= 24.8 \text{ kgm}^{-1} \end{aligned} \tag{7.1}$$

  If the diameter of the conductors could be reduced by just two millimetres to 32.3 mm, the amount of copper required would be reduced by over 10% to 22.0 kgm^{-1}. For a 100 km long cable, this is equivalent to a saving of around 280 tonnes of copper (2200 tonnes, down from 2480). Using a copper price of £3780 per tonne,[192] the potential saving in raw copper for the same 100 km cable is:

$$\begin{aligned} \text{Money saved} &= \frac{(24.8 - 22)}{1000} \cdot 100000 \cdot 3780 \\ &= £1.06 \text{ million} \end{aligned} \tag{7.2}$$

- In some circumstances, information on the seabed composition could even help to inform the cable route itself, if, for example a slightly longer route will pass through a shorter length of thermally detrimental sediment than a more direct one. It may consequently become economically preferable to lay the cable along the longer route due to either one, or a combination of the reasons listed above.

- The conclusions presented in Chapter 6 regarding the dependence of the cable temperature response time on the permeability of the sediment may help to refine techniques for setting dynamic cable ratings. FEM simulations similar to the one outlined in this chapter could be modified to caculate cable heat up (and cool down) times given the cable burial conditions and desired current load.

Another factor that is often underappreciated is the dynamic nature of the seafloor environment compared with the relatively static burial conditions for typical cables on land. As seen in Chapter 5, for conductive sediments the depth of burial below

the seawater is very influential in determining the thermal conditions to which a submarine HV cable will be exposed. This sensitivity to burial depth is echoed in existing treatments of cables buried on land, for example as in the IEC 60287 standard. However, burial depth is perhaps an even more important factor in the marine environment, as the seawater overlying the burial medium of submarine HV cables provides a much more effective heat sink than is available for land based cables. This combination of short dynamic timescales and prominence in determining the thermal environment has the potential to result in comparatively volatile cable behaviour.

One obvious source of inaccuracy within the model originates from the difficulties associated with obtaining an accurate value for the permeability of the burial sediment. Relationships between the permeability and other physical characteristics of the sediment are often oversimplified in their approach, emphasising range of applicablility over accuracy. Direct measurements can be technically challenging to undertake, and evaluate the permeability only at discrete locations. It may be possible to use the seismic characteristics of a sediment (possibly combined with permeability/grain size relations, or measurements of other quantities) to estimate the permeability. Vardy 2015[193] investigated the correlation between the mean grain size and porosity of marine sediments, and their measured acoustic impedance. It was discovered that smaller grain sizes and larger porosities corresponded to a lower acoustic impedance, and that these relations could be used to obtain a reliable estimate for the mean grain size and porosity of a sediment. This technique may provide some useful insight into the permeabilities of marine sediments with further development, and perhaps in combination with measurements of other quantities.

It is possible (albeit technically challenging, and comparatively costly) to measure the *in situ* permeability using other techniques, like those described near the beginning of Section 3.5. With further development, one of these methods may be suitable for determining the permeabilities of marine sediments into which submarine HV cables are buried. In time, it may be possible to use them in conjuction with the FEM models developed herein to predict the nature of the heatflow in different sediments along the route of a cable, and help to inform their current ratings.

7.2 Future Work

7.2.1 3D Simulations and Experiments

One of the limitations associated with both the simulations presented and experiments discussed herein is that they both aim to model a 3D system using a 2D approximation of the geometry. As stated in Appendix B, there were a number of complications that arose when attempting to directly compare the tank experiments and the FEM models. With further meticulous investigation, it may be possible to definitively identify the ultimate origin of the discrepancy in behaviour between the tank experiments and the FEM models (several hypotheses are discussed in Section B.2). Alternatively, a more representative description of the thermal situation of a real submarine HV cable could be obtained through the development of a 3D FEM model, or experiments in a fully 3D tank. Neither of these ventures have been explored significantly, due to a combination of financial, practical, and temporal constraints.

A 3D experiment would, at the very least, require a larger tank, more thermocouples, and more lab space (and therefore a larger budget). If possible, it would be desirable for the heat source used in the experiment to consist of a short section of an authentic submarine HV cable. This would recreate the *in situ* conditions experienced by installed cables more accurately than using a solid metal heat source analogous to the one used in the 2D tank experiments. Acquisition of such a cable section would necessitate collaboration with an industrial partner, which may bring with it its own delays and complications assuming a willing co-operator could be found at all. The duration of any experiments with a 3D tank may also take considerably longer to complete (*i.e.* reach a state of equilibrium) than the smaller scale 2D experiments that have been completed thus far.

Hindrances in the development of a 3D model are more technical in nature than financial. The time taken to solve the relevant system of PDEs is greatly increased for models in 3D. This not only increases the run time of the final model, but also the effective development time as well. More memory is required to run 3D models at a sufficient mesh resolution. In order to run the 3D models analogous to the 2D models detailed herein, machines require a relatively large amount of RAM; a limited number of nodes with sufficient RAM were available for use at the University of Southampton during the timeframe of the work (a problem that did not arise for the 2D models). Furthermore, the highly convective scenarios

with greater fluid velocities appear to cause increased instability in all available solver methods implemented in the FEM model software. Obtaining a convergent solution consequently becomes much more challenging in 3D.

If the challenges associated with constructing a functional 3D FEM model or 3D experiment as described above could be overcome, pursuing these avenues of research would be one obvious way to expand upon the work that has already been done. A 3D experiment in particular would provide the closest replication of the *in situ* conditions and thermal environment of submarine HV cables of which the author is aware.

7.2.2 Online DTS Measurements

Many contemporary submarine HV cables are equipped with distributed temperature sensing (DTS) systems to provide temperature monitoring in real time. These systems consist of a bundle of optical fibres that run parallel to the cable axis (within the outer serving), down which pulses of light are sent. After a certain time proportional to the distance along the cable, backscattered light returns to a detector (at the same end of the cable from which the light pulse was sent). This backscattered light includes two components: the "Stokes" band, the intensity of which is dependent on temperature, and the "anti-Stokes" band, which is not. The temperature at a given distance along the cable can be inferred from the ratio of the intensities of these two components.[57] Online temperature measurements using DTS systems can be used to provide dynamic cable ratings that can be used to supplement the conventional static cable ratings by taking into account the current ambient conditions, and to justify temporary overloading of cables.[4]

There is a tantalising possibility that recognition and appreciation of the role that convection has in the dissipation of heat from submarine HV cables may allow further predictions to be made about the cable environment through the contextual analysis of cable DTS data. For example, by considering the temperature time response to a change in the cable load, it should be possible to constrain the extent to which convection is responsible for the dissipation of heat from the cable. A sluggish time response would indicate that the cable is likely buried in a low permeability sediment. A rapid temperature response would indicate that a significant amount of heat is being transported away from the cable by convection. In the latter case, it may be challenging to determine whether this convection is occurring because the sediment in which the cable is buried is highly permeable,

or whether the cable has become directly exposed to the seawater through seabed processes (*e.g.* scouring).

Analysis of rapid temperature response times arising in cable DTS data could provide an additional warning criterion for assessing the likelihood that a particular section of cable has experienced a reduction in burial depth, or even become exposed directly to the seawater through excavation of the burial sediment. This could be accomplished by observing changes in the temperature response for a section of the cable over time. Sections determined to be at risk could be investigated further by using non-invasive seismic reflection surveys of the section to determine the burial depth of the cable.

A further empirical test of the predictive capabilities of the FEM models developed herein could be provided by combining data from DTS measurements with information about sediment grain size, and cable burial depth acquired from sub-bottom acoustic profiling. If it can be confirmed that a particular section of cable remains buried at a reasonable depth, the temperature response time of the DTS measurements can be predicted from the permeability of the sediment (which can be estimated from the grain size data), according to the behaviour documented in Chapter 6. If it could be demonstrated that the temperature response of DTS measurements for *in situ* submarine HV cable sections is dependent on the permeability of the burial sediment (as described by the trends observed in the time dependent FEM models presented in Chapter 6), it would considerably strengthen the conclusion that convection can play a significant role in the dissipation of heat away from submarine HV cables.

APPENDIX A

Current Density Perturbation due to the Skin Effect

The current density for an alternating current in a cable with a circular cross-section can be derived by considering the induced electric and magnetic fields caused by the switch in current direction. Maxwell's equations are the fundamental equations in classical electrodynamics used for describing the electric and magnetic fields, $\mathbf{E}$ and $\mathbf{B}$. They are:

$$\nabla \cdot \mathbf{E} = \frac{\rho_c}{\varepsilon} \tag{A.1}$$

$$\nabla \cdot \mathbf{B} = 0 \tag{A.2}$$

$$\nabla \times \mathbf{E} = -\frac{\partial \mathbf{B}}{\partial t} \tag{A.3}$$

$$\nabla \times \mathbf{B} = \mu_{\mathrm{B}}\mathbf{J} + \mu_{\mathrm{B}}\varepsilon\frac{\partial \mathbf{E}}{\partial t} \tag{A.4}$$

where ρ_c, μ_{B}, ε, and $\mathbf{J}$ are the charge density, magnetic permeability, electric permittivity and current density respectively. Taking the curl of equation (A.3) and using the well known vector calculus identity $\nabla \times \nabla \times \mathbf{A} = \nabla(\nabla \cdot \mathbf{A}) - \nabla^2\mathbf{A}$[44] gives:

$$\nabla \times \nabla \times \mathbf{E} = -\frac{\partial}{\partial t}\Big(\nabla \times \mathbf{B}\Big)$$

$$\nabla(\nabla \cdot \mathbf{E}) - \nabla^2\mathbf{E} = -\frac{\partial}{\partial t}\Big(\nabla \times \mathbf{B}\Big) \tag{A.5}$$

By considering the continuity equation[44] for electric charge in combination with equation (A.1), and Ohm's law, $\mathbf{J} = \sigma\mathbf{E}$ it can be concluded that:

$$\frac{\partial \rho_c}{\partial t} = -\nabla \cdot \mathbf{J}$$

$$\frac{\partial \rho_c}{\partial t} = -\sigma\nabla \cdot \mathbf{E}$$

$$\frac{\partial \rho_c}{\partial t} = -\sigma\frac{\rho_c}{\varepsilon}$$

$$\Rightarrow \rho_c(t) = \rho_c(0)e^{-(\sigma/\varepsilon)t} \tag{A.6}$$

Hence, for a good conductor, the time taken to dissipate any free charge will be much smaller than the mean time between collisions,[44,194] and equation (A.1) can be approximated by $\nabla \cdot \mathbf{E} = 0$.[44] Hence, from equation (A.5):

$$\nabla^2\mathbf{E} = \frac{\partial}{\partial t}\Big(\nabla \times \mathbf{B}\Big) \tag{A.7}$$

Then, using equation (A.4), the previous equation can be expressed in terms of the electric field only, and then in terms of the current density by using Ohm's law once again:

$$\begin{aligned}
\nabla^2\mathbf{E} &= \frac{\partial}{\partial t}\left(\mu_{\mathrm{B}}\mathbf{J} + \mu_{\mathrm{B}}\varepsilon\frac{\partial\mathbf{E}}{\partial t}\right) \\
\frac{1}{\sigma}\nabla^2\mathbf{J} &= \frac{\partial}{\partial t}\left(\mu_{\mathrm{B}}\mathbf{J} + \frac{\mu_{\mathrm{B}}\varepsilon}{\sigma}\frac{\partial\mathbf{J}}{\partial t}\right) \\
\nabla^2\mathbf{J} &= \mu_{\mathrm{B}}\sigma\frac{\partial\mathbf{J}}{\partial t} + \mu_{\mathrm{B}}\varepsilon\frac{\partial^2\mathbf{J}}{\partial t^2}
\end{aligned} \tag{A.8}$$

For good conductors the displacement current, $\mathbf{J_D} = \varepsilon\partial_t\mathbf{E}$ that arises as a consequence of Maxwell's correction to Faraday's law, equation (A.4) can be neglected.[64] This can be confirmed heuristically by comparing the orders of magnitude of the displacement current, $\mathbf{J_D}$ to the current arising from Ohm's law, and approximating ∂_t to scale as $\sim\omega$:

$$\frac{\mathbf{J_D}}{\mathbf{J}} = \frac{\varepsilon\omega}{\sigma} \tag{A.9}$$

This ratio is very much less than unity for a good conductor, and hence the term $\mu_{\mathrm{B}}\varepsilon\partial_t^2\mathbf{J}$ in equation (A.8) can be neglected. By making the additional assumption that the system is rotationally and axially symmetric ($\partial_\theta = \partial_z = 0$), expressing ∇^2 in cylindrical coordinates,[80] and assuming $\mathbf{J} = J_z\hat{\mathbf{z}}$, equation (A.8) becomes:

$$\begin{aligned}
\frac{1}{r}\frac{\partial}{\partial r}\left(r\frac{\partial J_z}{\partial r}\right) &= \mu_{\mathrm{B}}\sigma\frac{\partial J_z}{\partial t} \\
\frac{\partial}{\partial r}\left(r\frac{\partial J_z}{\partial r}\right) &= r\mu_{\mathrm{B}}\sigma\frac{\partial J_z}{\partial t} \\
r\frac{\partial^2 J_z}{\partial r^2} + \frac{\partial J_z}{\partial r} &= r\mu_{\mathrm{B}}\sigma\frac{\partial J_z}{\partial t}
\end{aligned} \tag{A.10}$$

If the frequency of the reversals in current is ω, then the current density at some point in the cable can be described as a function of time by $J_z(t) = J_z(0)e^{-i\omega t}$. Correspondingly:

$$\begin{aligned}
\frac{\partial J_z}{\partial t} &= J_z(0)e^{-i\omega t}\cdot -i\omega \\
&= -i\omega J_z(t)
\end{aligned} \tag{A.11}$$

Hence, with a bit of algebraic rearrangement, equation (A.10) becomes:

$$r\frac{\partial^2 J_z}{\partial r^2} + \frac{\partial J_z}{\partial r} = r\mu_{\mathrm{B}}\sigma(-i\omega J_z)$$

$$r^2\frac{\partial^2 J_z}{\partial r^2} + r\frac{\partial J_z}{\partial r} + r^2(i\mu_{\mathrm{B}}\sigma\omega)J_z = 0 \tag{A.12}$$

To tidy this equation up slightly, the following change of variables can be made:

$$\upsilon = r\sqrt{i\mu_{\mathrm{B}}\sigma\omega} \tag{A.13}$$

$$\Rightarrow \frac{\partial J}{\partial r} = \frac{\partial \upsilon}{\partial r}\frac{\partial J}{\partial \upsilon}$$

$$= \sqrt{i\mu_{\mathrm{B}}\sigma\omega}\frac{\partial J}{\partial \upsilon} \tag{A.14}$$

Hence:[195]

$$r^2(i\mu_{\mathrm{B}}\sigma\omega)\frac{\partial^2 J_z}{\partial \upsilon^2} + r\sqrt{i\mu_{\mathrm{B}}\sigma\omega}\frac{\partial J_z}{\partial \upsilon} + r^2(i\mu_{\mathrm{B}}\sigma\omega)J_z = 0$$

$$\upsilon^2\frac{\partial^2 J_z}{\partial \upsilon^2} + \upsilon\frac{\partial J_z}{\partial \upsilon} + \upsilon^2 J_z = 0 \tag{A.15}$$

Equation (A.15) is of the same form as Bessel's equation, which has the solution:[64,80]

$$\upsilon = A\mathcal{J}_0 + B\mathcal{Y}_0 \tag{A.16}$$

where $\mathcal{J}_0$ and $\mathcal{Y}_0$ are Bessel functions of the first and second kind of order zero. However as r tends to zero, the function $\mathcal{Y}_0$ tends to infinity. Therefore B is equal to zero in equation (A.16), and υ can be expressed in terms of $\mathcal{J}_0$ only. If r' is the radius of the cable and $J_z(r')$ is the current density at the conductor surface, then the current density through the cable is described by:[64,65]

$$J_z(r,t) = \frac{\mathcal{J}_0\left(r\sqrt{i\mu_{\mathrm{B}}\sigma\omega}\right)}{\mathcal{J}_0\left(r'\sqrt{i\mu_{\mathrm{B}}\sigma\omega}\right)}|J_z(r')| \cdot e^{-i\omega t} \tag{A.17}$$

The Bessel functions can be calculated by taking the real part of[65]

$$\mathcal{J}_0(\upsilon) = \sum_{j=0}^{\infty}(-1)^j\frac{(\upsilon/2)^{2j}}{j!\Gamma(j+1)}$$

which, in our case reduces to:

$$\mathcal{J}_0(\upsilon) = \sum_{j=0}^{\infty} \frac{(\upsilon/2)^{4j}}{(2j)!\Gamma(2j+1)} \tag{A.18}$$

$$\because \left(\sqrt{\mu_{\text{B}}\sigma\omega i}\right)^N \in \mathbb{R} \text{ iff } N \in \{n \mid n = 4 \cdot n' \wedge n' \in \mathbb{N}_0\}$$

Figure A.1 displays an example calculation of the normalised current density in an AC cable. The figure clearly shows that the current density is greatest towards the surface of the cable, and considerably less current flows in the region towards the centre of the cable.

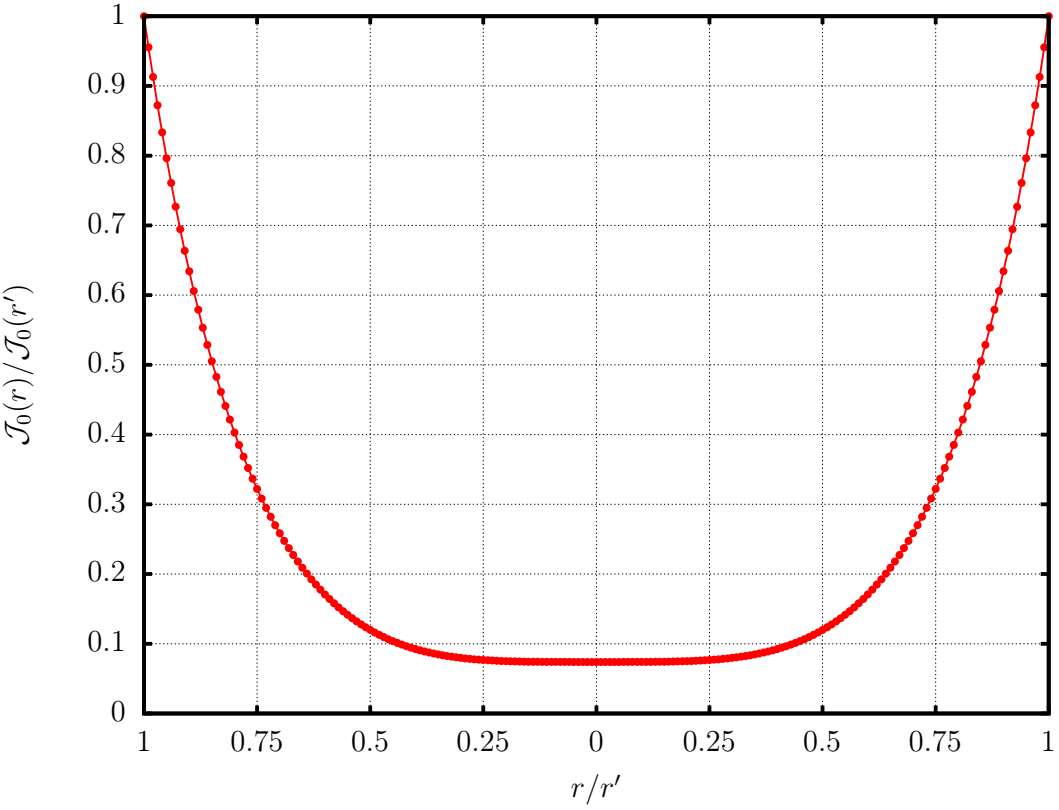

Fig. A.1: An example normalised Bessel function representing the current density in a longitudinal cross-section of a cable of radius r'. The AC frequency is 50Hz.

APPENDIX B

Verification of FEM Model Predictions

As part of a broader approach to investigating the thermal environment around submarine HV cables, a 2D tank experiment has been designed and constructed in one of the laboratories at the National Oceanography Centre Southampton (NOCS). One of the motivations behind this was to develop an alternative strategy for enquiry into the thermal behaviour of submarine HV cable systems by providing a physical analogue of the FEM models. In the context of the predictions made by the FEM model in chapter 4, it was hoped that the experimental results would deliver valuable supporting evidence (from a physical basis) for the phenomena observed in the model.

B.1 Experimental Setup

What follows is a brief outline of the apparatus used, and the experimental setup; a more thorough description (along with a comprehensive discussion of the results) is included in Emeana *et al.* 2016.[179] The tank itself is constructed from 2 cm thick perspex, reinforced with steel girders across its front and rear faces, and bolted to the floor of the lab. Figure B.1 shows the empty tank before any of the instrumentation or sediment was added. The dimensions of the tank are $2.5 \times 2.0 \times 0.1$ m.

The cable is represented in the experiment by a cylindrical heat source that was manufactured out of aluminium. This heat source has a radius of 11 cm and a length of 10 cm (the same as the width of the tank). The heat energy is supplied to the experiment via a coiled heating element located inside the aluminium shell. A wire leads from the top of the aluminium casing for connection to a voltage source. The heat source was fixed in place in the centre of the tank, at a distance of 1 m above its base. A regular grid of thermocouples was installed around the heat source by attaching them to nodal points in a square string net, as shown in Figure B.2. Based on the observation of convective phenomena in the results of some preliminary FEM simulations, it was decided to increase the density of the thermocouple mesh in the region of the tank above the heat source. It was hoped that the increased measurement resolution in this section of the tank would make it easier to identify any manifestation of convective behaviour that might occur during operation.

The tank was then filled with a synthetic sediment (called "ballotini") to a level approximately 1 m above the axis of the heat source. The ballotini was selected because it is composed of near-spherical grains, with a narrow size distribution

Fig. B.1: The empty experimental tank. See the yellow hard hat in the bottom right for scale.

(as close to an ideal sediment as possible). Once the tank was filled and fitted with several layers of sheet insulation on all sides, the heat source was switched on. Temperatures were recorded (automatically, via a data logger) at intervals of one minute until the tank reached an approximate state of thermal equilibrium (it usually required of the order of several days to a week to reach this point). This procedure was repeated at several different levels of heat input (between 5 and 50

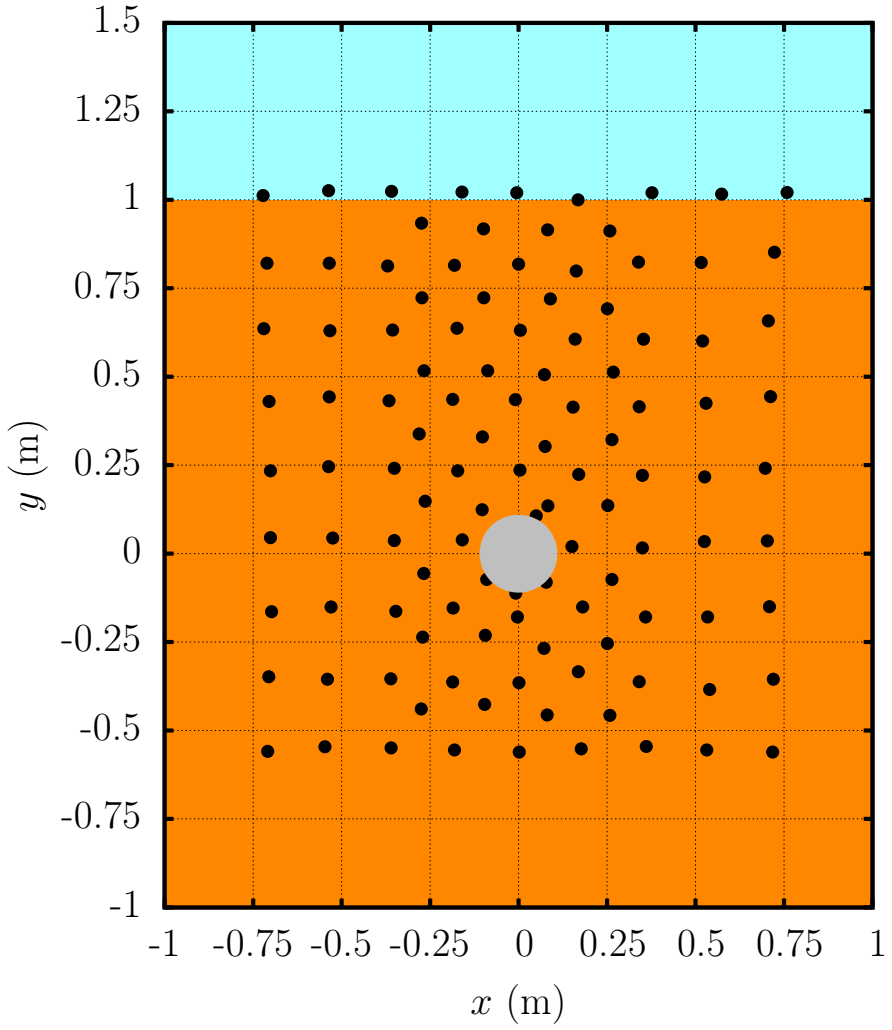

Fig. B.2: The positions of the heat source and the thermocouples are shown in this schematic. The centre of the heat source is used as the origin.

W), and for three different grades of ballotini. The permeabilities of each of the three different sediments was estimated using the Kozeny-Carman equation, after their grain size and porosity had been measured via sieving techniques,[196] and using the gravimetric grain volume approach[197] respectively. The calculated permeabilities for the three sediments were: $1.41{\cdot}10^{-13}$, $1.57{\cdot}10^{-11}$, and $1.49{\cdot}10^{-9}$ m^2. By cross-referencing these permeability values with the results presented in Figure 4.6(b) (and noting that the ballotini has a solid phase thermal conductivity of 0.94 $Wm^{-1}K^{-1}$, as stated by the manufacturers[198]), it is clear that the lowest

permeability is predicted by the FEM model to be well characterised by conductive heat dissipation. Similarly, the high permeability ballotini is predicted to be convective, while the medium permeability ballotini falls in the transition region between purely conductive, and purely convective thermal behaviour.

B.2 Results

The results of the tank experiment for the three different sediment types are displayed in Figure B.3. It is encouraging to note that the morphologies of the isotherms in these figures are very reminiscent of the corresponding plots for the results from the FEM model for similar sediment permeabilities presented in Figures 4.4 and 5.2. The results in Figure B.3 illustrate that, as predicted by the FEM models, the efficacy of the dissipation of an identical amount of heat supplied by the source is largely dependent on physical characteristics of sediment. In particular, the permeability (altered in the tank experiments by varying the grain size of the ballotini) of the sediment plays a key role in determining how effective this dissipation is.

Drawing a more quantitative comparison between the tank experiments and the FEM models is more difficult. The in depth analysis presented by Emeana *et al.* 2016 notes that the predictions of the FEM model and the tank results are consistent for sediment permeabilities in the conductive or convective limit. However, for the medium permeability (calculated to be $1.57 \cdot 10^{-11}$ m^2) ballotini which falls in the transition zone between conductive and convective behaviour, the FEM model that best matches the tank experiment has a slightly higher permeability, at $5 \cdot 10^{-11}$ m^2. There are a number of different plausible reasons for this discrepancy:

- The measurements of the grain size and/or porosity may not be perfectly accurate. Assuming a perfectly accurate porosity measurement, the permeability of the FEM model that best matches the tank results corresponds to a grain size of 0.357mm, compared with the actual measurement of 0.2 mm for the ballotini in tank. If the true porosity is greater than the measured value (the value and error given in Emeana *et al.* 2016 is $n = 0.32 \pm 0.06$), the grain size equivalent of the permeability used in the model will be reduced. If the true porosity was a single standard error out (*i.e.* $n = 0.38$), the resulting grain size for the same permeability would be 0.251 mm according to the Kozeny-Carman equation.

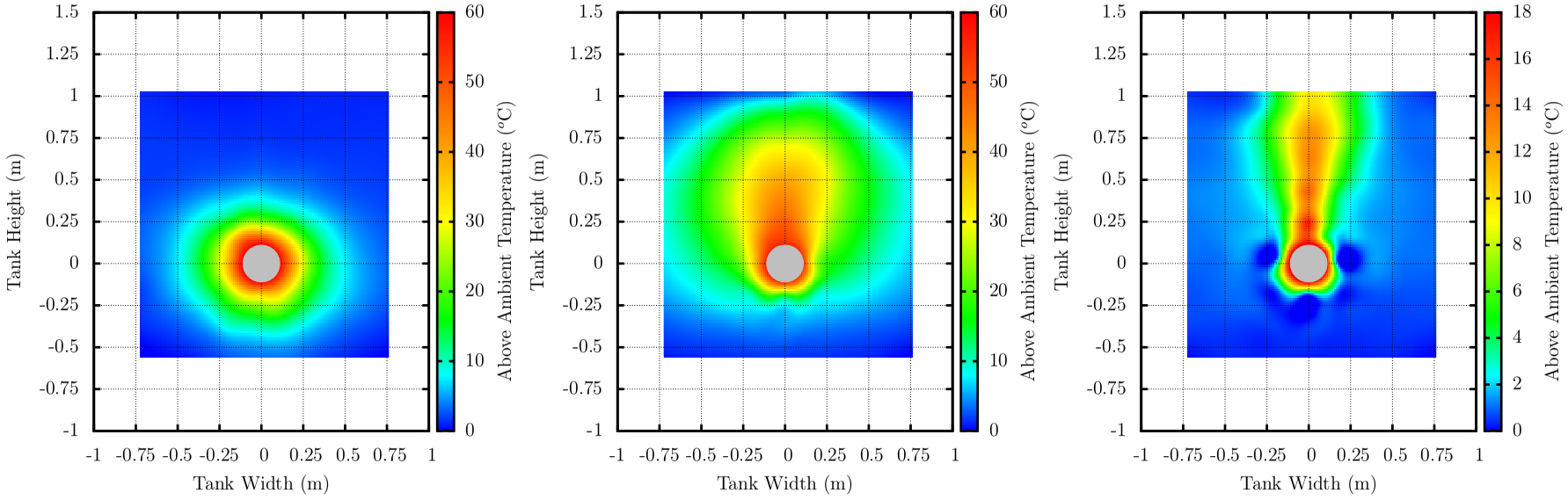

(a) Fine grained (impermeable) sediment (b) Medium grained (partially permeable) sediment (c) Coarse grained (permeable) sediment

Fig. B.3: Temperature plots (normalised by ambient temperature) of the experimental tank in a state of thermal equilibrium for the three different sediment types. The heat input from the central source is 50 W in each case.

- The use of the Kozeny-Carman equation to estimate the permeability from the measured grain size and porosity may not be perfectly reliable. Although it is stated in sections 3.5.1.3 and 3.5.1.4 that it provides a good estimate for the permeability based on the grain size and porosity of a sediment (and that the reliability increases for more uniform sediments), in order to be useful it has to be reliable for and applicable to a range of grain sizes and porosities representative of real natural sediments. This emphasis on reliability and breadth of application may marginally compromise the accuracy of the predictions based on this calculation.

- The FEM models constructed were 2D in nature. The tank experiment, however, was not a completely 2D system. Any characteristically 3D phenomena exhibited by the tank would lead to a difference between the tank results, and the FEM model predictions. It may be worth noting that the radius and axial length of the heat source were comparable (11 and 10 cm respectively, giving a ratio of the surface area of the curved face and the flat end faces of the heat source as: $2\pi rL/2 \cdot \pi r^2 = 0.1/0.11 = 10/11$). This would not be conducive to the accuracy of the approximation of the tank as a purely 2D system if there was a significant amount of heat dissipated through the front and rear tank faces that was not expected/accounted for. Although every attempt was made to mitigate the flow of heat parallel to the axis of the heat source (namely, by placing multiple layers of 10 cm thick insulating material on the outside of the tank during experimental runs), it was difficult to quantify how effective this was in reality.

  An approximation of how much heat might be lost through the front and rear faces of the tank can be obtained by making an order of magnitude calculation using equation (3.1), and estimating from Figure B.3(b) that there are roughly seven 0.25 m×0.25 m squares at ∼50 °C, and 19 at ∼ 25 °C above ambient (the thermal conductivity of the insulation material is 0.022 $\mathrm{Wm^{-1}K^{-1}}$[179]):

$$\begin{aligned}\iint_S q_z \cdot dxdy &\approx -\lambda \cdot \frac{\Delta T}{\Delta z} \cdot A \\ &= 0.022 \cdot \frac{50}{0.3} \cdot (0.25 \cdot 0.25) \cdot 7 \\ &+ 0.022 \cdot \frac{25}{0.3} \cdot (0.25 \cdot 0.25) \cdot 19 \\ &= 0.022 \cdot 0.0625 \cdot \left(\frac{50 \cdot 7 + 25 \cdot 19}{0.3}\right) \\ &\approx 4 \ \mathrm{Wm^{-1}K^{-1}} \text{ per face} \end{aligned} \tag{B.1}$$

Hence, the sum of the heat loss through the insulation for both the front and rear tank faces is roughly 8 $Wm^{-1}K^{-1}$ for an input heat of 50 W.

- Quantifying the amount of heat being dissipated through the experimental apparatus (as opposed to through the ballotini) is challenging. An indeterminate amount of energy will have been lost in the cable supplying electricity to the heat source. Some heat will also have been lost through the sides and base of the tank (although probably only a small amount due to their distance from the heat source). There was some evidence to suggest that heat was being lost through the front and rear faces of the tank, in spite of the many layers of insulation. A rise in temperature of ∼10 - 20 °C above ambient was recorded by a single thermocouple that was placed near the centre of the steel girder closest to the heat source (across the rear face of the tank). The steel girders on the rear face are in thermal contact with both the perspex wall of the tank (inside the insulation covering), and the steel frame. Heat will have been conducted along the girder in the centre of the tank (and possibly others) outwards and into the frame, to areas that were not covered by insulation (such as the legs at the base of the tank). Whether or not a significant amount of heat could have been dissipated in this manner is unknown; the instrumentation required to thoroughly investigate this hypothesis was not available concurrent to when the experiments were being conducted.

Despite the difficulties associated with drawing a direct quantitative comparison between the tank experiment and the model, it is still encouraging to note that the general trends in behaviour predicted by the model are mirrored in the experiment. For low permeabilities, conduction does seem to be the only mechanism through which heat from the source can be dissipated through the surrounding ballotini medium. As the permeability rises, the contribution to the dissipation of heat from convection become apparent. This change in the thermal behaviour is characterised by lower overall temperatures recorded by the thermocouples in the tank, and a reduction in the isotropy of the heat transfer as more heat is convected upwards. The observation of these phenomena is consistent between the tank experiment and the FEM models.

The reciprocation of significant convective dissipation in the tank experiments lends affirmation to the FEM model, and the predictions that it makes by demonstrating that convection can indeed occur in a physical system similar to the situation of a typical submarine HV cable.

APPENDIX C

List of Attended Conferences and Published Papers

C.1 Journal Papers

The following papers have been submitted to, and published in peer reviewed academic journals:

- Hughes, T.J., Henstock, T.J., Pilgrim, J.A., Dix, J.K., Gernon, T.M., Thompson, C.E.L., "Effect of Sediment Properties on the Thermal Performance of Submarine HV Cables", *IEEE Trans. Power Del.* **30**(6) p.2443-2450 (2015).

All material discussed therein is the work of Tim Hughes (supported by his supervisors, the other named authors), except the section entitled: Impact on Cable Design, which was co-written by James Pilgrim and Tim Hughes.

- Emeana, C.J., Hughes, T.J., Dix, J.K., Gernon, T.M., Henstock, T.J., Thompson, C.E.L., Pilgrim, J.A., "The Thermal Regime Around Buried Submarine High-voltage Cables", *Geophys. J. Int.* **206**(2) p.1051-1064 (2016).

The layout of the thermocouples in the tank was informed by preliminary FEM simulations conducted by Tim Hughes. He developed the FEM simulations depicted in Figures 4-6, wrote the computer programs used to analyse the raw data collected from the datalogger, and those used to produce: the temperature isotherm plots in Figures 3-7, the radial plots in Figures 8 -10, and the histograms in Figure 11.

C.2 Conferences

Talks have been presented on this work at the following conferences, listed in chronological order:

- Hughes, T.J., Henstock, T., Dix, J., Pilgrim, J., Gernon, T., "Heat Transfer in Cable Systems Under the Seafloor", *7th UHVNet Colloquium*, University of Surrey, Guildford, UK (15th-16th Jan 2014).
- Hughes, T.J., Henstock, T.J., Dix, J.K., Pilgrim J.A., Gernon, T.M., Thompson, C.E.L., "Environmental Controls on the Thermal Performance of HV Cables Under the Seafloor", *NSGG Postgraduate Symposium 2014*, BGS Keyworth, UK (13th May 2014) - **Awarded Best Paper**.
- Hughes, T.J., Henstock, T.J., Dix, J.K., Pilgrim, J.A., Gernon, T.M., Thompson, C.E.L., "Environmental Controls on the Thermal Performance of Submarine High Voltage Cables", *BGA Postgraduate Research in Progress Meeting 2014*, University of Liverpool, Liverpool, UK (4th-5th Sep 2014) - **Awarded Best Paper**.
- Hughes, T., Henstock, T., Pilgrim, J., Dix, J., Gernon, T., Thompson, C., "Thermal Ratings of Submarine HV Cables Informed by Environmental Considerations", *Jicable'15*, Palais de Congrès, Versailles, France (21st-25th Jun 2015).
- Hughes, T., Henstock, T., Pilgrim, J., Dix, J., Gernon, T., Thompson, C., "Understanding How Heat Generated in Submarine High Voltage Cables is Dissipated in the Surrounding Sediment", *Sea Lines of Communication 2015*, University of Southampton, Southampton, UK (17th Sep 2015).

References

[1] Brinser, H. N., "Submarine Power Cables", in *Oceans '76*, p.79–82, Washington DC, USA (13^{th} - 15^{st} Sep 1976).

[2] Eccles, M., Ferenez, J., & Burnett, D., "Submarine Power Cables", in *Submarine Cables: The Handbook of Law and Policy*, edited by Burnett, D. R., Beckman, R. C., & Davenport, T. M., Martinus Nijhoff, Leiden, Netherlands (2014).

[3] Howarth, B., Coates, M., & Renforth, L., "Fault Location Techniques for One of the World's Longest AC Interconnector Cables", in *8th IEE International Conference on AC and DC Power Transmission*, p.14–18, Savoy Place, London, UK (28^{th}-31^{st} Mar 2006).

[4] Worzyk, T., *Submarine Power Cables: Design, Installation, Repair, Environmental Aspects*, Springer-Verlag, Berlin, Germany (2009).

[5] Turvey, R., "Interconnector Economics", *Energy Policy* **34**(13), p.1457–1472 (2006).

[6] Department of Energy and Climate Change, "More Interconnection: Improving Energy Security and Lowering Bills", London, UK (2013).

[7] Weedy, B. M. & Shehata, S. A. M., "2GW Britain-France HVDC Link Transition Joint - Steady State Stresses", *IEEE Trans. Power Del.* **3**(4), p.1280–1288 (1986).

[8] Department for Business, Energy and Industrial Strategy, "Digest of United Kingdom Energy Statistics 2016", London, UK (2016).

[9] Department of Energy and Climate Change, "Digest of United Kingdom Energy Statistics 2015", London, UK (2015).

[10] HM Treasury, "National Infrastructure Plan 2014", London, UK (2014).

[11] 4C Offshore Interconnectors Database, "http://www.4coffshore.com/windfarms/interconnectors.aspx", accessed: 2015-10-15T19:00+01:00.

[12] 4C Offshore Global Offshore Wind Farms Database, "http://www.4coffshore.com/windfarms/", accessed 2015-10-15T19:00+01:00.

[13] de Decker, J. & Woyte, A., "Review of the Various Proposals for the European Offshore Grid", *Renewable Energy* **49**, p.58–62 (2013).

[14] Macilwain, C., "Energy: Supergrid", *Nature* **468**(7324), p.624–625 (2010).

[15] Edenhofer, O. *et al.*, editors, *Renewable Energy Sources and Climate Change Mitigation: Special Report of the Intergovernmental Panel on Climate Change*, Cambridge University Press, Cambridge, UK (2012).

[16] Carbon Trust, "Accelerating Marine Energy", London, UK (2011).

[17] House of Commons Energy and Climate Change Committee, "The Future of Marine Renewables in the UK", London, UK (2012).

[18] Philip, J. R. & de Vries, D. A., "Moisture Movement in Porous Materials under Temperature Gradients", *Trans. Am. Geophys. Union* **38**(2), p.222–232.

[19] Groeneveld, G. J., Snijders, A. L., Koopmans, G., & Vermeer, J., "Improved Method to Calculate the Critical Conditions for Drying Out Sandy Soils Around Power Cables", *IEE Proc.-C* **131**(2), p.42–53 (1984).

[20] Anders, G. J. & Radhakrishna, H. S., "Power Cable Thermal Analysis with Consideration of Heat and Moisture Transfer in the Soil", *IEEE Trans. Power Del.* **3**(4), p.1280–1288 (1988).

[21] Koopmans, G., van de Wiel, G. M. L. M., van Loon, L. J. M., & Palland, C. L., "Soil Physical Route Survey and Cable Thermal Design Proceedure", *IEE Proc.-C* **136**(6), p.341–346 (1989).

[22] Pilgrim, J. A., "Circuit Rating Methods for High Temperature Cables", PhD thesis, University of Southampton, UK (2011).

[23] Welty, J. R., Wicks, C. E., Wilson, R. E., & Rorrer, G. L., *Fundamentals of Momentum, Heat, and Mass Transfer*, John Wiley & Sons, Hoboken, NJ, USA, 5$^{\text{th}}$ Ed. (2008).

[24] Kaviany, M., *Principles of Heat Transfer in Porous Media*, Springer, New York, USA, 2$^{\text{nd}}$ Ed. (1995).

[25] Siegel, R. & Howell, J., *Thermal Radiation Heat Transfer*, Taylor & Francis, New York, USA, 4$^{\text{th}}$ Ed. (2002).

[26] Hanna, M. A., Chikhani, A. Y., & Salama, M. M. A., "Thermal Analysis of Power Cables in Multi-layered Soils Part 1: Theoretical Model", *IEEE Trans. Power Del.* **8**(3), p.761–771 (1993).

[27] IEC 60287-1:2006, *Electric Cables - Calculation of the Current Rating*, 2006.

[28] Purushothaman, S., de León, F., & Terracciano, M., "Calculation of Cable Thermal Rating Considering Non-isothermal Earth Surface", *IET Gener. Transm. Distrib.* **8**(7), p.1354–1361 (2014).

[29] Masson, D. G. *et al.*, "Seafloor Sediments and Sedimentary Processes on the Outer Continental Shelf, Continental Slope and Basin Floor", *DECC Strategic Environmental Assessments 4: Supporting Documents - Sediments*, London, UK (2003).

[30] Stephens, D. & Diesing, M., "Towards Quantitative Spatial Models of Seabed Sediment Composition", *PLoS One* **10**(11), p.1–23 (2015).

[31] van Landeghem, K. J. J. *et al.*, "Reversed Sediment Wave Migration in the Irish Sea, NW Europe: A Reappraisal of the Validity of Geometry-based Predictive Modelling and Assumptions", *Mar. Geol.* **295-298**, p.95–112 (2012).

[32] Weimers, L., "HVDC Light - A New Technology for a Better Environment", *IEEE Power Eng. Rev.* **18**(8), p.19–20 (1998).

[33] Simmons, M., "High Voltage Cables", in *High Voltage Engineering and Testing*, edited by Ryan, H. M., IET, London, UK, 2$^{\text{nd}}$ Ed. (2001).

[34] Dalal, S. B., Gorur, R. S., & Dyer, M. L., "Aging of Distribution Cables in Service and its Simulation in the Laboratory", *IEEE Trans. Dielectr. Electr. Insul.* **12**(1), p.139–146 (2005).

[35] Fink, L. H., "Control of the Thermal Environment of Buried Cable Systems", *Trans. AIEE (Power Apparatus and Systems)* **73**(1), p.406–412 (1954).

[36] Milne, A. G. & Mochlinski, K., "Characteristics of Soil Affecting Cable Ratings", *Proc. IEE* **111**(5), p.1017–1039 (1964).

[37] Mitchell, J. K. & Abdel-Hadi, O. N., "Temperature Distributions around Buried Cables", *IEEE Trans. Power App. Syst.* **98**(4), p.1158–1166 (1979).

[38] Freitas, D. S., Prata, A. T., & de Lima, A. J., "Thermal Performance of Underground Power Cables with Constant and Cyclic Currents in Presence of Moisture Migration in the Surrounding Soil", *IEEE Trans. Power Del.* **11**(3), p.1159–1170 (1996).

[39] de León, F. & Anders, G. J., "Effects of Backfilling on Cable Ampacity Analyzed With the Finite Element Method", *IEEE Trans. Power Del.* **23**(2), p.537–543 (2008).

[40] Swaffield, D. J., Lewin, P. L., & Sutton, S. J., "Methods for Rating Directly Buried High Voltage Cable Circuits", *IET Gener. Transm. Distrib.* **2**(3), p.393–401 (2008).

[41] Baazzim, M. S., Al-Saud, M. S., & El-Kady, M. A., "Comparison of Finite-Element and IEC Methods for Cable Thermal Analysis under Various Operating Environments", *Int. J. Electric. Comp. Electron. Comm. Eng.* **8**(3), p.470–475 (2014).

[42] Tayal, D. C., *Electricity and Magnetism*, Himalaya Publishing House, Mumbai, India (2009).

[43] Landau, L. D. & Liftshitz, E. M., *The Classical Theory of Fields*, Pergamon Press, Oxford, UK, 4th Ed. (1975).

[44] Griffiths, D. J., *Introduction to Electrodynamics*, Prentice Hall, Up Saddle River, NJ, USA, 3rd Ed. (1999).

[45] Purcell, E. M. & Morin, D. J., *Electricity and Magnetism*, Cambridge University Press, Cambridge, UK, 3rd Ed. (2013).

[46] Thue, W. A., editor, *Electrical Power Cable Engineering*, Marcel Dekker, New York, USA (1999).

[47] Parliamentary Office of Science and Technology, "UK Electricity Networks", *POST PN 163*, London, UK (2001).

[48] Worzyk, T., "Use of Aluminium Conductors in Submarine Power Cables", in *Jicable'15 B1.1*, p.1–6, Versailles, France (21st - 25th Jun 2015).

[49] Arkell, C. A., Hutson, R. B., & Nicholson, J. A., "Development of Internally Oil-cooled Cable Systems", *Proc. IEE* **124**(3), p.317–325 (1977).

[50] Bodega, R., van Rossum, J., & Geene, H., "Selecting the Optimized Conductor Design", in *Jicable'11 B10.1*, Versailles, France (19th - 23rd Jun 2011).

[51] Rizk, F. A. M. & Trinh, G. N., *High Voltage Engineering*, CRC Press, Boca Raton, FL, USA (2014).

[52] Milliken, H., "Electrical Cable", *US Patent 1,904,162* (1933).

[53] Bayliss, C. R. & Hardy, B. J., *Transmission and Distribution Electrical Engineering*, Elsevier, Oxford, UK, 4th Ed. (2012).

[54] Ciuprina, F., Teissèdre, G., & Filippini, J. C., "Polyethylene Crosslinking and Water Treeing", *Polymer* **42**(18), p.7841–7846 (2001).

[55] Attwood, J. R., "Cable Design for Subsea Power Links", *IEEE Pow. Eng. Rev.* **20**(9), p.13–14,21 (2000).

[56] International Cable Protection Committee, "Damage to Submarine Cables Caused by Anchors", *Loss Prevention Bulletin* (2009).

[57] Lennon, B., "Dielectric Relaxation Analysis to Assess the Integrity of High Voltage DC Cables of the Mass Impregnated Type", Master's thesis, Delft University of Technology, Netherlands, 2009.

[58] Yoon, H. & Na, W., "Safety Assessment of Submarine Power Cable Protectors by Anchor Dragging Field Tests", *Ocean Eng.* **65**, p.1–9 (2013).

[59] Boehme, T., "Subsea Power Connections that Work", in *European Wind Energy Association 2013 Annual Event*, p.1227–1231, Vienna, Austria (4th - 7th Feb 2013).

[60] Dix, J. K., *pers. comm.*, (2016).

[61] Hook, J. R. & Hall, H. E., *Solid State Physics*, John Wiley & Sons, Chichester, UK, 2nd Ed. (1991).

[62] Nauman, R. J., *Introduction to the Physics and Chemistry of Materials*, CRC Press, Boca Raton, FL, USA (2008).

[63] Sivanagaraju, S. & Satyanarayana, S., *Electrical Power Transmission and Distribution*, Dorling Kindersley, New Delhi, India (2009).

[64] Zangwill, A., *Modern Electrodynamics*, Cambridge University Press, Cambridge, UK (2013).

[65] Smythe, W. R., *Static and Dynamic Electricity*, McGraw Hill, New York, USA, 2nd Ed. (1950).

[66] Kaiser, K. L., *Electromagnetic Compatibility Handbook*, CRC Press, Boca Raton, FL, USA (2005).

[67] Anders, G. J., *Rating of Electric Power Cables: Ampacity Computations for Transmission, Distribution, and Industrial Applications*, McGraw Hill, New York, USA (1998).

[68] Smith, G. S., "Proximity Effect in Systems of Parallel Conductors", *J. Appl. Phys.* **43**(5), p.2196–2203 (1972).

[69] Kao, K. C., *Dielectric Phenomena in Solids*, Elsevier, San Diego, CA, USA (2004).

[70] Lewin, P. L., Theed, J. E., Davis, A. E., & Larsen, S. T., "Method for Rating Power Cables Buried in Surface Troughs", *IEE Proc.-C* **146**(4), p.360–364 (1999).

[71] Lewis, R. W., Nithiarasu, P., & Seetharamu, K. N., *Fundamentals of the Finite Element Method for Heat and Fluid Flow*, John Wiley & Sons, Chichester, UK (2004).

[72] Logan, D. L., *A First Course in the Finite Element Method*, Cengage Learning, Boston, MA, USA, 6th Ed. (2015).

[73] Clough, R. W., "The Finite Element Method in Plane Stress Analysis", in *Proceedings of the 2nd ASCE Conference on Electronic Computation*, p.345–378, Pittsburgh, PA, USA (8th - 9th Sep 1960).

[74] Huebner, K. H., Dewhirst, D. L., Smith, D. E., & Byrom, T. G., *The Finite Element Method for Engineers*, John Wiley & Sons, New York, USA, 4th Ed. (2001).

[75] Zienkiewicz, O. C., Taylor, R. L., & Zhu, J. Z., *The Finite Element Method: Its Basics and Fundamentals*, Elsevier Butterworth-Heinemann, Oxford, UK, 6th Ed. (2005).

[76] Desai, C. S. & Kundu, T., *Introductory Finite Element Method*, CRC Press, Boca Raton, FL, USA (2001).

[77] Howell, J. R., Menguc, M. P., & Siegel, R., *Thermal Radiation Heat Transfer*, CRC Press, Boca Raton, FL, USA, 6th Ed. (2015).

[78] Mardiana, R., "Parameters Affecting the Ampacity of HVDC Submarine Power Cables", in *2nd International Conference on Electrical Power and Energy Conversion Systems*, p.337–343, Sharjah, UAE (15th - 17th Nov 2011).

[79] Mills, A. F., *Heat Transfer*, Richard D. Irwin, Inc., New York, USA, 1st Ed. (1992).

[80] Riley, K. F., Hobson, M. P., & Bence, S. J., *Mathematical Methods for Physics and Engineering*, Cambridge University Press, Cambridge, UK, 3rd Ed. (2006).

[81] Lide, D. R., editor, *CRC Handbook of Chemistry and Physics*, CRC Press, Boca Raton, FL, USA, 84th Ed. (2003).

[82] Robertson, E. C., "Thermal Properties of Rocks", *US Geological Survey Open File Report 88-441*, Reston, VA, USA (1988).

[83] Dawson, M., "Silica Sand: Foundary Requirements and Classification", Cast Metal Services Pty. Ltd., Queensland, Australia (2004).

[84] Landau, L. D. & Liftshitz, E. M., *Fluid Mechanics*, Pergamon Press, Oxford, UK, 2nd Ed. (1987).

[85] Turcotte, D. L. & Schubert, G., *Geodynamics*, Cambridge University Press, Cambridge, UK, 2nd Ed. (2002).

[86] Bear, J., *Dynamics of Fluids in Porous Media*, American Elsevier, New York, USA (1972).

[87] Carson, J. K., Lovatt, S. J., Tanner, D. J., & Cleland, A. C., "Thermal Conductivity Bounds for Isotropic, Porous Materials", *Int. J. Heat Mass Tran.* **48**(11), p.2150–2158 (2005).

[88] Bart, G. C. J., "Thermal Conduction in Non Homogeneous and Phase Change Media", PhD thesis, Delft University of Technology, Netherlands (1994).

[89] Woodside, W. & Messmer, J. H., "Thermal Conductivity of Porous Media I: Unconsolidated Sands", *J. Appl. Phys.* **32**(9), p.1688–1699 (1961).

[90] Revil, A., "Thermal Conductivity of Unconsolidated Sediments with Geophysical Applications", *J. Geophys. Res.* **105**(B7), p.16749–16768 (2000).

[91] Lovell, M. A., "Thermal Conductivities of Marine Sediments", *Q. J. Eng. Quart. Geol.* **18**(4), p.437–441 (1985).

[92] Brigaud, F. & Vasseur, G., "Mineralogy, Porosity and Fluid Control on Thermal Conductivity of Sedimentary Rocks", *Geophys. J. Int.* **98**(3), p.525–542 (1989).

[93] Kasenow, M., *Applied Ground-water Hydrology and Well Hydraulics*, Water Resources Publications, Denver, CO, USA, 2nd Ed. (2001).

[94] Darcy, H. P. G., *Les Fontaines Publiques de la Ville de Dijon*, Dalmont, Paris, France (1856).

[95] Hamilton, E. L., "Compressional-Wave Attenuation in Marine Sediments", *Geophysics* **37**(4), p.620–646 (1972).

[96] Detmer, D. M., "Permeability, Porosity, and Grain-size Distribution of Selected Pliocene and Quaternary Sediments in the Albuquerque Basin", *New Mexico Geology* **17**(4), p.79–87 (1995).

[97] Carrier III, W. D., "Goodbye, Hazen; Hello, Kozeny-Carman", *J. Geotech. Geoenviron. Eng.* **129**(11), p.1054–1056 (2003).

[98] Drazin, P. & Riley, N., *London Mathematical Society Lecture Note Series 334: The Navier-Stokes Equations: A Classification of Flows and Exact Solutions*, Cambridge University Press, Cambridge, UK (2006).

[99] Johnson, R. W., editor, *The Handbook of Fluid Dynamics*, Springer-Verlag, Heidelberg, Germany (1998).

[100] Oertel, H., editor, *Prandtls Essentials of Fluid Mechanics*, Springer-Verlag, New York, USA, 2nd Ed. (2004).

[101] Nield, D. A. & Bejan, A., *Convection in Porous Media*, Springer, New York, USA, 4th Ed. (2013).

[102] Millero, F. J. & Poisson, A., "International One-atmosphere Equation of State of Seawater", *Deep Sea Res.* **28**(6), p.625–629 (1981).

[103] Sharqawy, M. H., Lienhard, J. H., & Zubair, S. M., "Thermophysical Properties of Seawater: A Review of Existing Correlations and Data", *Desalin. Water Treat.* **16**, p.354–380 (2010).

[104] Kell, G., "Density, Thermal Expansivity, and Compressibility of Liquid Water from 0^o to 150^oC: Correlations and Tables for Atmospheric Pressure and Saturation Reviewed and Expressed on 1968 Temperature Scale", *J. Chem. Eng. Data* **20**(1), p.97–105 (1975).

[105] Sclater, J. G., Corry, C. E., & Vacquier, V., "In Situ Measurements of the Thermal Conductivity of Ocean-floor Sediments,", *J. Geophys. Res.* **74**(4), p.10701081 (1969).

[106] Vugts, H. F. & Zimmerman, J. F. T., "The Heat Balance of a Tidal Flat Area", *Neth. J. Sea Res.* **19**(1), p.114 (1985).

[107] Bolton, A. J., Maltman, A. J., & Fisher, Q., "Anisotropic Permeability and Bimodal pore-size Distributions of Fine-grained Marine Sediments", *Mar. Petrol. Geol.* **17**(6), p.657–672 (2000).

[108] Bennett, R. H. *et al.*, "In Situ Porosity and Permeability of Selected Carbonate Sediment: Great Bahama Bank Part 1: Measurements", *Mar. Geotechnol.* **9**(1), p.1–28 (1990).

[109] Aleksandrov, A. A. & Trakhtengerts, M. S., "Viscosity of Water at Temperatures of -20^oC to 150^oC", *J. Eng. Phys. Thermophys.* **27**, p.1235–1239 (1974).

[110] Dullien, F. A. L., *Porous Media Fluid Transport and Pore Structure*, Academic Press, New York, USA (1979).

[111] Todd, D. K. & Mays, L. W., *Groundwater Hydrology*, John Wiley & Sons, Hoboken, NJ, USA, 3rd Ed. (2005).

[112] van Baars, S. & van der Graaf, H. C., "Determination of Organic Soil Permeability Using the Piezocone Dissipation Test", *Environ. Eng. Geosci.* **13**(3), p.197–203 (2007).

[113] Lovell, M. A., "Thermal Conductivity and Permeability Assessment by Electrical Resistivity Measurements in Marine Sediments", *Mar. Geotechnol.* **6**(2), p.205–240 (1985).

[114] Jackson, D. R. & Richardson, M. D., *High-frequency Seafloor Acoustics*, Springer, New York, USA (2007).

[115] Santos, I. R., Eyre, B. D., & Huettel, M., "The Driving Forces of Porewater and Groundwater Flow in Permeable Coastal Sediments: A Review", *Estuar. Coast. Shelf S.* **98**, p.1–15 (2012).

[116] Dias, R., M.Mota, Teixeira, J. A., & Yelshin, A., "Study of Ternary Glass Spherical Particle Beds: Porosity, Tortuosity and Permeability", *Filtration* **5**(1), p.68–75 (2005).

[117] Shepherd, R. G., "Correlations of Permeability and Grain Size", *Ground Water* **27**(5), p.633638 (1989).

[118] Carman, P. C., "Fluid Flow Through Granular Beds", *Trans. Instn. Chem. Eng.* **15**, p.150–166 (1937).

[119] Moon, P. & Spencer, D. E., "The Meaning of the Vector Laplacian", *J. Frankl. Inst.* **256**(6), p.551–558 (1953).

[120] Vukovic, M. & Soro, A., *Determination of Hydraulic Conductivity of Porous Media from Grain-Size Composition*, Water Resources Publications, Denver, CO, USA (1992).

[121] Terzaghi, K., Peck, R. B., & Mesri, G., *Soil Mechanics in Engineering Practise*, John Wiley & Sons, New York, USA, 3rd Ed. (1996).

[122] Kasenow, M., *Determination of Hydraulic Conductivity from Grain Size Analysis*, Water Resources Publications, Denver, CO, USA (2002).

[123] Hazen, A., "Some Physical Properties of Sands and Gravels, with Special Reference to their Use in Filtration", *Mass. State Board of Health Ann. Rep.* **24**(34), p.539556 (1892).

[124] Odong, J., "Evaluation of Empirical Formulae for Determination of Hydraulic Conductivity based on Grain-Size Analysis", *J. Amer. Sci.* **3**(3), p.54–60 (2007).

[125] Loudon, A. G., "The Computation of Permeability from Simple Soil Tests", *Geotechnique* **3**(4), p.165–183 (1952).

[126] Masch, F. D. & Denny, K. J., "Grain Size Distribution and its Effect on The Permeability of Unconsolidated Sands", *Water Resour. Res.* **2**(4), p.665–677 (1966).

[127] Boadu, F. K., "Hydraulic Conductivity of Soils from Grain-Size Distributions: New Models", *J. Geotech. Geoenviron. Eng.* **180**(August), p.739–746 (2000).

[128] Mavko, G. & Nur, A., "The Effect of a Percolation Threshold in the Kozeny-Carman Relation", *Geophysics* **62**(5), p.1480–1482 (1997).

[129] Pan, C., Hilpert, M., & Miller, C., "Pore-scale Modeling of Saturated Permeabilities in Random Sphere Packings", *Phys. Rev. E* **64**(6), p.1–9 (2001).

[130] Forster, S., Bobertz, B., & Bohling, B., "Permeability of Sands in the Coastal Areas of the Southern Baltic Sea : Mapping a Grain-size Related Sediment Property", *Aquat. Geochem.* **9**, p.171–190 (2003).

[131] Zaman, E. & Jalali, P., "On Hydraulic Permeability of Random Packs of Monodisperse Spheres: Direct Flow Simulations Versus Correlations", *Physica A* **389**(2), p.205–214 (2010).

[132] Kozeny, J., "Ueber Kapillare Leitung des Wassers im Boden", *Akad. Wiss. Wien* **136**, p.271–306 (1927).

[133] Chapuis, R. P. & Aubertin, M., "On the Use of the Kozeny-Carman Equation to Predict the Hydraulic Conductivity of Soils", *Can. Geotech. J.* **40**(3), p.616–628 (2003).

[134] Carman, P. C., "Permeability of Saturated Sands, Soils and Clays", *J. Agric. Sci.* **29**(2), p.262–273 (1939).

[135] Mbonimpa, M., Aubertin, M., Chapuis, R. P., & Bussie, B., "Practical Pedotransfer Functions for Estimating the Saturated Hydraulic Conductivity", *Geotech. Geol. Eng.* **20**, p.235–259 (2002).

[136] Soulsby, R. L., *Dynamics of Marine Sands*, Thomas Telford Publications, London, UK (1997).

[137] Slichter, C. S., "Theoretical Investigation of the Motion of Ground Waters", *19th Ann. Rep. US Geological Survey Part 2* (1899).

[138] Cheng, C. & Chen, X., "Evaluation of Methods for Determination of Hydraulic Properties in an Aquifer-aquitard System Hydrologically Connected to a River", *Hydrogeol. J.* **15**(4), p.669–678 (2007).

[139] Chapuis, R. P., "Predicting the Saturated Hydraulic Conductivity of Sand and Gravel Using Effective Diameter and Void Ratio", *Can. Geotech. J.* **41**(5), p.787–795 (2004).

[140] Song, C., Wang, P., & Makse, H. A., "A Phase Diagram for Jammed Matter", *Nature* **453**(7195), p.629–632 (2008).

[141] Wentworth, C. K., "A Scale of Grade and Class Terms for Clastic Sediments", *J. Geol.* **30**(5), p.377392 (1922).

[142] Boggs Jr., S., *Petrology of Sedimentary Rocks*, Cambridge University Press, Cambridge, U.K., 2nd Ed. (2009).

[143] Huettel, M., Ziebis, W., & Forster, S., "Flow-induced Uptake of Particulate Matter in Permeable Sediments", *Limnol. Oceanogr.* **41**(2), p.309–322 (1996).

[144] Jansen, F., Huettel, M., & Witte, U., "Pore-water Advection and Solute Fluxes in Permeable Marine Sediments (II): Benthic Respiration at Three Sandy Sites with Different Permeabilities (German Bight, North Sea)", *Limnol. Oceanogr.* **50**(3), p.779–792 (2005).

[145] Lowe, D. R., "Water Escape Structures in Coarse-grained Sediments", *Sedimentology* **22**(2), p.157–204 (1975).

[146] Wilson, A. M., Huettel, M., & Klein, S., "Grain Size and Depositional Environment as Predictors of Permeability in Coastal Marine Sands", *Estuar. Coast. Shelf* **80**, p.193–199 (2008).

[147] Chu, J., Bo, M. W., Chang, M. F., & Choa, V., "Consolidation and Permeability Properties of Singapore Marinem Clay", *J. Geotech. Geoenviron. Eng.* **128**(9), p.724–732 (2002).

[148] Bennett, R. H. *et al.*, "In situ Permeabilities of Selected Coastal Marine Sediments", *IEEE. J. Oceanic Eng.* **27**(3), p.571–580 (2002).

[149] Billerbeck, M. *et al.*, "Nutrient Release from an Exposed Intertidal Sand Flat", *Mar. Ecol. Prog. Ser.* **316**, p.35–51 (2006).

[150] Ehrenberg, S. N., Eberli, G. P., & Baechle, G., "Porosity-permeability Relationships in Miocene Carbonate Platforms and Slopes Seaward of the Great Barrier Reef, Australia (ODP Leg 194, Marion Plateau)", *Sedimentology* **53**(6), p.1289–1318 (2006).

[151] Franke, U., Polerecky, L., Precht, E., & Huettel, M., "Wave Tank Study of Particulate Matter Degradation in Permeable Sediments", *Limnol. Oceanogr.* **51**(2), p.1084–1096 (2006).

[152] Hamdi, F. & Taylor Smith, D., "The Influence of Permeability on Compressional Wave Velocity in Marine Sediments", *Geophys. Prospect.* **30**, p.622–640 (1982).

[153] Huettel, M. & Gust, G., "Solute Release Mechanisms from Confined Sediment Cores in Stirred Benthic Chamber Flume Flows", *Mar. Ecol. Prog. Ser.* **82**, p.187–197 (1992).

[154] Huettel, M., Ziebis, W., Forster, S., & Luther, G. W., "Advective Transport Affecting Metal and Nutrient Distributions and Interfacial Fluxes in Permeable Sediments", *Geochim. Cosmochim. Ac.* **62**(4), p.613–631 (1998).

[155] Huettel, M. & Rusch, A., "Transport and Degradation of Phytoplankton in Permeable Sediment", *Limnol. Oceanogr.* **45**(3), p.534–549 (2000).

[156] Huettel, M. *et al.*, "Transport and Degradation of a Dinoflagellate Bloom in Permeable Sublittoral Sediment", *Mar. Ecol. Prog. Ser.* **340**, p.139–153 (2007).

[157] Hunter, E. M., Mills, H. J., & Kostka, J. E., "Microbial Community Diversity Associated with Carbon and Nitrogen Cycling in Permeable Shelf Sediments", *Appl. Environ. Microbiol.* **72**(9), p.5689–5701 (2006).

[158] Jahnke, R. *et al.*, "Organic Matter Remineralization and Porewater Exchange Rates in Permeable South Atlantic Bight Continental Shelf Sediments", *Cont. Shelf Res.* **25**, p.1433–1452 (2005).

[159] Precht, E. & Huettel, M., "Rapid Wave-driven Advective Pore Water Exchange in a Permeable Coastal Sediment", *J. Sea Res.* **51**, p.93–107 (2004).

[160] Rasheed, M., Badran, M. I., & Huettel, M., "Particulate Matter Filtration and Seasonal Nutrient Dynamics in Permeable Carbonate and Silicate Sands of the Gulf of Aqaba, Red Sea", *Coral Reefs* **22**, p.167–177 (2003).

[161] Rasheed, M., Wild, C., Franke, U., & Huettel, M., "Benthic Photosynthesis and Oxygen Consumption in Permeable Carbonate Sediments at Heron Island, Great Barrier Reef, Australia", *Estuar. Coast. Shelf S.* **59**, p.139–150 (2004).

[162] Reimers, C. E. *et al.*, "In situ Measurements of Advective Solute Transport in Permeable Shelf Sands", *Cont. Shelf Res.* **24**, p.183–201 (2004).

[163] Rusch, A., Huettel, M., & Forster, S., "Particulate Organic Matter in Permeable Marine Sands - Dynamics in Time and Depth", *Estuar. Coast. Shelf S.* **51**, p.399–414 (2000).

[164] Wild, C., Tollrian, R., & Huettel, M., "Rapin Recycling of Coral Mass-spaawning Products in Permeable Reef Sediments", *Mar. Ecol. Prog. Ser.* **271**, p.159–166 (2004).

[165] Wild, C. *et al.*, "Benthic Metabolism and Degradationof Natural Particulate Organic Matter in Carbonate and Silicate Sand Reefs of the Nothern Red Sea", *Mar. Ecol. Prog. Ser.* **298**, p.69–78 (2005).

[166] Wild, C., Laforsch, C., & Huettel, M., "Detection and Enumeration of Microbial Cells within Highly Porous Calcareous Reef Sands", *Mar. Freshwater Res.* **57**, p.415–420 (2006).

[167] Høyer-Hansen, M. & Lervik, J. K., "Evaluation of Cross-talk in Power Cables by Use of 3D Finite Element Computations", in *Jicable'15 E4.3*, Versailles, France (21st - 25th Jun 2015).

[168] Lide, D. R., editor, *CRC Handbook of Chemistry and Physics*, CRC Press, Boca Raton, FL, USA, 85th Ed. (2004).

[169] Martienssen, W. & Warlimont, H., editors, *Springer Handbook of Condensed Matter and Materials Data*, Springer, Berlin, Germany (2005).

[170] Cverna, F., editor, *Thermal Properties of Metals*, ASM International, Materials Park, OH, USA (2002).

[171] Goto, S. & Matsubayashi, O., "Relations Bewteen the Thermal Properties and Porosity of Sediments in the Eastern Flank of the Juan de Fuca Ridge", *Earth Planets Space* **61**(7), p.863–870 (2009).

[172] IEEE Std 442-1981, *IEEE Guide for Soil Thermal Resistivity Measurements*, 1981.

[173] Dennis, J. E. & Mei, H. H. W., "Two New Unconstrained Optimization Algorithms which use Function and Gradient Values", *J. Optimiz. Theory App.* **28**(4), p.453–482 (1979).

[174] Versteeg, H. K. & W. Malalasekera, *An Introduction to Computational Fluid Dynamics*, John Wiley & Sons, New York, USA (1995).

[175] Bejan, A. & Kraus, A. D., *Heat Transfer Handbook*, John Wiley & Sons, Hoboken, NJ, USA (2003).

[176] Csanady, G. S., "Mean Circulation in Shallow Seas", *J. Geoophys. Res.* **81**(30), p.5389–5399 (1976).

[177] Emeana, C. J. *et al.*, "Sediment Thermal Properties and Heat Flow Implication on the Performance of Sub-seabed HV Cables", in *British Geophysics Association Postgraduate Research in Progress Meeting 2014*, Liverpool, UK (4th - 5th Sep 2014).

[178] Hughes, T. J. *et al.*, "Effect of Sediment Properties on the Thermal Performance of Submarine HV Cables", *IEEE Trans. Power Del.* **30**(6), p.2443–2450 (2015).

[179] Emeana, C. J. *et al.*, "The Thermal Regime Around Buried Submarine High-voltage Cables", *Geophys. J. Int.* **206**(2), p.1051–1064 (2016).

[180] Wæraas de Saint Martin, G., Charvet, J., & Veal, C., "Development of a Three-terminal Ready HVDC Interconnector between France and Great Britain via Alderney", in *Jicable'15 B4.4*, p.1–6, Versailles, France (21st - 25th Jun 2015).

[181] Whitehouse, R. J. S., Harris, J. M., Sutherland, J., & Rees, J., "The Nature of Scour Development and Scour Protection at Offshore Windfarm Foundations", *Mar. Pollut. Bull.* **62**(1), p.73–88 (2011).

[182] Dix, J. K., *pers. comm.*, Presentation to Industry Representatives, (7th Dec 2015).

[183] BERR, "Review of Cabling Techniques and Environmental Effects Applicable to the Offshore Wind Farm Industry", London, UK (2008).

[184] Forewind Ltd., "Dogger Bank Creyke Beck Environmental Statement - Chapter 5", *F-OFC-CH-005 Issue 4*, Reading, UK (5th Aug 2013).

[185] Hughes, T. J. *et al.*, "Thermal Ratings of Submarine HV Cables Informed by Environmental Considerations", in *Jicable'15 D9.6*, p.1–6, Versailles, France (21st - 25th Jun 2015).

[186] Nichols, G., *Sedimentology and Stratigraphy*, Wiley-Blackwell, Chichester, UK, 2nd Ed. (1999).

[187] Wheatcroft, R. A., "*In Situ* Measurements of Near-surface Porosity in Shallow-water Marine Sands", *IEEE J. Oceanic Eng.* **27**(3), p.561–570 (2002).

[188] Anders, G. J. & El-Kady, M. A., "Transient Ratings of Buried Power Cables Part 1: Historical Perspective and Mathematical Model", *IEEE Trans. Power Del.* **7**, p.1724–1734 (1992).

[189] Carvill, J., *Mechanical Engineer's Data Handbook*, Butterworth-Heinemann, Oxford, UK, 1st Ed. (1993).

[190] Pilgrim, J. *et al.*, "Offshore Wind Farm Export Cable Current Rating Optimisation", in *European Wind Energy Association Offshore 2013*, p.1–10, Frankfurt, Germany (19^{th}-21^{st} Nov 2013).

[191] Chippendale, R., Cangy, P., & Pilgrim, J., "Thermal Ratings of J-tubes using Finite Element Analysis Techniques", in *Jicable'15 B5.4*, p.1–6, Versailles, France (21^{st} - 25^{th} Jun 2015).

[192] London Metal Exchange, "Copper Price Per Tonne Sterling Equivalent", http://www.lme.com/en-gb/metals/non-ferrous/copper/ accessed: 2016-07-23T18:00+01:00.

[193] Vardy, M. E., "Deriving Shallow-water Sediment Properties using Post-stack Acoustic Impedance Inversion", *Near Surf. Geophys.* **13**(2), p.143–154 (2015).

[194] Ashby, N., "Relaxation of Charge Imbalances in Conductors", *Am. J. Phys.* **43**(6), p.553–555 (1975).

[195] Popović, Z. & Popović, B. D., *Introductory Electromagnetics*, Prentice Hall, Upper Saddle River, NJ, USA (2000).

[196] Folk, R. L. & Ward, W. C., "Brazos River Bar: A Study in the Significance of Grain Size Parameters", *J. Sediment. Petrol.* **27**(1), p.3–26 (1957).

[197] Amyx, J. W., Bass, D. M., & Whiting, R. L., *Petroleum Reservoir Engineering: Physical Properties*, McGraw Hill, New York, USA (1960).

[198] Potters-Ballotini Co., Ltd., "http://www.pqj.co.jp/en/product/01.html", accessed: 2016-05-15T22:02+01:00.